Pathogen detection with the Nanofiber- Light Addressable Potentiometric Sensor (NF-LAPS)
by

Parmiss Mojir Shaibani

A thesis submitted in partial fulfillment of the requirements for the degree of

Doctor of Philosophy
in
Materials Engineering

Chemical and Materials Engineering
University of Alberta

Abstract

The basic human right to have safe and clean drinking water cannot be neglected with the ever-rising worldwide need for drinking water that meets global standards. Local monitoring of water sources is even more vital in areas where access to pure drinking water is limited and its processing facilities are out of reach. The lack of sophisticated medical services in remote areas also makes providing clean drinking water crucial due to the danger of infectious outbreaks. These outbreaks, or even isolated cases of infections may seem easily treatable in more urbanized areas, but basic treatment may not be sufficient in more rural sites.

One of the most widely occurring pathogens in water is *Escherichia coli* (*E. coli*). The presence of *E. coli* although infectious on its own, can also often be an indicator for the existence of other harmful coliforms in water. Therefore *E. coli* is an important target for detection in water. To provide more economic means of *E. coli* detection that can be used on-site, there is a need to develop a portable sensor system that will not require highly qualified personnel training and can be used for rapid on/off based detection. For this reason, a simple, rapid and cost effective detection technique for *E. coli* using a Light Addressable Potentiometric Sensor integrated with electrospun polyvinyl alcohol/poly acrylic acid (PVA/PAA) hydrogel nanofibers as the sensing layer (NF-LAPS) is reported. Changes in pH of the media are detected as *E. coli* cells ferment glucose molecules and increase acidity of the surrounding. A super-Nernstian response of a 74 mV/pH change in the NF-LAPS provides high sensitivity towards *E. coli* with a theoretical limit of detection (LOD) of 20 CFU/ml. The measured limit of detection in this work is 100 CFU/ml. The high sensitivity is associated with the pH sensitive behavior of the NFs on the surface. Detection of acidic species released in cellular metabolism of pathogens in the presence of carbon source renders the sensing mechanism cheaper, less time consuming and more practical

than the antibody-antigen interaction based approach. Selectivity towards *E. coli* for applications in drinking water detection is ensured by the incorporation of d-mannose for specific binding. Selectivity is examined against *Pseudomonas fluorescens* (*P. fluorescens*).

To examine the possible application of the biosensor for other beverages with complex media (with more compounds compared to water), the detection of *E. coli* in orange juice with a portable NF-LAPS prototype device was investigated. The measured limit of detection in this work is 100 CFU/ml. The selectivity of the biosensor towards *E. coli* is confirmed by examining the response of the NF-LAPS against *Salmonella typhimurium* (*S. typhi*), also commonly found in orange juice. *S. typhi* is also a sugar fermenting genus of bacteria. The entire NF-LAPS system is packaged into a portable device with the readout displayed on a generic tablet. The Device is also capable of wirelessly transmitting data into the analysis software. Real water samples are tested with the working prototype of the portable NF-LAPS.

In addition, to demonstrate the versatility of the NF-LAPS, the system was used to investigate the metabolic activity of breast cancer cells in the presence of sugar. Over the testing period of 2 h, cancer cells (MDA MB231) showed a response of approximately 0.4 change in pH compared to a virtually no change for normal cells (MCF10A). The role of metabolic inhibitors is also examined by monitoring cellular metabolism. The conclusion is that the use of inhibitors suppresses the acidification process in cancer cells. This study based on the extracellular acidification of cancer cells enhances our understanding of cancer cell metabolic activity and their response to antibiotics, which in turn will help in the development of better treatments, drugs and drug dosages.

Preface

The electrospinning referred to in chapters 3, 4 and 5 was designed by myself and Mr. Amirreza Sohrabi, with the assistance of Professor T. Thundat. The data analysis in chapters 3,4,5 and concluding analyses are my original work, as well as the literature review in chapters 1 and 2.

Chapter 3 of this thesis has been published as P.M. Shaibani, K. Jiang, G. Haghighat, M. Hassanpourfard, H. Etayash, S. Naicker, T. Thundat, The detection of Escherichia coli (E. coli) with the pH sensitive hydrogel nanofiber-light addressable potentiometric sensor (NF-LAPS), Sensors Actuators, B Chem. 226 (2016) 176–183. doi:10.1016/j.snb.2015.11.135. I was responsible for the data collection and analysis as well as the manuscript composition. G. Haghighat assisted with literature review and nanofiber fabrication. K. Jiang, M. Hassanpourfard and H. Etayash assisted with the data collection and contributed to manuscript edits. T. Thundat was the supervisory author and S. Naicker and T. Thundat were involved with concept formation and manuscript composition.

Some of the research conducted for this thesis forms part of a research collaboration, led by Professor T. Thundat at the University of Alberta, with Professor K. Kaur being the lead collaborator at the University of Alberta as well as Chapman University. I was responsible for providing the sensor and data analysis. Parts of chapter 5 has been published as P.M. Shaibani, H. Etayash, S. Naicker, T. Thundat, "Metabolic study of cancer cells using a pH Sensitive hydrogel Nanofiber Light Addressable Potentiometric Sensor (NF-LAPS)", ACS Sensors, DOI: 10.1021/acssensors.6b00632 (2017). The manuscript was written mainly by me and H. Etayash. S. Naicker and T. Thundat helped with data analysis and manuscript composition.

Dedication

I dedicate this work to my wonderful, supportive husband Amirreza Sohrabi and my family who have supported me my entire life. I would also like to dedicate it to all the girls who want to make a difference in the world.

Acknowledgements

This work is supported by the India-Canada Centre for Innovative Multidisciplinary Partnerships to Accelerate Community Transformation and Sustainability (IC-IMPACTS) program and the Canada Excellence Research Chairs (CERC) program. I would like to offer my deepest gratitude towards the Nano Fabrication Lab, Oil Sands and Coal Interfacial Engineering Facility (OSCIEF) and Alberta Centre for Surface Engineering & Sciences (ACSES) for characterization equipment and analysis.

I would especially like to thank Prof. Thomas Thundat for his insight and leadership throughout this work and his excellent supervision. This research would not have been possible without his advice and his will for me to excel at every stage. His vision to help translate laboratory tools to real life applications drove this work.

Dr. Slevaraj Naicker has also been of immense help through the experimental planning, giving direction and analysis of acquired data. He has been a wonderful source of inspiration and assistance. His support is greatly appreciated.

I would also like to thank the members of my supervisory committee, Dr. Hyun-Joong Chung and Dr. Zubin Jacob whose guidance is highly valued.

My deepest gratitude goes to my husband Amirreza Sohrabi for his unconditional support and help in every step. He has contributed to this research scientifically and personally.

I would like to thank the co-authors of our publications and prepared manuscripts, Keren Jiang, Ghazaleh Haghighat, Mahtab Hassanpourfard, Hashem Etayash and Dr. Kamaljit Kaur for all their contribution.

In addition, I would like to thank Mehrnaz Rahimi, Dr. Charles Van Neste, Richard Hull, John E. Hawk and Arindam Phani for helpful discussions and on going support. I extend my gratitude all the members of the group for their help.

Finally, I would like to acknowledge our summer students Neethu Xavier and Shilpa Anthony for their assistance and their determination to learn.

Table of Contents

List of Tables

List of Figures

List of Abbreviations

CFU	Colony forming unit
E. coli	*Escherichia coli*
ELISA	Enzyme-Linked Immunosorbent Assay
PCR	Polymerase chain reaction
QCM	Quartz Crystal Microbalance
SPR	Surface plasmon resonance
Taq	*Thermus Aquaticus*
UN	United Nations
BW	Bulk wave
TSM	Thickness shear mode
SAW	surface acoustic wave
SRB	sulphate-reducing bacteria
MEMS	Micro-elecrtromechanical Systems
DMD	digital micromirror devices
SEM	scanning electron microscope
LOD	Limit of detection
FET	Field effect transistors
LAPS	light addressable potentiometric sensor
WE	Working electrode
DLP	Digital light processor
CHEMFET	chemical field effect transistors
PVA	polyvinyl alcohol
PAA	poly acrylic acid
NF	Nanofiber
RWS	Real water samples
PBS	Phosphate buffer saline
PS	Polystyrene
PSMA	poly(styrene-alt-maleic anhydride
MMP-9	Matrix metalloproteinases-9
SAF	Self-assembled nanofiberous gels
TRIS	Tri(hydroxymethyl)aminomethane
RE	Reference electrode
CE	Counter electrode
NF-LAPS	Nanofiber-Light addressable potentiometric sensor
FT-IR	Fourier transform infrared spectroscopy
EVM	Evaluation module
DC	Direct current
LB	Luria–Bertani
PI	Propidium iodide
P. fluorescens	*Pseudomonas fluorescens*

NJ	New jersey
GFP	green fluorescent protein
MQ	MilliQ
3D	3-dimentional
LED	Light emitting diode
SNR	Signal to noise ratio
FDA	Food and drug administration
S. Typhi	*Salmonella typhimurium*
ATCC	American type culture collection
VA	Virginia
DMEM	Dulbecco's modified eagle medium
FBS	fetal bovine serum
LSV	Linear sweep voltammetry
2-DG	2-deoxyglucose
SD	Standard deviation

Chapter 1: Introduction

Planet earth holds approximately 1.4 billion km^3 of water from which only 2.5% is classified as fresh water. Realistically, only about 200,000 km^3 of fresh water rounding up to less than 1% of all bodies of water, can be used as supply for people and the earth's ecosystems [1]. With the ever-growing population of the world, it is becoming increasingly difficult to provide sufficient amounts of water for human use compliable with global standards. The United Nations (UN) has addressed the need for safe global drinking water in its mandate to, "by 2030, achieve universal and equitable access to safe and affordable drinking water for all" [2].

Production, distribution and monitoring of water that is safe to drink have particularly become the focus of global discussions as water directly affects the quality of life. In the case of drinking water, guidelines are presented in terms of the maximum amount of various substances permitted in water. Substances are considered by their effect on the appearance of water, effect on the health of the consumer as well as interference with processes or technologies used for water treatment or water infrastructure, e.g. corrosion [3]. Maintaining the specified guideline standards becomes more difficult in rural or remote areas where access to state of the art facilities is rare and local water sources are utilized for public use; monitoring the quality of water is especially challenging in these locations due to lengthy analysis procedures and far distances from equipped labs. For this reason, the need arises for local analysis techniques and devices that can be employed on site to examine the water sources for harmful entities such as pathogens.

Incidents of bacteria breakout in drinking water have often been reported in developed countries as well as developing countries. Reports of these outbreaks will be highlighted in the coming

sections. All the different reports and infection statistics indicate the vital need for the development of tools and techniques that can be used to monitor water sources for the early detection of hazardous pathogens to prevent future outbreaks or even unlikely disastrous events related to public outbreaks.

1.1. World waters and contaminants

In this section, the global distribution of water and the categories of contaminants that threaten the safety of world waters for drinking purposes are reviewed.

1.1.1. World water distribution

The world's total renewable water resource per capita per year as reported by UN in 2015 is illustrated in figure 1.1 [4]. As the figure suggests, the renewable water resources around the world are not evenly distributed. Scarcity of water resources that can be used for human consumption is becoming increasingly alarming with the population of the world increasing. Moreover, climate change is affecting the availability of water, worldwide [5]. Therefore, it is of utmost importance to take measures that make good use of the water that is available and ensure its safety for drinking.

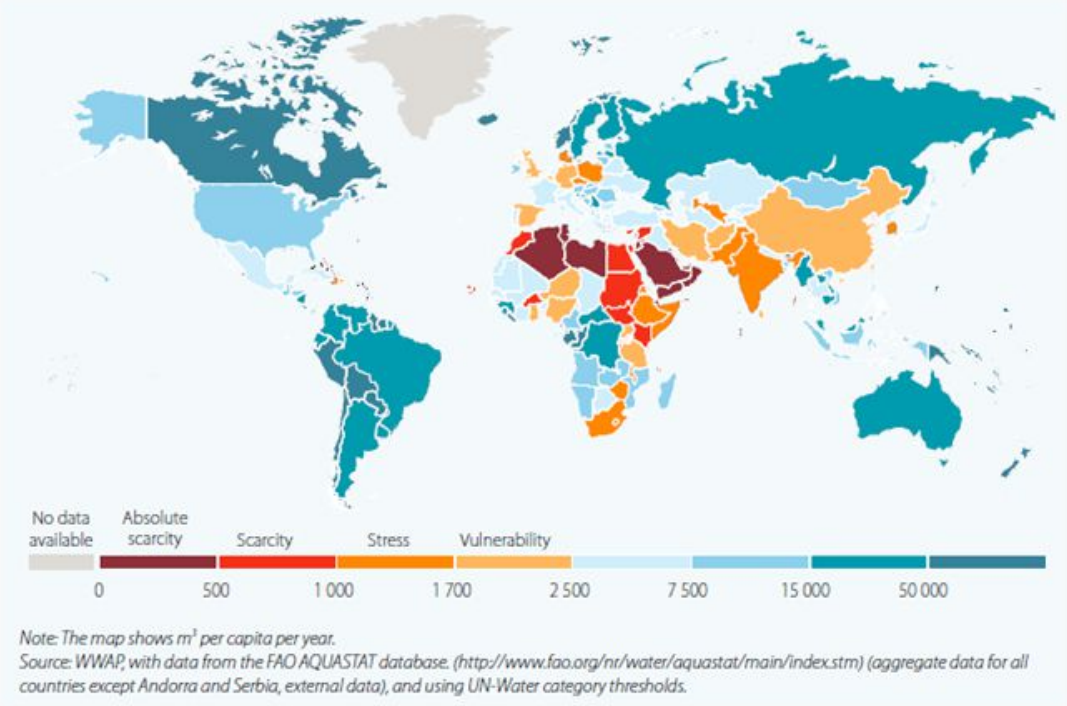

Figure 1.1. The total renewable water resources distribution in the world per capita as reported by the UN [4]. Water resources are not evenly distributed and renewable water resources are highly scarce in parts of the world.

1.1.2. Contaminants in water

There are a variety of substances and microorganisms that threaten the safety of water for drinking. In general, contaminants in water can be categorized as follows [3,6]:

- Physical contaminants
- Chemical contaminants
- Microbial contaminants
- Radiological contaminants

Physical contamination in water pertains to any changes in the appearance of water or any physical changes in it as a result of events such as mineral sedimentation or suspended substances in water.

The category of chemical contamination in water covers a broad range of chemical elements or compounds that can occur from natural sources or of be of man-made origin. These chemicals include agricultural pesticides, metals, pharmaceutical compounds, etc. [6]. Pharmaceutical compounds are regarded as emerging contaminants that have raised additional concern in the water community [7].

Bacteria, viruses and protozoa (parasites) are considered examples of microbial contaminants, also known as biological contaminants. Human or animal feces are the most common sources of microbial contaminants in water. Examples of the different microbial contaminant groups include *Escherichia coli* (*E. coli*), poliovirus and cryptosporidium, respectively.

Radiological contaminants arise from elements with an unbalanced number of protons and neutrons in the nucleus that cause instability in the chemical and consequent radiation. Plutonium for instance is a radioactive element.

Here the focus is on microbial microorganisms that can contaminate water, in particular *E. coli*. *E. coli* is a gram-negative rod-shaped bacterium with mostly harmless strains; however, some serotypes of *E .coli* can cause a variety of problems if ingested. Food poisoning with *E. coli* may lead to diarrhea, bloody diarrhea, hemorrhagic colitis, and a type of kidney failure called hemolytic uremic syndrome [8,9]. The *E. coli* 0157:H7 strain produces Shiga toxin that leads to different symptoms in humans [10]. Moreover, the presence of *E. coli* can often be an indicator organism for the existence of other microbial contaminants in water [11].

Incidents of bacteria breakout in drinking water have often been reported in developed countries as well as developing countries. The allegedly worst outbreak of *E. coli* reported in Canada in the year 2000 was caused by *E. coli* contamination in the local water system. The outbreak occurred in Ontario claiming 7 lives and made over 2300 people ill [12]. More recently, a report on the quality of the drinking water in Pune, India indicated that 21% of the water samples taken in March 2016 from the district were contaminated and results showed the presence of harmful bacteria in those samples [13]. Yang et al. reported a global map of water-associated outbreak of infectious diseases in recent years (1991-2008), depicting the distribution of such outbreaks worldwide (figure 1.2) [14].

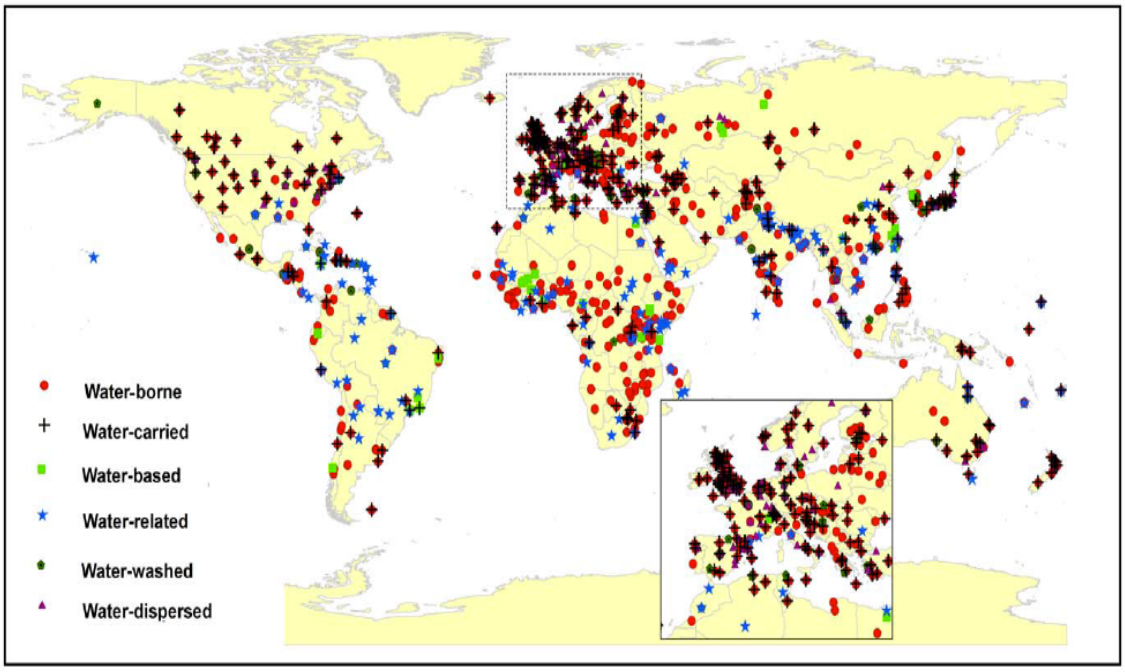

Figure 1.2. Global map of water related infectious disease outbreak from 1991 to 2008 [14].

1.2. Detection of pathogens in water

The numerous accounts of outbreaks related to contaminated water indicate the vital need for the development of tools and techniques that can be used to monitor water sources for the early detection of hazardous pathogens to prevent future outbreaks or even unlikely catastrophes. In this section we describe different methods of pathogen detection and biosensors used in water monitoring.

1.2.1. Conventional diagnostic methods

Traditional laboratory based diagnostic tools for pathogen detection still used as the gold standard for water monitoring due to their reliability, can be described as follows:

1.2.1.1. Plating and counting

In this method, cells are initially cultured with nutrients at physiologically appropriate temperatures for at least 12 h. Colony forming units (CFU) are then counted either manually or by automated cell counting methods. Petri dishes, counting chambers and grids are used to perform manual counting; flow cytometry, image analysis software or electrical resistance tools are used for automated plate counting [15,16].

1.2.1.2. Polymerase Chain Reaction (PCR)

The PCR technique was introduced in the 1980s by Kary Mullis. In this method, DNA amplification is used to detect microorganisms. Nucleic segments with defined sequences and lengths are amplified by the denaturation of strands, annealing and extension of oligonucleotide primers in repetitive cycles. The thermally stable *Thermus Aquaticus* (Taq) DNA polymerase is used for this purpose [17,18].

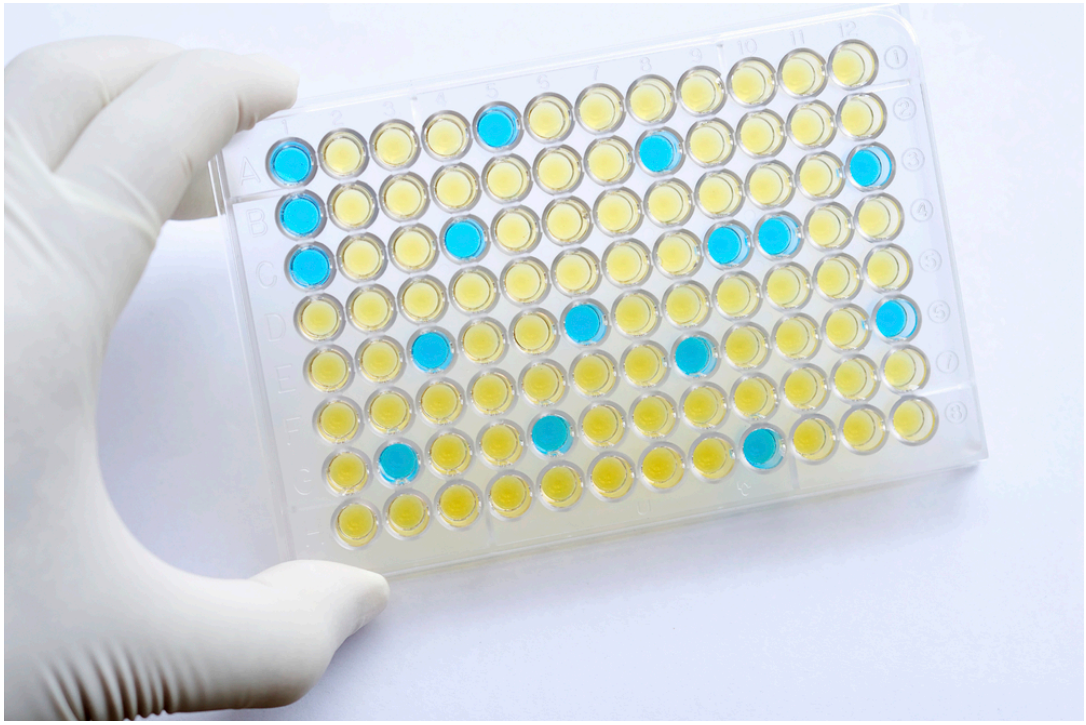

Figure 1.3. An example of an ELISA plate used for the detection of microorganisms [25].

PCR has been the object of many biosensing studies for the detection of various organisms ranging from water related pathogens like *E. coli* [19] to the very recently publicized Zika virus [20].

1.2.1.3. Enzyme-Linked Immunosorbent Assay (ELISA)

ELISA is frequently used for the detection of pathogens in the laboratory. The method is based on antibody-antigen interactions to identify the target microorganism. A specific antigen is fixed on the surface and when the specific antibody binds to the antigen, a known enzyme linked to the antibody is used to produce a signal, usually by color change [21]. ELISA is often used as a biosensor for pathogen detection [22–24]. Figure 1.3 illustrates an ELISA kit after binding has

occurred on the surface of the chambers [25]. In some cases, a sandwich assay is used where a second antibody is added by a tagged enzyme, acting as the detector antibody.

1.2.2. Emerging diagnostic methods

The gold standards for pathogen detection are effective and accurate. However, they are time consuming and can seldom be used by untrained users. For faster detection of pathogens and potential on-site monitoring of drinking water, scientists have invented modern alternative techniques. A few of these techniques are described in this section.

1.2.2.1.Optical and mechanical sensors

Biosensors based on optical methods, mechanical methods or combinations of the two have been developed that mainly consist of a biological interface, a transducer and a data acquisition unit These sensors are classified as rapid detection systems that can often be used for real-time sensing.[17]. The shorter detection time associated with these methods is owed to their sensing mechanisms and the fact that no additional overnight culturing of the pathogens is required. Here are a few of these methods:

1.2.2.1.1. Surface Plasmon Resonance (SPR)

When a metal surface is irradiated by light with an appropriate wavelength, the photons excite the free electrons of the metal. These excited electrons at an interface with an oppositely charged material undergo charge density oscillation. This oscillation creates a plasmon wave (electromagnetic or evanescent) that is maximal at the metal-ambient interface. The plasmon wave then penetrates into the ambient media, usually aqueous. As the angle of irradiation at a single wavelength surpasses a critical resonance angle, or the wavelength at a fixed angle

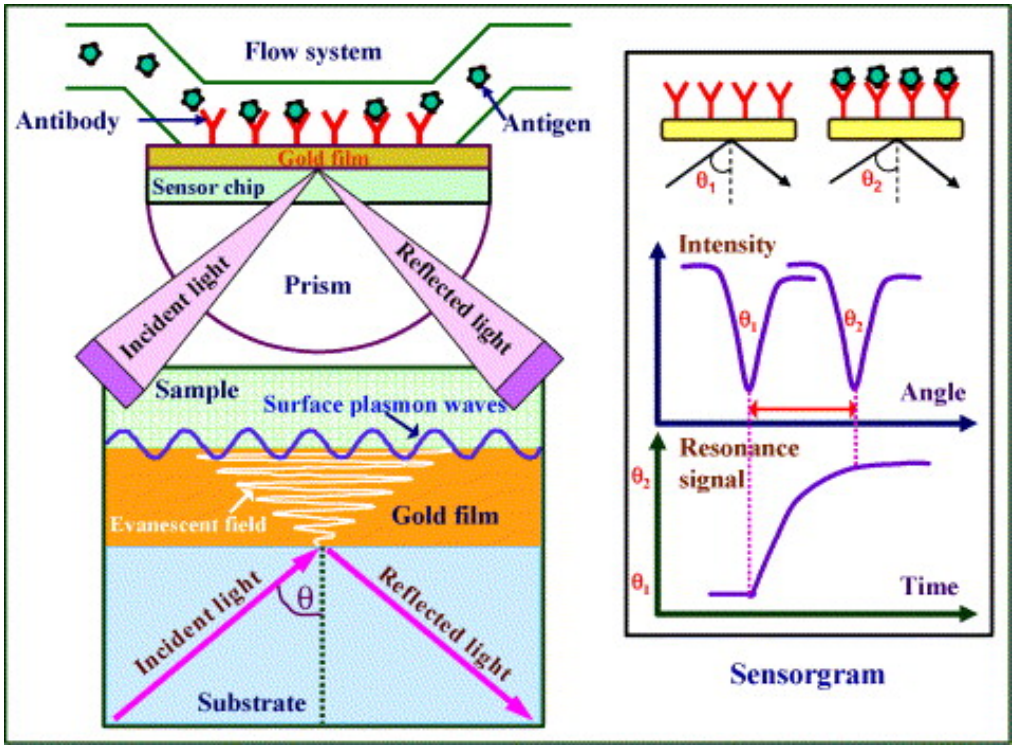

Figure 1.4. Schematic representation of an SPR sensor and output signal. The angular shift in the reflected light shows the addition of mass on the surface indicative of antibody-antigen binding [26].

surpasses the threshold, resonance is achieved. If there is additional mass attached to the surface, which is what happens for instance when antibody to antigen binding occurs, this resonance frequency shifts as a result of the change in the refractive index [17]. The change is detected by the shift in the angular position of the reflected light. Figure 1.4 represents a schematic view of an SPR system and its typical response curve as depicted by Shankaran et al [26].

Recently, Enrico et al. demonstrated the detection of *Legionella pneumophila*, responsible for Legionnaires' disease in water using an immunosensor based on SPR. In their study, the gold surface was functionalized with self-assembled Protein A and antibody was immobilized on the surface. The SPR setup was designed into a prototype by means of a microfluidics channel and

additional electronics and mechanics designed by CAD software. The results showed the successful detection of down to 10^3 CFU/ml L. pneumophila by binding to its respective antibody, here polyclonal antibody [27].

Although SPR sensors are quite versatile and very sensitive, there are still challenges that need to be addressed. The SPR transducer is sensitive to temperature drifts [17]. Antibodies can lose sensitivity with temperature rise as well. The entire system may not be cost effective and despite being commercialized, SPR is still difficult to transport for detection on-site.

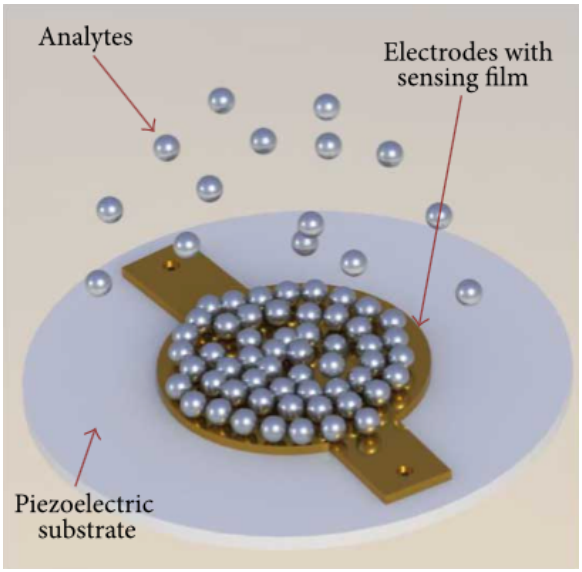

Figure 1.5. An illustration of a QCM disc comprised of a gold coated piezoelectric crystal substrate. The analyte sits on the surface and the signal changes as a result of mass adsorption [29].

1.2.2.1.2. Quartz Crystal Microbalance (QCM)

QCM sensors are bulk wave (BW) acoustic sensors. In BW acoustic sensors, applying an electric field through a transducer to the piezoresistive substrate generates an acoustic wave. The acoustic wave propagates through the material and is picked up by a second transducer converting the wave into an electric field.). QCMs, also known as thickness shear mode (TSM) acoustic wave resonators, make up the oldest acoustic wave devices originally used to monitor metal deposition rates. Applying a voltage to the QCM electrodes results in the shear deformation of the crystal. The shear propagation component of the wave renders TSM resonators a suitable candidate for biosensing applications in liquids, because a perpendicular component would be damped in liquid media [28]. That is why surface acoustic wave sensors (SAW) unlike BW sensors are not suitable for liquid sensing applications. Figure 1.5 depicts a conventional QCM sensor [29].

An example of the application of QCMs in biosensing is reported by Wan et al. who utilized functionalized magnetic nanoparticles to capture and separate sulphate-reducing bacteria (SRB) and detected the bacteria using a Ti-gold plated QCM [30].

The disadvantage of using QCM sensors emerges when attempting to increase sensitivity. QCMs typically operate at resonance frequencies in the range of 5-30 MHz and for higher mass sensitivity, higher operating frequencies are desired; to achieve that, the thickness of the crystal being used needs to decrease thus causing the sensing device to become more fragile for outside the laboratory applications [28].

1.2.2.1.3. Micro-elecrtromechanical Systems (MEMS)

MEMS are a general class of devices that convert a mechanical change into an electrical signal. Examples of the everyday applications of MEMS devices include video projectors, microphones and gyroscopes. As the name suggests, a MEMS device includes micron sized main components with microsensors that interact with different surrounding stimuli. An actuator drives the microsensor. The changes in the surrounding then lead to mechanical signals that are converted into electrical signals via the processor unit. Examples of various MEMS sensors include microcantilevers, pressure sensors, micromirror arrays (such as digital micromirror devices, known as DMD, used in projectors) and lab-on-a-chip devices for biological applications.

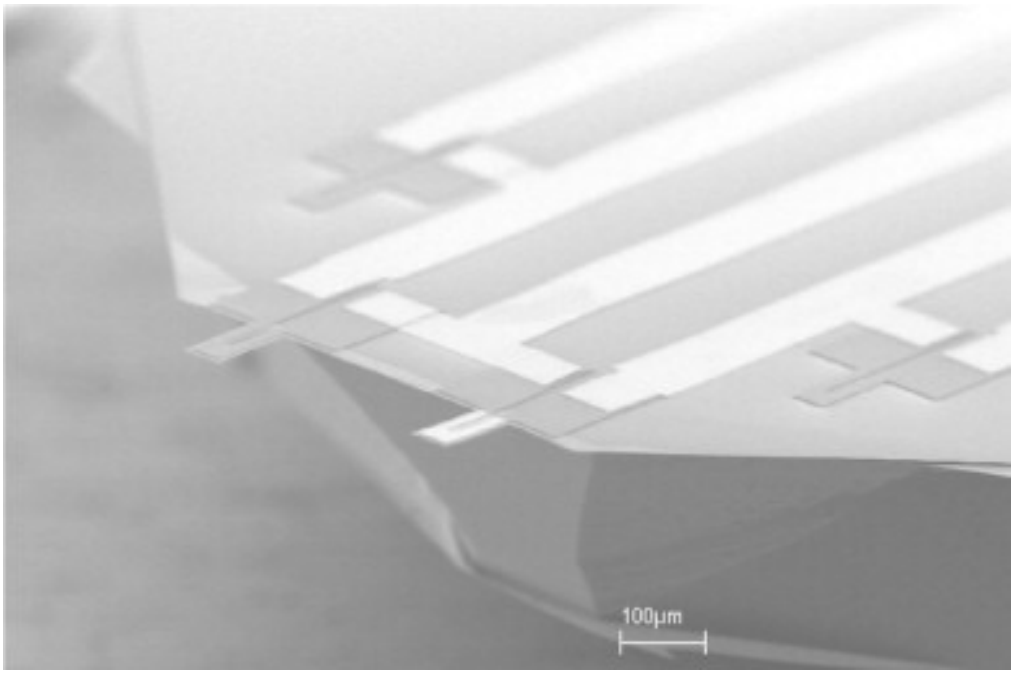

Figure 1.6. SEM image of two silicon cantilevers under magnification. The functionalized cantilevers are hanging from the base, attached to the readout system [32] .

The success of MEMS devices is due to the sensitivity arising form their small size, easy integration into electronic systems and relatively low manufacturing cost [31].

To investigate the use of MEMS for biosensing, Thundat et al. reported the application of microcantilever sensors in biosensing for a variety of biological targets. The high selectivity of these sensors is attributed to the specific surface functionalization of the cantilevers. The scanning electron microscope (SEM) image (figure 1.6) shows silicon cantilevers under magnification [32]. The challenge with microcantilevers, although quite versatile, is miniaturization of the readout system and ensuring repeatability.

1.2.2.2.Electrochemical sensors

One of the most promising categories of sensors used in pathogen detection is electrochemical sensors. The advantage of using electrochemical sensors is the direct conversion of biological processes to electronic signals. These sensors include the same structure of biosensors with a biological interface transducer and data acquisition unit. Moreover, they are cost effective, reliable, rapid and easily miniaturized [33]. They can even be integrated with MEMS devices. In this section amperometric and potentiometric electrochemical sensors are introduced as examples of electrochemical biosensors.

1.2.2.2.1. Amperometric sensors

The mechanism of biosensing via amperometric sensor devices is simply explained as detecting microorganisms by measuring the current produced by oxidation or reduction of the entity as it engages in bioaffinity reactions on the surface of the sensor [17]. Amperometric setups commonly consist of a working electrode to measure the current and a reference electrode to maintain the potential; a target specific surface is also required to act as the platform for the

biological reactions as shown in figure 1.7. The main advantage of amperometric electrochemical sensors is the ability to have compact, portable sensing devices that can be used for on-site detection with detection limits down to ppb level [34]. The linear response of these sensors with concentration also simplifies the calibration process. The drawback of amperometric devices arises from the mechanism being based mostly on oxidation/reduction processes.

Tang et al. utilized an amperometric biosensor to detect *E. coli* with a self-assembled monolayer based system. They report a sensing range of 1.6 x 10^3 to 1 x 10^7 CFU/ml. Furthermore, using a bi-enzyme configuration the limit of detection (LOD) was determined to be 9.7 x 10^2 CFU/ml [35].

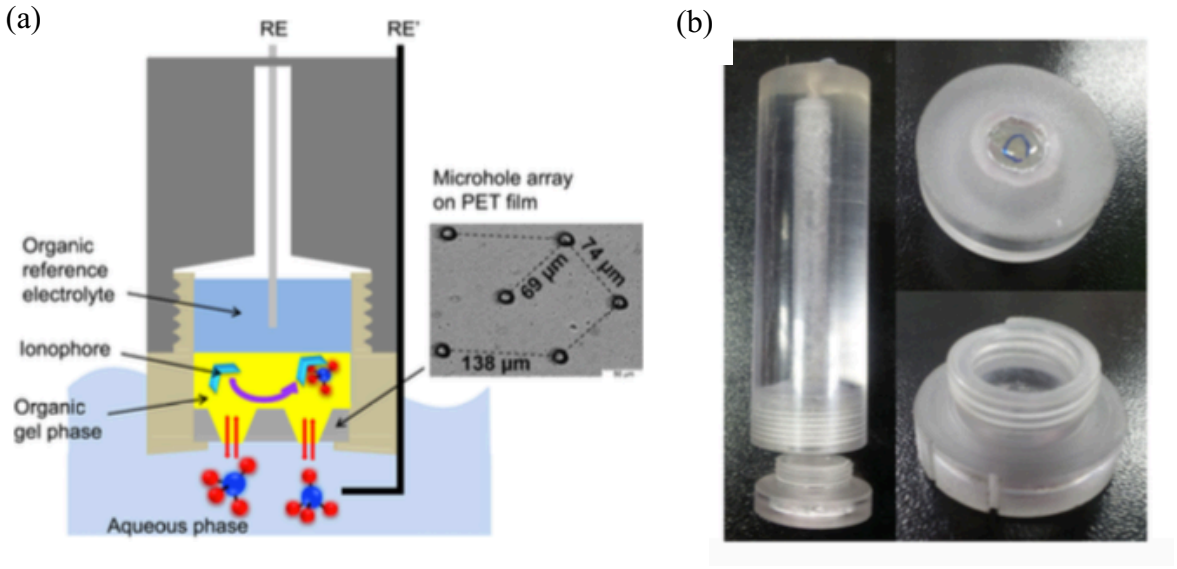

Figure 1.7. (a) A schematic representation of an amperometric sensor used for perchlorate detection in water; (b) an image of the portable sensor device [34].

1.2.2.2.2. Potentiometric sensors

Potentiometric sensors benefit from detecting the changes in potential that result from various activities that occur on the analyte/sensor interface where discrete chemistry of the surface ensures the selectivity of the system. Much like amperometric sensors, potentiometric sensors are simple by design and can be miniaturized into portable units. Field effect transistors (FETs) are often applied in potentiometric sensing systems to measure the potential changes at the gate of the FET. This makes the sensing device easier to be made compact for real time use [17].

One of the most widely used potentiometric sensors is the light addressable potentiometric sensor (LAPS). LAPS is an electrochemical sensor with a three-electrode configuration. The working electrode (WE) in this system is a semiconductor (most often Si), which is the main sensor component. The sensor is connected to a potentiostat that shows the I-V curve response of LAPS. Figure 1.8 demonstrates a scheme of a typical LAPS device.

When light is illuminated on the front side or backside of the sensor, electron-hole pairs separate under the surface of the WE at the interface with the electrolyte. When an electric field is applied, the electron-hole pairs move in the field and create a photocurrent signal. This signal is dependent on the potential of the surface of the WE, where the ion sensitive layer is, and changes in electrolyte properties such as pH alter the photocurrent response. The advantage of LAPS over other types of potentiometric sensors such as chemical field effect transistors (CHEMFETS) is the incorporation of light. LAPS can be used as a spatially sensitive system, bearing in mind that only parts of the sensor that are illuminated are responsible for the signal. Functionalizing the surface of the sensor ensures the selectivity of the sensing unit. The physics of LAPS is

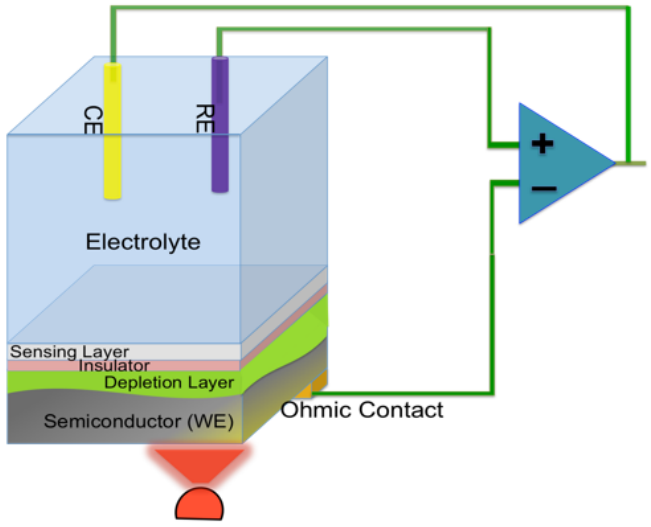

Figure 1.8. Schematic illustration of a typical LAPS system with a three-electrode configuration.

extensively explained in chapter 2. Various applications of LAPS in biosensing have been explored in the last 2 decades [36–38].

1.3. Hydrogels

The sensitive layer of the LAPS system in this work is chosen to be pH sensitive polyvinyl alcohol/poly acrylic acid (PVA/PAA) hydrogel nanofibers (NFs). For this purpose hydrogels are briefly explored in this section, with a focus on pH sensitive hydrogels and their NFs. Hydrogels are a class of polymeric materials that consist of a 3-dimentional network of polymer chains. This network is hydrophilic in nature. The components used for the synthesis of hydrogels are initially water-soluble. However, as the gel forms, it is no longer soluble in water.

1.3.1. Stimuli responsive hydrogels

In stimuli responsive hydrogels, any small alterations in the surrounding media result in a considerable change in the volume of the hydrogel network. The swelling of the hydrogel in response to an external force can lead to a volume change, up to a hundred times. On the other hand, reverse changes cause deswelling of the hydrogel by release of aqueous solutions from the polymer network. There are a number of stimuli that cause volume changes in hydrogels, including and not limited to light, pH, temperature and applied electric field.

pH sensitive hydrogels are polyelectrolytes with weak acidic or basic groups with the capability to be ionized. Hydrogels with weak acidic groups (like PVA/PAA) become deprotonated in more basic media and protonated in more acidic environments. As the hydrogel is deprotonated, like-charge density increases and the generation of mobile counterions causes a phase transition and consequent swelling. Deprotonation in hydrogels with weak acidic groups is represented in Eq.1.1.

$$[RCOOH]_{gel} + [OH^-]_{aq} \rightarrow [RCOO^-]_{gel} + H_2O \qquad \text{Eq.1.1}$$

The opposite occurs in more acidic environments and protonation causes a decrease in like-charge density and the gel shrinks (Eq.1.2):

$$[RCOO^-]_{gel} + [H^+] \rightarrow [RCOOH]_{gel} \qquad \text{Eq.1.2}$$

Figure 1.9 demonstrates the phase transition of polyelectrolyte hydrogels with changes in pH. Hydrogels with both acidic and basic groups show 2 phase transitions. The phase change is associated with the dissociation constant pK_a of the hydrogel. As the pH passes the pK_a, phase transition happens (in acidic hydrogels). Any further change in pH only increases the ionic strength of the network.

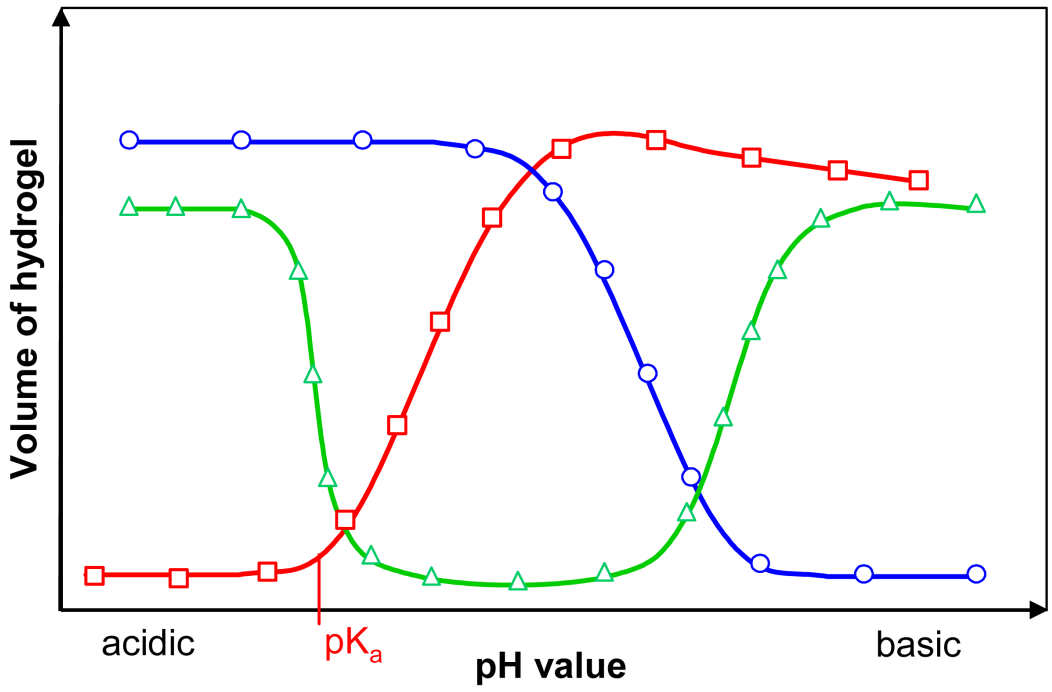

Figure 1.9. The swelling behavior of hydrogels with respect to changes in pH. In acidic hydrogels, as the pH passes the pK_a of the network a phase transition happens. Further increase in pH increases the ionic strength and reaches maximal swelling. For basic hydrogels the opposite occurs. Hydrogels with both acidic and basic groups show 2 phase transitions [39].

It is worth mentioning that due to the kinetics of hydrogel swelling, smaller hydrogel dimensions lead to higher swelling. Swelling time is proportional to the square thickness of the hydrogel as seen in Eq.1.3. In this equation τ is the swelling time constant, r is the hypothetical radius of a spherical gel and D the diffusion constant. If we consider the ionic characteristics of the buffer solution, we can obtain Eq. 1.4, which is more complex (obtaining the equation is out of the focus of this work). δ is the gel thickness, D is the diffusivity of the buffer solution, H_0 the hydration and β_{gel} and β_{HB} the buffer capacity of the hydrogel and buffer, respectively[39].

$$\tau = \frac{r^2}{D} \quad \text{Eq.1.3}$$

$$\tau = \frac{\delta^2}{\pi^2 D_{HB}}\left[1 + \frac{\beta_{gel}}{(1+ H_0)\beta_{HB}}\right] \quad \text{Eq.1.4}$$

Therefore, the idea of using NFs of pH sensitive hydrogels can drastically decrease the swelling time of the hydrogel. They can be used in a variety of applications from drug delivery to sensors.

1.3.2. pH sensitive hydrogel NFs in sensing

Hydrogel NFs offer enhanced swelling properties as opposed to the bulk form. Fabrication of NFs can be done using techniques such as electrospinning [40], self-assembly [41] and chemical methods [42]. To elucidate the importance applications of pH sensitive hydrogel NFs, two separate examples of the use of NFs in sensing are given.

Han et al. incorporated electrospun polystyrene (PS)/poly (styrene-alt-maleic anhydride) (PSMA) hydrogel NFs into a microfluidic system for the fluorescent detection of matrix metalloproteinases-9 (MMP-9), which is a key factor in vascular disease and cancer progression. Figure 1.10 shows the microfluidic sensor with the fluorescent signal of the functionalized NFs [43].

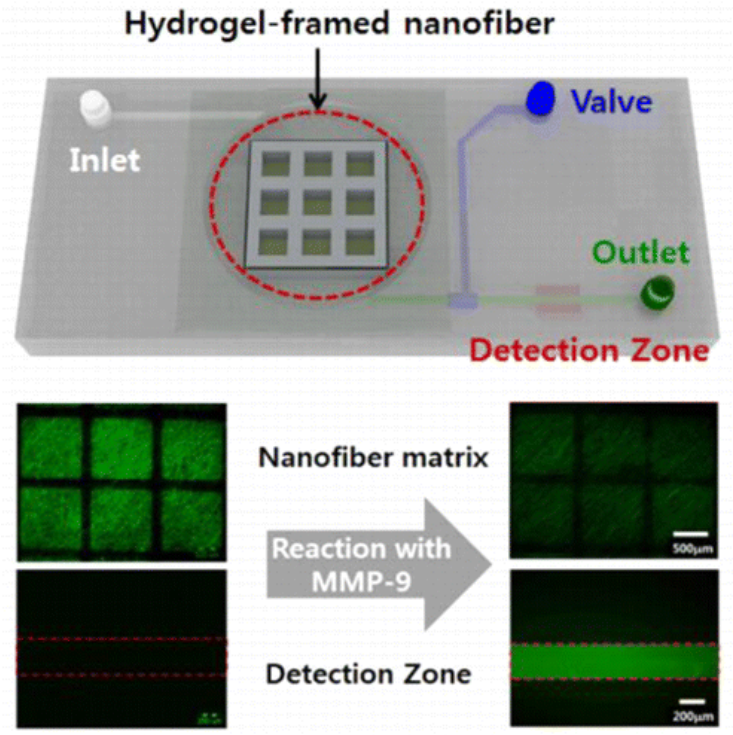

Figure 1.10. A microfluidic system coupled with PS/PSMA electrospun hydrogel NFs and its fluorescent response as a result of the presence of MMP-9 [43].

In addition, Vemula et al. used self-assembled nanofiberous gels (SAF) of tri(hydroxymethyl)aminomethane (TRIS) to detect intracellular milieu (decrease in pH). The ability of the hydrogel to detect changes in pH helps to deliver drugs more efficiently due to the simple design of the hydrogel carrier network. pHrodo dye is encapsulated in the NFs for pH modulation (figure 1.11). By using this method, the authors have provided an alternative approach to deliver molecules that are not amenable to covalent binding for drug delivery [44].

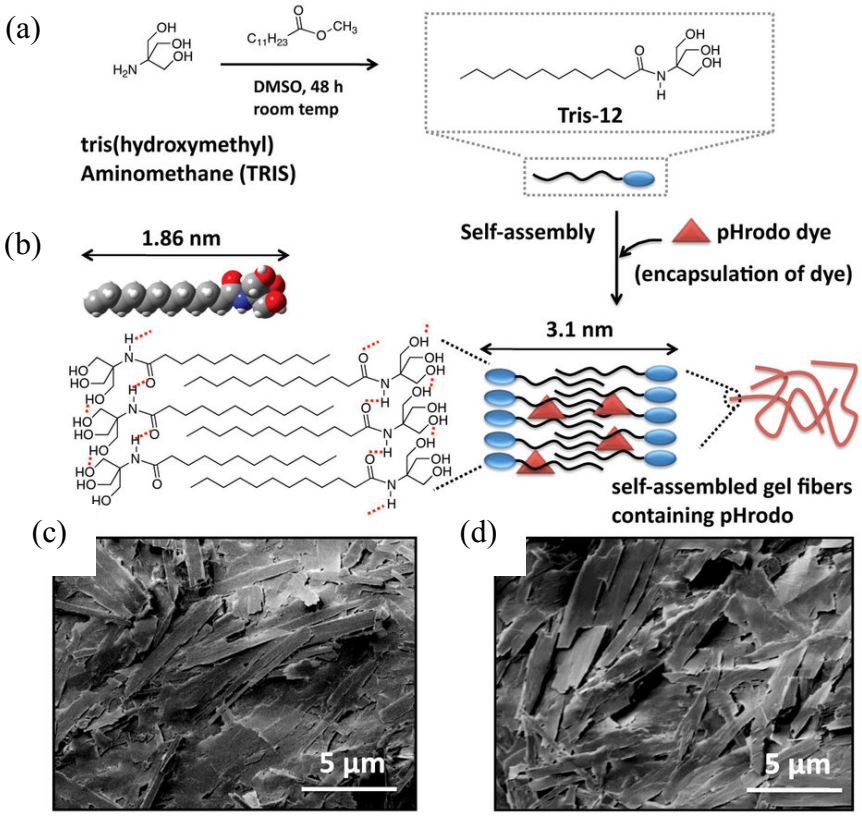

Figure 1.11. The fabrication of Tris NFs incorporated with pHrodo dye for detection of intracellular milieu. (a) and (b) show the synthesis steps and optimization of the SAF; (c) shows the SEM image of the SAF without pHrodo and (d) is the SAF with pHrodo [44].

In summary, the LAPS system, combined with the pH sensitive hydrogel layer is the perfect candidate for sensing *E. coli*. The reason for that is, compared to methods such as plating, LAPS has the capacity for detection in much shorter times of possibly an hour compared to 2 days. Compared to other techniques, LAPS can be easily miniaturized for portable usage outside the laboratory environment. It can be used in the field for onsite detection in different media. Further discussion on the abilities of this NF-LAPS system is discussed in the following chapters.

Chapter 2: Light Addressable Potentiometric Sensor (LAPS)

In this chapter, the physics of LAPS will be explored so that the sensing mechanism of the system becomes clear. Firstly, basic physical phenomena regarding semiconductors are described and then the LAPS response is elaborately explained. Despite the complicated underlying phenomena that govern semiconductors, the sensing mechanism in LAPS is quite simple. Any changes in potential on the sensing layer are reflected in the photocurrent signal. This renders the sensor very practical and versatile.

2.1. Physics of LAPS

A typical WE in a LAPS system constitutes of a semiconductor substrate (usually slightly doped), an insulating layer and a sensing layer with a discrete chemistry. A light source commonly made up of light emitting diodes (LEDs) illuminates the sensor to produce a photocurrent. A potentiostat is responsible for providing biased voltage to the system and measuring current through an electrochemical system where the sensing chip acts as the WE and the reference electrode (RE) and the counter electrode (CE) are placed in the electrolyte containing the sensing target. A schematic of such a system can be seen in figure 2.1 with a sensor chip holder that engulfs the system (similar to what was presented in figure 1.8 in chapter 1).

To better understand the physical phenomenon involved in LAPS, some fundamental concepts need to be explained. Here, some basics will be explored regarding semiconductors, semiconductor/insulator/electrolyte interfaces and charge transport phenomena.

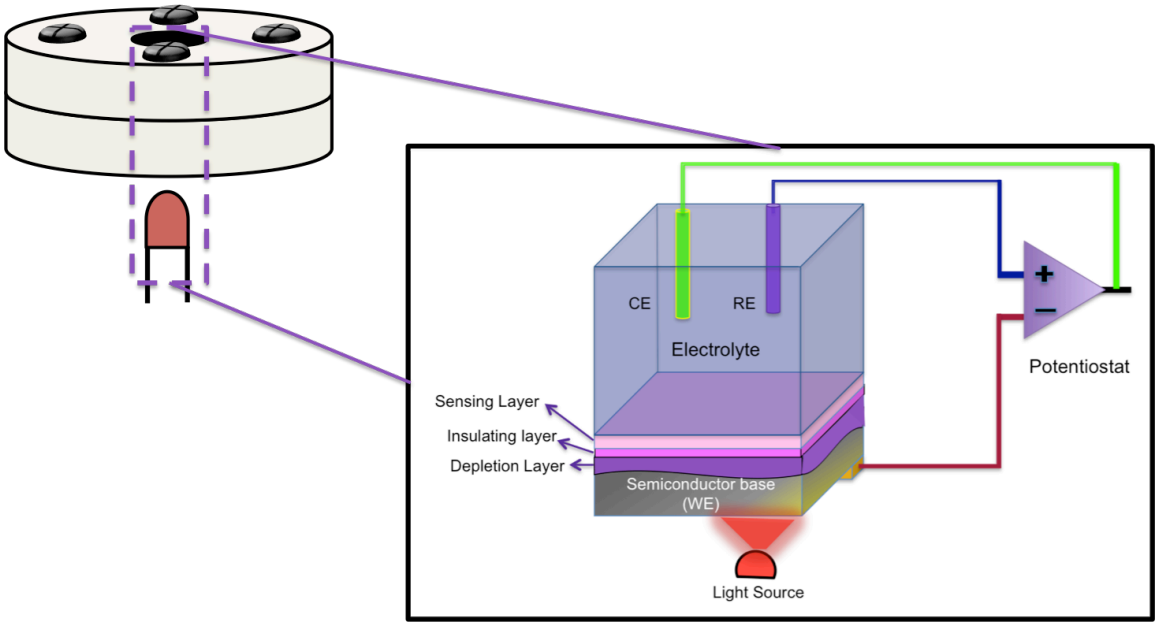

Figure 2.1. A sensor chip chamber schematic representation and a closer view of LAPS and its components. The RE and CE continue outside the chamber to a potentiostat that reads the LAPS signal.

2.1.1. Charge states in semiconductors

Materials can be divided into 3 groups based on their electrical conductivity as conductors, semiconductors and insulators. Different energy levels can be defined for all theses groups with the main energy levels being the energy of the valence band (E_v) and the energy of the conduction band (E_c). What differentiates conductors from semiconductors is the availability of electrons at different energy levels. In conducting materials as well as semiconductors, the valence band is filled with electrons; however, the conduction band in a semiconductor is inherently empty. A conductor has filled energy states in the conduction band up to the Fermi level with energy of E_f. In a semiconductor, this E_f, defined by the energy level where the possibility of an electron present is 0.5, falls in the band gap of the material between E_v and E_c.

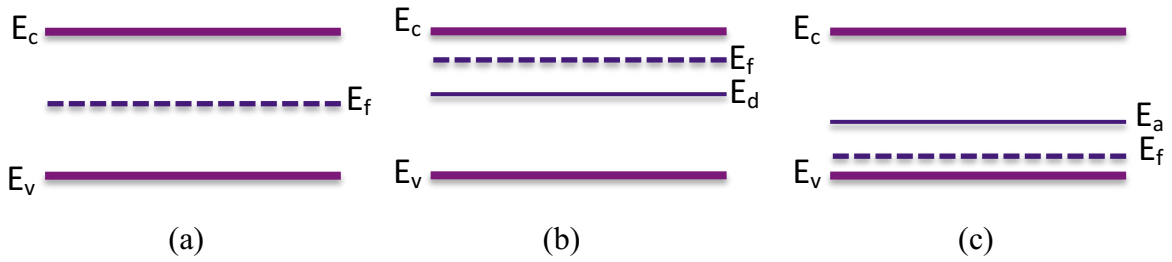

Figure 2.2. Band diagrams of an (a) intrinsic (b) n type and (c) p type semiconductor with E_c representing the energy of the conduction band, E_v valence band, E_f the Fermi level, E_d the donor level and E_a acceptor level.

Therefore, semiconductors need additional energy for electrons to flow into the conduction band. This additional energy can be provided by means of thermal energy, field emission especially in the form of light and thermal vibrations. Electrons and holes are generated through this addition of energy and electrons can move into the conduction band leaving behind holes.

In the case of extrinsic semiconductors, donor or acceptor atoms are added to the system. These atoms will provide electrons (or holes) with quantized energy, even at T=0 k, so that the Fermi level of the semi conductor will no longer be situated in the middle of the band gap resulting in extrinsic n type or p type semiconductors (figure 2.2).

2.1.2. Band bending in semiconductors

When a semiconductor forms a junction with other materials like metals, band bending can occur to reach equilibrium at the energy levels. When a semiconductor is in contact with a metal, since the work function (ϕ) of the semiconductor is different from that of the metal, charge transfer occurs between the two materials. The work function of materials is defined as the energy required for moving an electron from the Fermi level of a material into the vacuum. When two

materials, in this case a metal and a semiconductor, have different work functions, transfer of charges can occur to compensate for the difference between the work functions of the materials so that the electrons would require less energy to be moved to vacuum. In other words, the two materials will be more stable thermodynamically. This transfer of charges creates a field between the semiconductor and the metal. Since the number of free charge carriers in the semiconductor (up to10^{18} cm^{-3}) is smaller than that of metals (10^{23} cm^{-3}), the field is not well screened in the semiconductor and a space charge region is formed near the surface of the semiconductor. In this space charge region, the band edges can shift upwards or downwards due to the charge transfer, depending on the relative position of the Fermi energy levels. In other words, depending on the different work functions of the semiconductor and metal, the band edges bend. Reported work function values of some materials that may be used in LAPS systems can be found in table 2.1.

If we consider an n type semiconductor, when the work function of the metal is lower than the semiconductor ($\phi_m < \phi_{sc}$), which means the Fermi level of the metal is at a higher state compared to the semiconductor, downward band bending occurs for the Fermi levels to match. Charge

Table 2.1. Work functions of different materials that can be used in LAPS.

Semiconductor	ϕ_{sc} (eV)	Metal	ϕ_m (eV)	References
Silicon (Si)-Intrinsic	4.95	Gold (Au)	5.1	[45]
Germanium (Ge)-Intrinsic	5.15	Aluminum (Al)	4.28	[45]
Gallium Nitride (GaN)	4.1	Titanium (Ti)	4.33	[45], [46]
Titanium Dioxide (TiO_2)-Rutile	4.7-5.8 (Treatment dependent)	Chromium (Cr)	4.44	[45], [47]

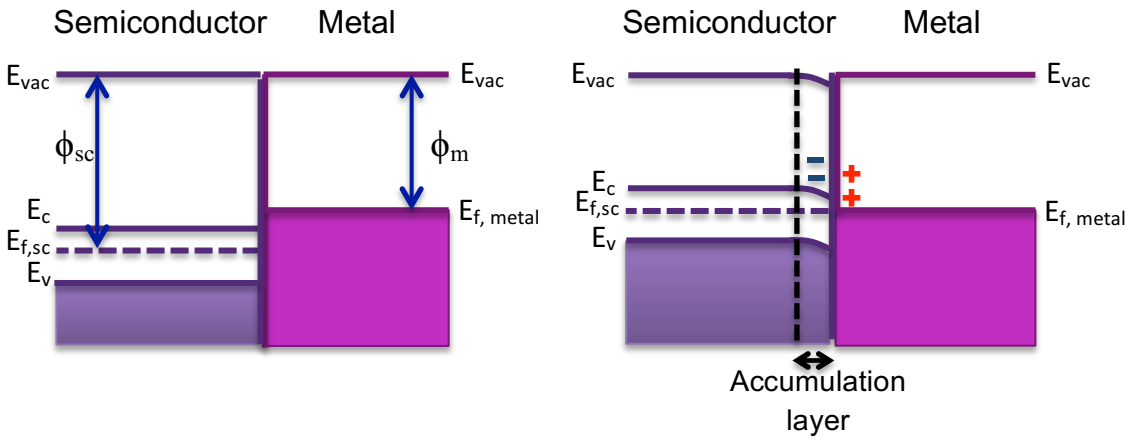

Figure 2.3. Downward band bending in an n type semiconductor in junction with a metal having a lower work function than the semiconductor. Electrons flow from the metal to the semiconductor and accumulate in the space charge region.

transfer due to the induced electric field causes the electrons to flow from the metal to the semiconductor and the semiconductor will be in a state of accumulation (figure 2.3).

In downward band bending, the Fermi level of the semiconductor gains energy to match the Fermi level of the metal. Since the relative positions of the electronic states of the semiconductor remain constant and the band gap of the material cannot change, the valence and conduction bands of the semiconductor also shift in energy. This shift does not happen at the edges of the energy bands due to the fact that the band edges are pinned to the surface and the electric field caused by the contact causes the downward bending of the bands. This type of contact is known as ohmic contact between metal and semiconductor.

When the work function of the metal is bigger than that of the semiconductor however ($\phi_m > \phi_{sc}$), the space charge region has extra positive charge and electrons flow from the semiconductor to the metal, thus causing a depletion layer that is assumingly free of charge and hence depleted of charges. It should be noted that the number of charges in the depletion layer is not really zero, but that in fact there is no current density in that region (figure 2.4).

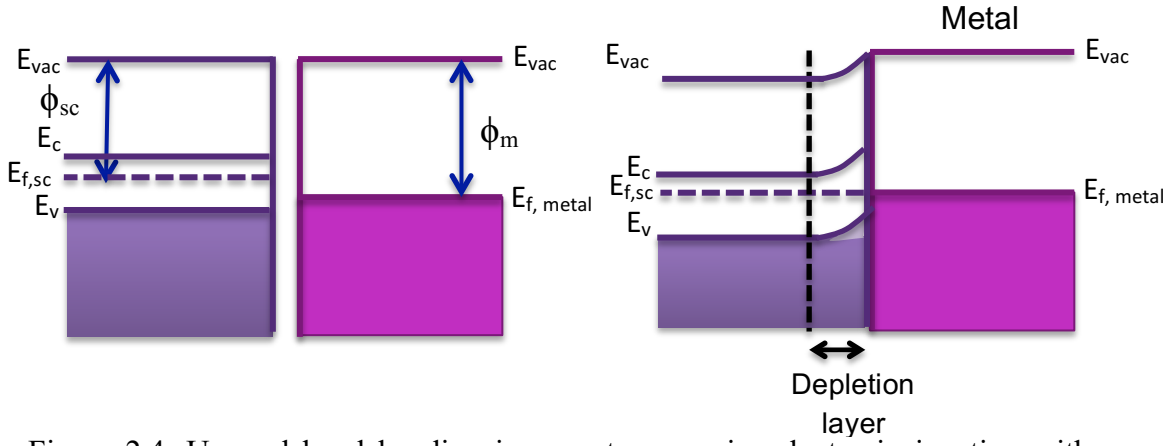

Figure 2.4. Upward band bending in an n type semiconductor in junction with a metal having a higher work function than the semiconductor. Electrons flow towards the metal and a depletion layer is created.

The formation of the depletion layer is accompanied by the upward bending of the energy bands since the Fermi level of the semiconductor is at a higher state and equilibrium is reached as the Fermi levels match. The n type semiconductor in depletion is depleted of electrons; therefore an energy barrier is formed between the semiconductor and the metal called the Schottky barrier [48].

Considering the values for different work functions of materials, one can predict the nature of the contact between a metal and a semiconductor. For example, one would predict that aluminum would probably form an ohmic contact with silicon (depending on the doping) or that gold would probably form a Schottky barrier with gallium nitride. Having said that, experimental data does not always follow predictions based on theory due to factors such as the presence of surface states, change in surface morphology or even the diffusion of the adhesion layer into the semiconductor when a metal contact is deposited on the semiconductor.

It should be mentioned that in a p type semiconductor, the majority of charge carriers are holes and therefore the depletion layer forms when band bending is downwards, or when the space charge region is depleted of holes. If there is no difference between the work functions of the semiconductor and the metal before contact, the energy bands lie flat and there is no band bending. The semiconductor is then at a flat band state.

Band bending can also happen when a voltage is applied to the semiconductor connected to a metal (field effect band bending). For an n type semiconductor, if a positive voltage is applied (relative to the flat band potential which will be explained), accumulation will occur and if a negative voltage is applied, the semiconductor will be in a state of depletion.

If the voltage applied to the semiconductor compensates for the work function difference between the semiconductor and the metal (or even an electrolyte), that is to say the Fermi level of the semiconductor is elevated to the Fermi level of the metal, there will be no need for band bending to occur; such an applied voltage is referred to as the flat band voltage or the flat band potential.

2.1.3. Width of the depletion layer

Before the width of the depletion layer is calculated, some considerations towards the accumulation layer need to be taken into account. Firstly, charges flow from the semiconductor bulk to the semiconductor surface in accumulation because the Fermi level is closer to the conduction band near the surface (for an n type semiconductor). The density of the electrons near the surface can then be described as:

$$e_s = N_d \exp(-\frac{qV_{bb}}{kT}) \qquad \text{Eq. 2.1}$$

in which e_s is the concentration of the electrons at the surface, N_d is the number of donor atoms, V_{bb} is the band bending potential, qV_{bb} is the band bending energy, k the Boltzman constant and T is the absolute temperature (adapted from [49]). The width of the accumulation layer differs with the width of the depletion layer due to the fact that the distribution of charges is different in the two cases. The typical width of the accumulation layer is under 10 nm and at times neglected.

For a LAPS system, photocurrent is generated when a semiconductor is illuminated as it is in depletion. Therefore the width of the depletion layer will be of importance. For an n type semiconductor, if we assume that the electrostatic charges on the surface of the semiconductor space charge region and the surface of the metal (or an electrolyte) create a field, the electric field is the gradient of the electric potential. Then we have:

$$E = -\nabla\phi \qquad \text{Eq. 2.2}$$

the electric field can be written as (Gauss's law):

$$\nabla . E = -\frac{\rho}{\varepsilon_0 \varepsilon_r} \qquad \text{Eq. 2.3}$$

where ρ is the space charge density, ε_0 is the vacuum dielectric constant and ε_r is the dielectric constant of the semiconductor (assuming that the space charge region acts as a capacitor and assuming a schottky approximation). Therefore, the electric potential in the depletion layer can be calculated by solving the Poisson equation:

$$\nabla^2\phi = -\frac{\rho}{\varepsilon_0 \varepsilon_r} \qquad \text{Eq. 2.4}$$

Under the assumption that the potential energy of the charges is only changing in one direction, i.e. assuming that the interface is of infinite surface, the potential can be derived for the direction of the height (z) where the semiconductor surface height is considered as 0. So we can rewrite Eq. 2.4 as:

$$\nabla^2 V = -\frac{\rho}{\varepsilon_0 \varepsilon_r} \qquad \text{Eq. 2.5}$$

where V is the band bending potential defined as:

$$V_{bb}=V_{app}-V_{fb} \qquad \text{Eq. 2.6}$$

in which V_{app} is the applied potential and V_{fb} is the flat band potential. Let us consider the width of the depletion layer to be W. The charge density is then defined as the number of donor ions N_d (depletion layer is depleted of electrons) multiplied by the charge of a single charged particle q:

$$\rho = qN_d \qquad (0 \leq z \leq w) \qquad \text{Eq. 2.7}$$

This is true for any point inside the depletion layer, and if we assume for simplicity that the positive charges (holes) are not present beyond the depletion layer, then:

$$\rho = 0 \qquad (z > w) \qquad \text{Eq. 2.8}$$

From integrating Eq. 2.3, the electric field in the depletion becomes:

$$E = \int -\frac{\rho}{\varepsilon_0 \varepsilon_r}\, dz = -\frac{\rho}{\varepsilon_0 \varepsilon_r}\, z + C_1 \qquad \text{Eq. 2.9}$$

since the field is 0 at the boundaries of the depletion layer:

$$E\,(z = w) = 0 \qquad \text{Eq. 2.10}$$

therefore:

$$E = -\frac{\rho}{\varepsilon_0 \varepsilon_r}\, z + \frac{\rho}{\varepsilon_0 \varepsilon_r} w = \frac{\rho}{\varepsilon_0 \varepsilon_r}\, (w - z) \qquad \text{Eq. 2.11}$$

Then the electric potential would be:

$$V = \int \frac{\rho}{\varepsilon_0 \varepsilon_r}\, (w - z) dz = \frac{\rho}{\varepsilon_0 \varepsilon_r}\, wz - \frac{\rho}{2\varepsilon_0 \varepsilon_r} z^2 + C_2 \qquad \text{Eq.2. 12}$$

The band bending potential, as defines in Eq. 2.6, is applied to the depletion layer such that the potential in the bulk is assumed to be zero:

$$V\,(z = w) = 0 \qquad \text{Eq. 2.13}$$

and thus:

$$V = \frac{\rho}{\varepsilon_0 \varepsilon_r}\, wz - \frac{\rho}{2\varepsilon_0 \varepsilon_r} z^2 - \frac{\rho}{\varepsilon_0 \varepsilon_r} \frac{w^2}{2} \qquad \text{Eq. 2.14}$$

which by applying Eq. 2.7 throughout the width of the depletion layer can be rewritten as:

$$V = -\frac{qN_d}{2\varepsilon_0\varepsilon_r}(z-w)^2 \qquad 0 \le z \le w \qquad \text{Eq. 2.15}$$

from Eq. 2.6 and Eq. 2.15, the width of the depletion layer is [49]:

$$w = \sqrt{\frac{2\varepsilon_0\varepsilon_r(V_{app}-V_{fb})}{qN_d}} \qquad \text{Eq. 2.16}$$

this width, depending on the practical conditions, can be in the range of tens of nm to a few μm [50].

2.1.4. Charge states in electrolytes

Having explained the charge transfer in a semiconductor, one should bear in mind that an electrolyte behaves differently from a metal. In an electrolyte, charge transfer is done by means of ions in the electrolyte. At the interface of the electrolyte with an electrode, which can be a solid or liquid metal, a semiconductor or even carbon, the charges existing near the interface form what is called an electric double layer. The electrode/electrolyte interface, that can be described as a double layer capacitor at any applied potential (although the two charged surfaces are not completely distinct) with a capacitance of C_{dl}. This capacitance, unlike for real capacitors, can change with the applied potential and is in the order of 10-40 μF/cm^2 [51]. Theoretically, the charge on the electrolyte side should equal that of the electrode side and are often used as charge density.

The electrolyte side of the double layer consists of many layers. The layer near the electrode surface is called the Helmholtz layer and the layer following the Helmholtz is called the diffuse layer (figure 2.5). This is all valid for higher ionic concentrations in the electrolyte. At lower ionic concentrations, a gouy layer can be defined that is not the focus of this report.

The Helmholtz layer itself is composed of an inner Helmholtz layer and an outer Helmholtz layer. The inner Helmholtz layer consists of adsorbed ions or molecules near the interface with a charge density in the orders of $\mu C/cm^2$. The length of this layer is controlled by the center of the specifically adsorbed ions. The outer Helmholtz layer includes the solvated ions surrounded by the molecules of the solvent. The solvated ions, or nonspecifically adsorbed ions, interact with the charges of the electrode only in a long range electrostatic fashion. Due to the thermal aggitations in the electrolyte, the nonspecifically adsorbed ions distribute throughout the solution in the diffuse layer [51]. The diffuse layer length changes with the ionic strength of the solution.

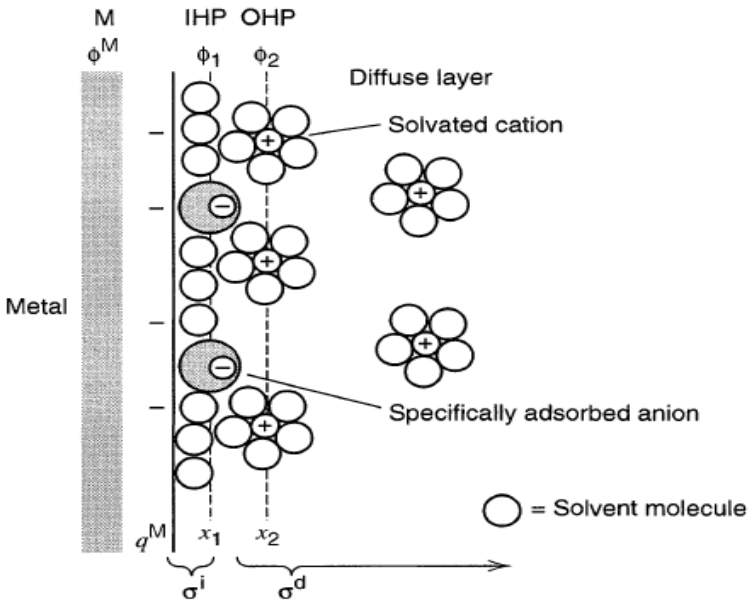

Figure 2.5. Schematic representation of the double layer at the electrode/electrolyte interface on the side of the electrolyte [51].

The electronic states in an electrolyte can be classified as reduced states (filled states), oxidized states and the redox potential state (electrochemical potential) which is the equivalent of the fermi level for the electrolyte. The distribution of the electronic states is often described with a Gaussian distribution as follows:

$$D_{ox} = \exp(-\frac{(E-E_{redox}-\lambda)^2}{4kT\lambda}) \quad \text{Eq. 2.17}$$

$$D_{red} = \exp(-\frac{(E-E_{redox}+\lambda)^2}{4kT\lambda}) \quad \text{Eq. 2.18}$$

in which E_{redox} is the redox energy level of the electrolyte, k the Boltzman constant, T temperature and λ is defined as the reorganization energy of electron transfer (solvent reorganization energy) [52]. The position of the redox energy level is determined by where the reduced and oxidized state distributions coinside and can be explained by the Nernst equation (Eq. 2.19) when the activity (or concentration) of the oxidized and reduced species are considered [53]. In Eq. 2.19, n is the number of charges transferred and F is the Faraday constant.

$$E_{redox} = E^0_{redox} + \frac{RT}{nF} ln \frac{[c_{ox}]}{[c_{red}]} \quad \text{Eq. 2.19}$$

The same can be expressed in terms of electrochemical potential since E= μ/e :

$$\mu_{redox} = \mu^0_{redox} + RTln \frac{[c_{ox}]}{[c_{red}]} \quad \text{Eq. 2.20}$$

Standard electrochemical potentials are commonly given compared to a normal hyderogen electrode [52].

The importance of energy states is discussed in the next section.

2.1.5. Electrolyte-semiconductor interface

The behavior of the electrolyte in contact with a metal is different from its contact with a semiconductor since the charge carrier density is lower in semiconductors. When an electrolyte is in contact with a semiconductor, if the fermi level of the semiconductor and the redox potential of the electrolyte do not match, band bending occurs in the semiconductor until equilibrium is reached by charge transfer (figure 2.6). The direction of band bending would still depend on the position of the redox potential compared to the fermi level of the semiconductor.

Band bending in the semiconductor, in contact with an electrolyte also happens when voltage is applied between the semiconductor (from an ohmic metal contact) and the RE, in the electrolyte.

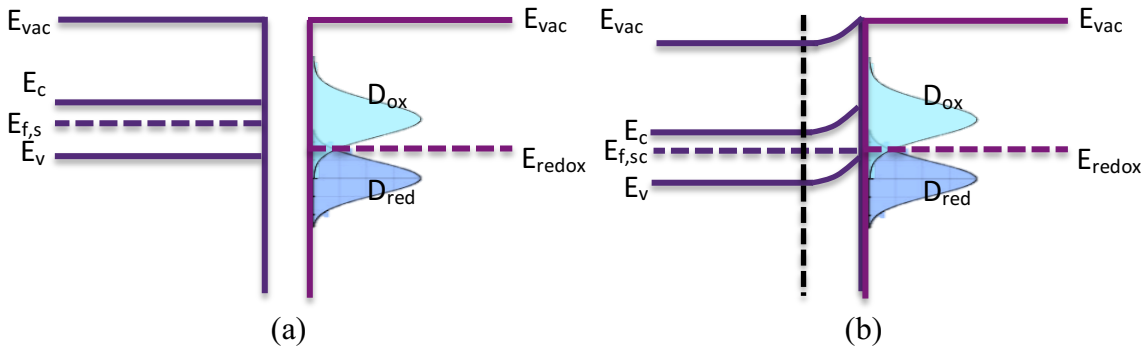

Figure 2.6. Upward band bending for an n type semiconductor (a) before contact (b) after contact with an electrolyte with a redox potential lower than the Fermi level of the semiconductor.

Change in the solution pH will result in different band bending energy values since the redox potential in the system changes by the change in H^+ ions concentration.

The potential profile along such a junction can be described in figure 2.7; however, the inner Helmholtz layer has a different capacitance than the outer Helmholtz layer and therefore there is a slight change in the potential before reaching the interface. U_R indicates the potential of band bending, U_{Ga} the band gap potential, U_H the Helmholtz potential and U_G represents the diffuse layer (gouy) potential [54]. The Helmholtz layer is considered to be free of charge.

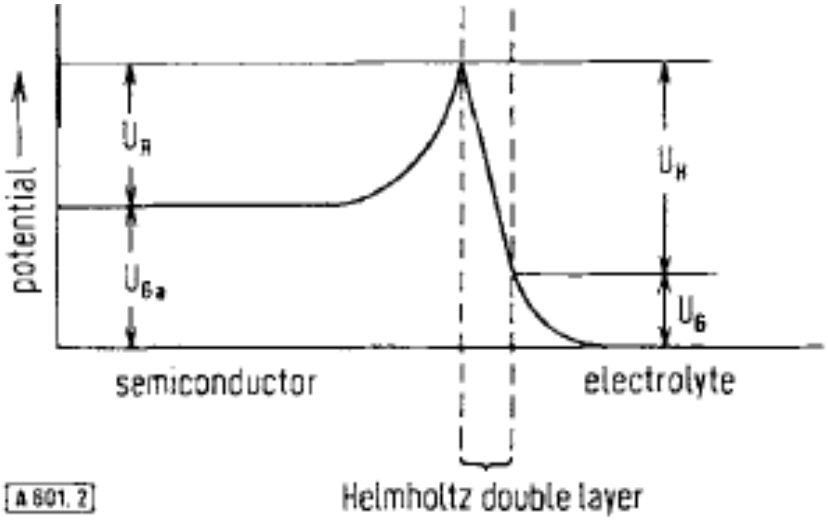

Figure 2.7. Distribution of potential throughout the semiconductor and electrolyte in contact. The inner and outer Helmholtz layers have different potentials [54].

2.1.6. Electrolyte-insulator-semiconductor connection

Let us assume that the insulating layer, like the natural oxide layer on the semiconductor, completely blocks all charge transfer. In this case, the electrostatic charge phenomena will be dominant. The insulating layer will be free of charge and therefore the potential will drop linearly from one side of the insulating layer to the other. A schematic representation of the potential profile when an insulating layer separates the semiconductor and electrolyte can be seen in figure 2.8 where the semiconductor is in a state of depletion. The drop in the potential across the capacitance created by the inner Helmholtz layer is too small to show. It is worth mentioning that the capacitance of the electric double layer in the electrolyte is larger than the capacitance of the semiconductor space charge region.

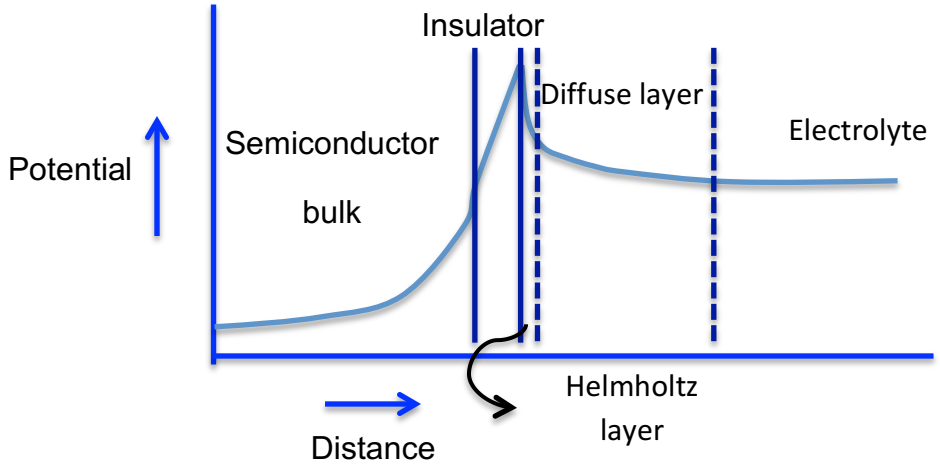

Figure 2.8. Schematic representation of the potential profile across the semiconductor, insulator, electrolyte in contact.

2.1.7. Photoeffect

Let us consider a LAPS system where the semiconductor is covered by an oxide layer and the electrolyte is in contact with the semiconductor oxide layer. As light is shone on the semiconductor with an energy equal to or greater than the semiconductor band gap energy, electrons and holes are generated. Electrons gain energy to move into the conduction band and holes will be left in the valence band. The electric field generated by the applied voltage to the LAPS system will separate the electrons and holes (bearing in mind that band bending has also created an electric field when the semiconductor/insulator come into contact with the electrolyte). The movement of the separated charges in the field alongside the drift current produced by the movement of charges from the semiconductor bulk to the surface will create a photocurrent. Figure 2.9 represents the schematic separation and movement of charge carriers when the semiconductor is illuminated for an n type semiconductor.

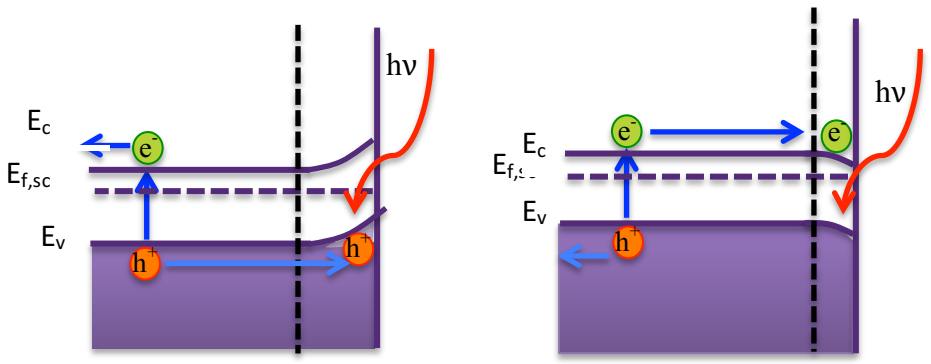

(a) (b)

Figure 2.9. Illustration of charge separation in the electric field when the semiconductor is under illumination for an n type semiconductor in (a) depletion and (b) accumulation.

If the semiconductor is in a state of accumulation, electron hole pair recombination happens too quickly for the photocurrent to be measured and there is virtually no total current. When the semiconductor is in a state of depletion however (in reverse bias), the generated photocurrent can be measured.

Two competing currents appear in the semiconductor even with no illumination. Drift current is defined as the movement of the charges (both majority and minority charge carriers) as a result of the electric field. On the other hand, the diffusion current happens due to the gradient in the concentration of the charges from surface to the bulk and vice versa (Figure 2.10). If illumination is continuous, not only will recombination of the electrons and holes diminish the photocurrent, but the diffusion of the charge carriers back into the semiconductor bulk will cause the net current to decay to zero as it cancels out the drift current.

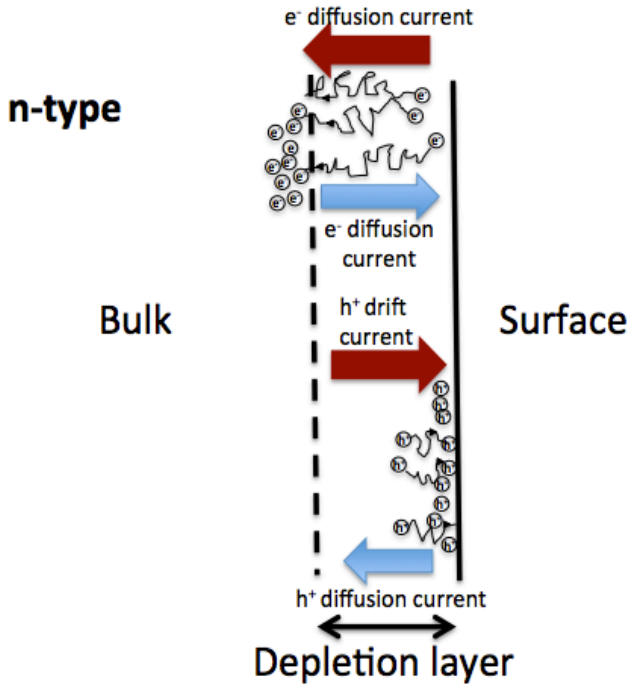

Figure 2.10. Schematic illustration of the diffusion current and drift current in an n type semiconductor.

As the light is turned off, the diffusion current will dominate and current will be generated in the opposite direction (figure 2.11(a)). To avoid the transient decay of the photocurrent and to ensure faster measurements, light is normally modulated in a LAPS setup and an alternating photocurrent will be produced as electron holes are generated, separated in the field and recombined (figure 2.11(b)) [55].

Using light illumination is an advantage for the LAPS system since it makes the sensing system spatially sensitive. This means that the photocurrent that is measured is only produced where light is illuminated and that is where the sensing has occurred. Next, the dependence of the generated signal on the pH of the solution is discussed.

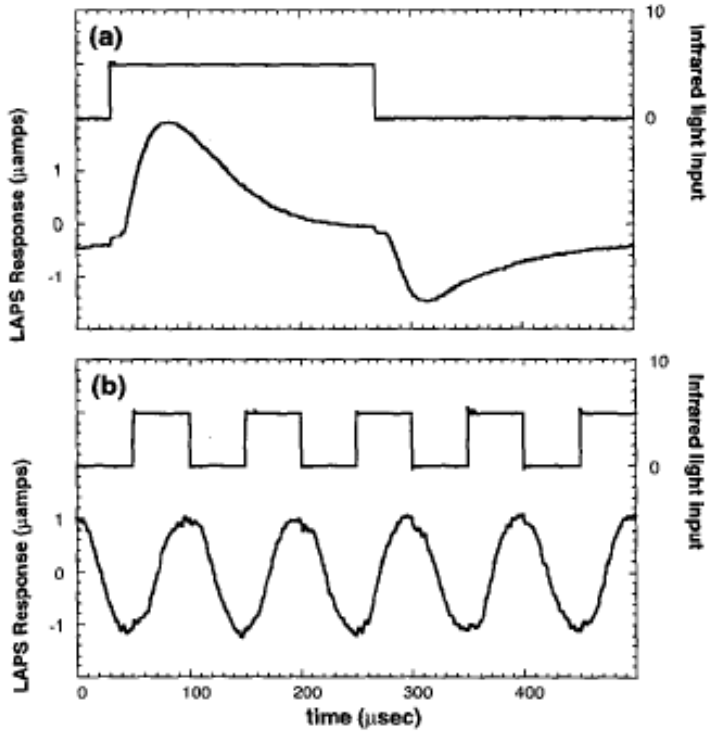

Figure 2.11. (a) Generation of photocurrent with continuous illumination in a LAPS system. Photocurrent decays as diffusion current overcomes drift current and as light is turned off, diffusion current becomes dominant; (b) Generation of an alternating photocurrent as light is modulated in a LAPS setup [55].

2.1.8. LAPS response

The semiconductor substrate of the LAPS system is driven from accumulation to depletion (and vise versa depending on the type of semiconductor) while biased voltage is applied between the semiconductor and the electrolyte, through the reference electrode. As light is irradiated, the ammeter or potentiostat measures the generated photocurrent. Typical photocurrent profiles for n and p type semiconductors are depicted in figure 2.12. The inflection point of the photocurrent versus the applied voltage curve shows the flat band potential. For an n type semiconductor, any voltage smaller (more negative) than the flat band potential drives the semiconductor into depletion and any voltage bigger (more positive) will drive the semiconductor to accumulation and cause the photocurrent to decrease (figure 2.12(a)). For a p type semiconductor this happens the opposite way (figure 2.12(b)).

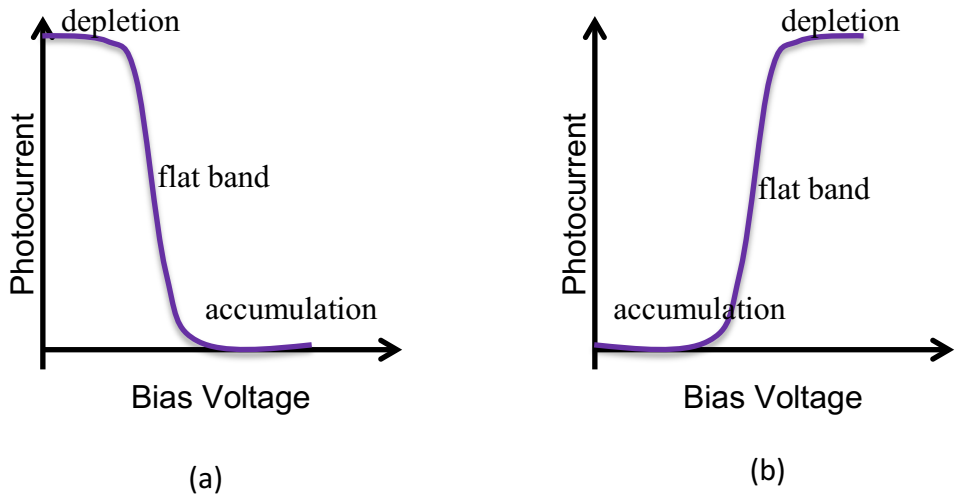

Figure 2.12. Typical photocurrent response of a LAPS system for (a) an type semiconductor (b) a p type semiconductor substrate.

The pH dependence of the LAPS system is attributed to the change in the redox potential of the electrolyte (E_{redox}) that in turn changes the flat band potential of the system. According to the Nernst equation introduced earlier (Eq. 2.19), 1 unit change in pH results in 59 mV of change in the redox potential as follows:

$$E_{redox} = E^0_{redox} + \frac{RT}{nF} ln \frac{[c_{ox}]}{[c_{red}]} \qquad and \qquad pH = -\log[H^+] \qquad \text{Eq. 2.21}$$

The Faraday constant is 96485 C/mol and n is considered 1 for 1 mol of charge transfer. Thus, at room temperature we have:

$$\Delta E_{redox} = 2.303 \frac{8.314 \times 298}{1 \times 96500} = 0.059\, V \qquad \text{Eq. 2.22}$$

It is worth mentioning that the response can be super-Nernstian (over 59 mV/pH) if the ion activity on the surface is different from the activity in the bulk (lower on the surface) as a result of localized ion depletion [56]. This can be attributed to surface properties of the material used (such as the hydrogel NFs used here where H^+ ion concentration varies locally when the NFs swell and deswell).

The change in the flat band potential can be traced through the shift of the photocurrent curves at the inflection point. An example of this shift is illustrated in figure 2.13 for a p type semiconductor in a LAPS system. The profile of the LAPS response deals with a complex relationship between the photocurrent and the biased voltage but different computational and modeling works have been conducted to try and explain this behavior. If we take into account only the inflection point of the profile, the voltage of the inflection (for a p type semiconductor) can be more accurately described by:

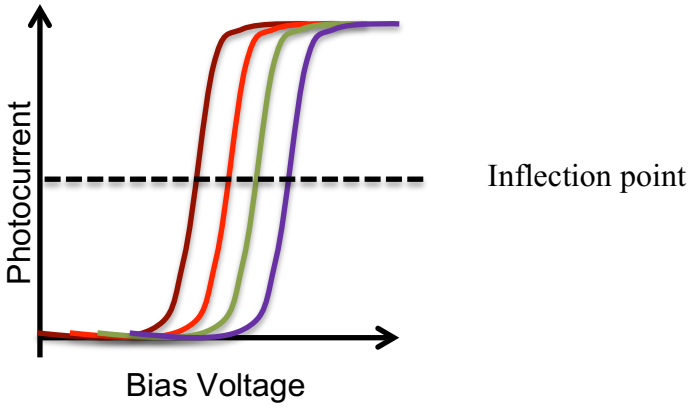

Figure 2.13. Shift in the photocurrent curve with change in the electrolyte pH for a LAPS system with a p type semiconductor. The shift in the inflection point shows the change in the flat band potential.

$$V_{ip} = V_{fb} + V_{bb} + \frac{\sqrt{2\varepsilon_r V_{bb} q N_a}}{C_i} \qquad \text{Eq. 2.23}$$

in which V_{ip} represents the voltage of the inflection point, N_a is the number of acceptor atoms (dopants) and C_i is the capacitance of the insulating layer [57]. Overall, the last term represents the voltage that is applied to the insulating layer, but the charge is attributed to the semiconductor as a capacitor in series with the insulator.

In order to understand the shape of the I-V curves illustrated in Figure 2.13, different models have been proposed; however, one of the most intuitive models was introduced by Sartore et al. [58]. Figure 2.14(a) and 2.14(b) show a schematic of a LAPS device and the equivalent circuit, respectively, which was developed based on the semiconductor/insulator layer interface and insulator/electrolyte interface.

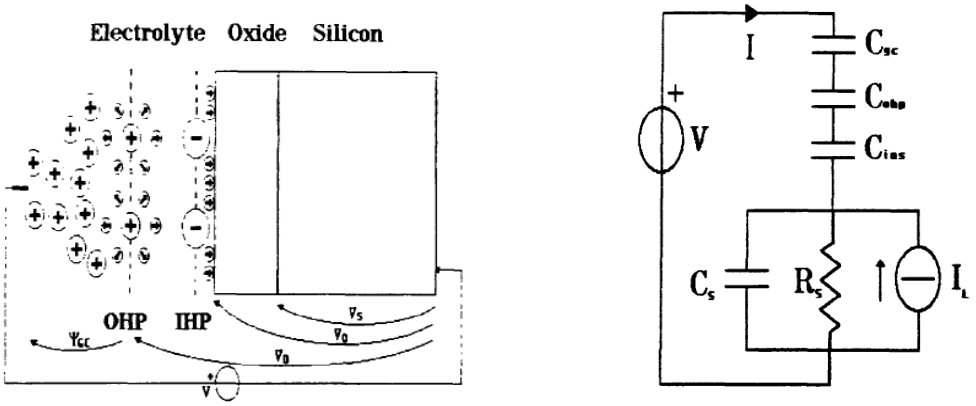

(a) (b)

Figure 2.14. (a) Schematic of a LAPS structure showing the interface between the semiconductor, insulator and the electrolyte. (b) The equivalent circuit of a LAPS structure [58].

In this work, the current for the equivalent circuit has been calculated based on the equivalent capacitance and impedance modeled in figure 2.15 to be:

$$|I| = \sqrt{2}\frac{\omega R_S C_{EL}}{\sqrt{[1+\omega^{\omega 2} R_S^2 (C_S + C_{EL})^2]}} \qquad \text{Eq. 2.24}$$

Changes in solution pH change the value of C_{OHP} (capacitance of inner Helmholtz plane) and C_{GC} (capacitance of diffuse layer) according to the Nernst equation and the flat band potential influences the C_s and C_{INS}, capacitance of semiconductor and insulating layer, respectively. The role of the width of the depletion layer (Eq. 2.13) is indicated in the C_S since:

$$C_s = \frac{\varepsilon_0 \varepsilon_r}{w} \qquad \text{Eq. 2.25}$$

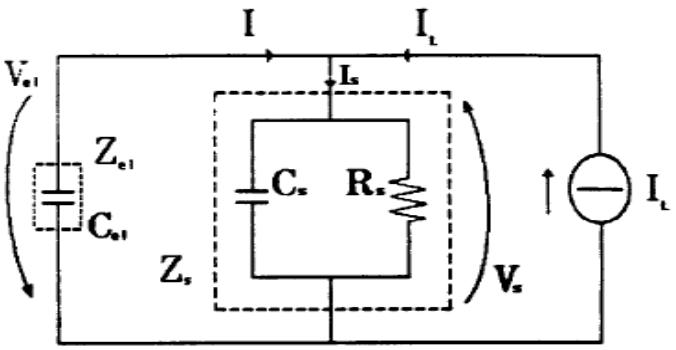

Figure 2.15. Simplified equivalent of the LAPS circuit used to deduce the measured photocurrent (I) [58].

Having explained this model, it should be noted that there are no unified formula correlating the photocurrent to the applied voltage that would explain all experimental data due to the complex nature of the interactions between the semiconductor, insulator and electrolyte in a LAPS system. Incorporating all the aspects of these interactions can model the responses seen in LAPS experiments.

The biggest advantage of LAPS over other sensors used in liquid sensing is the fact that since once illuminated parts of the sensing platform generate a response, the sensor is spatially sensitive. This brings forth the opportunity to image the changes in the system based on illumination.

2.2. Motivation and objectives

More than 1 billion people around the world, mostly in Asia, are without improved drinking water resources. In even more devastating numbers, almost 4000 children die from dirty water and related diseases each day [59]. A 4-fold increase in number of water related outbreaks in the course of 18 years (1991-2008) as mentioned in chapter 1 (section 1.1.2) and fatalities are

reported because of those outbreaks. All these statistics and unfortunate inequality in access to safe drinking water raises the global need for water monitoring, especially in areas where access to sophisticated facilities is scarce. Therefore, sensor devices should be developed to allow on-site monitoring of the safety of drinking water with shorter response times.

The primary aim of this research will be to develop a sensor capable of detecting harmful pathogens, particularly *E. coli*, in drinking water that can ultimately be used for on-site water monitoring. Measures will be taken to fabricate a sensitive and selective sensor based on LAPS to be functional at lab scale. The role of integrating hydrogel NFs into the system will be investigated in the sensitivity of the system. Functionalization of the sensing surface towards *E. coli* will be conducted to achieve selectivity towards the target bacteria and the ability of developing a system responsive to more than one type of pathogen will be examined. The versatility of the NF-LAPS system will be tested for media other than water. Eventually, a prototype of a NF-LAPS setup will be manufactured.

Chapter 3: The detection of *Escherichia coli (E. coli)* in water with NF-LAPS[1]

In this chapter, a simple, rapid and cost effective detection technique for *E. coli* using LAPS integrated with electrospun PVA/PAA hydrogel NFs as a sensing layer (NF-LAPS) is reported. Changes in pH of the media are detected as *E. coli* cells ferment sugar molecules and increase acidity of the surrounding. The high sensitivity is associated with the pH sensitive behavior of the NFs on the surface. Detection of acidic species released in cellular metabolism of pathogens in the presence of carbon source renders the sensing mechanism cheaper, less time consuming and more practical than the antibody-antigen interaction based approach. Selectivity towards *E. coli* for detection applications in drinking water is ensured by the incorporation of d-mannose, a sugar monomer, for specific binding [60]. Figure 3.1 summarizes the detection method in this chapter.

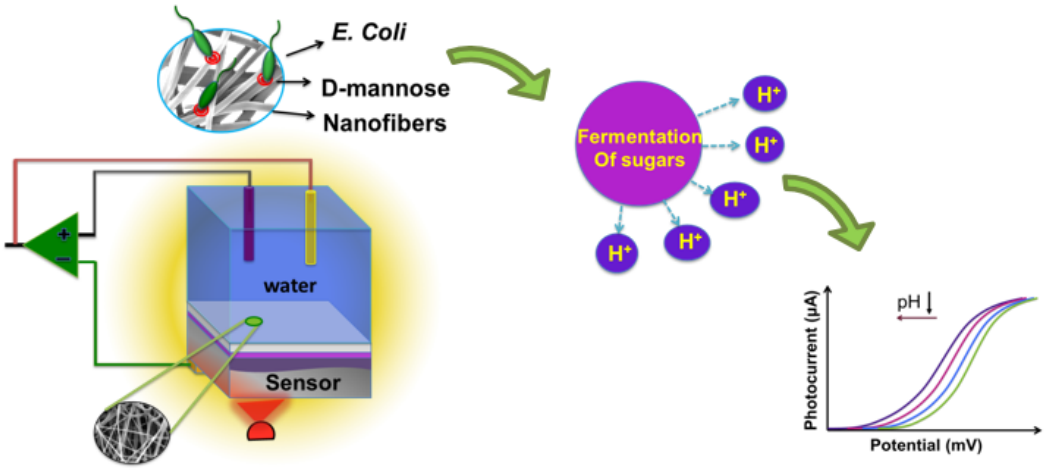

Figure 3.1. A summary of the detection method using the NF-LAPS. The pH sensitive hydrogel NFs act as a pH sensitive layer. The *E. coli* cells bind to the d-mannose on the surface of the NFs. The fermentation of glucose added to the system results in the drop in pH over time. The LAPS system with a p-type semiconductor WE responds to the changes in the pH. Photocurrent curves shift towards lower potential values as pH decreases.

[1] Parts of this chapter have been published in our work in Sensors and Actuators B: Chemical [60]

3.1. Objectives

In this study, the use of biocompatible electro-spun PVA/PAA hydrogel NFs fabricated by a simple electrospinning method, followed by annealing in a vacuum oven for crosslinking is reported. The annealed NFs act as the pH sensitive sensing layer in a LAPS system for *E. coli* detection after functionalization with d-mannose, for selective binding to *E. coli*. Divinyl sulfone is used as the cross linker between the NFs and d-mannose. Moreover, unlike conventional studies in which antibody-antigen interactions or Urease hydrolysis are set as the basis for *E. coli* detection, the fermentation of sugar molecules by *E. coli* as the sensing mechanism is selected. As previously studied by Werner et al. to determine the extracellular acidification of *E. coli* in a LAPS system, this phenomenon works when the bacteria produces acidic products such as acetate, lactate, succinate, etc. from fermenting sugar molecules [61].

The products decrease the pH of the environment, which can be detected by the NF-LAPS system. It should be noted that the use of antibody-antigen interactions makes biosensing more complex and detection less reliable. Byrne et al. have provided a thorough review of the principles of antibody based sensors and their problems [62]. The complexity may arise from additional steps such as verifying the specificity of the antibody, or complicated surface chemistry procedures for the conjugation of the molecules. Reproducibility is also an issue, when facing problems such as unsuccessful binding or loss of biological activity. The proposed sensor deals with no such issues. The NF layer is simply and inexpensively fabricated on the sensing chip through electrospinning. The surface functionalization is a one step process and the detection takes 60 min as opposed to days.

3.2. Experimental

This section focuses on the experimental processes and procedures to fabricate and characterize the NF-LAPS and steps used for *E. coli* detection.

3.2.1. NF-LAPS fabrication

All chemical reagents, except for divinyl sulfone, were purchased from Sigma Aldrich and used without further purification. Divinyl sulfone was provided by Alfa Aesar. Phosphate buffered saline (PBS) solution with an original pH of 7.4 was prepared by dissolving PBS in powder form into MilliQ water. Solutions for pH sensing were obtained by adding proper amounts of HCl or NaOH to the PBS solutions. To prepare the solution for the hydrogel sensing layer, the ratio of PVA/PAA was kept at 1/5 w/w with a sum of 3 g of material. The PAA (450,000 Da) was first dissolved in 50 ml of MilliQ water and left for stirring for 24 h. PVA (146,000–186,000 Da) was then gradually added and the solution was stirred for an additional 24 h to ensure a homogeneous mixture.

A homemade electrospinning setup was used for the fabrication of the hydrogel NFs. Clean p-type Si substrates with a thickness of 525 ± 25 μm and a natural SiO_2 layer were used as the collecting target. Electrospinning is a well-known method that uses high voltage to produce nanostructures, mainly NFs. High electric field is applied to a Newtonian fluid (mostly polymers) through a conductive needle. When the electric filed is high enough to overcome the viscoelastic properties of the electrospinning solution, a jet is formed. The jet travels towards a grounded target and the solvents evaporate under the electric field. Due to bending instability of the jet, the solution splits into smaller and smaller jets until nano-sized fibers reach the target.

We have extensively explored the optimization of the homemade setup in our previous work [63].

To prepare the NFs for the NF-LAPS chips, firstly an aqueous solution with pH=9 was electrosprayed followed by divinyl sulfone to assure the adhesion of the NF mat to the substrate. Immediately after, the PVA/PAA solution was electrospun. Electrospinning was done at a high voltage value of 20 kV, distance between the collector and syringe was 15 cm and a flow rate of 0.3 ml/h was maintained. The procedure was performed at room temperature. The as-spun samples were annealed under vacuum for 30 min at 145 °C to help the crosslinking and the evaporation of the residual solvents. Eutectic GaIn was used as the ohmic contact of the sensing chip.

Following the annealing step, the sensing chips were functionalized with d-mannose by immersing in an aqueous solution containing 0.1 mol d-mannose and 1 ml divinyl sulfone as the crosslinker. The solution pH was kept at 9 for activation of divinyl sulfone. The chips were kept in solution overnight for functionalization.

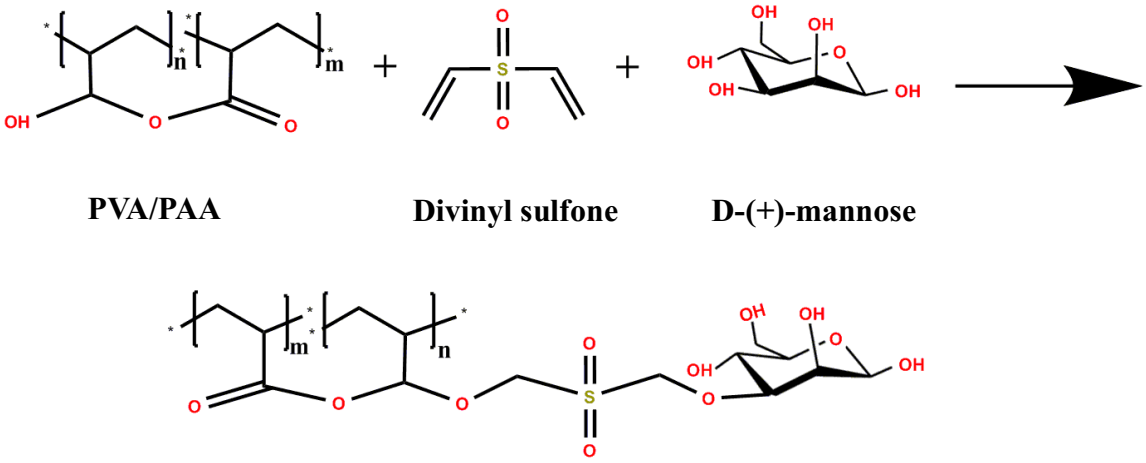

Figure 3.2. Schematic representation of the surface functionalization of d-mannose on the PVA/PAA hydrogel NFs. Divinyl sulfone is used as the cross linker between the polymer and the sugar.

Figure 3.2 represents the proposed mechanism of the surface functionalization with divinyl sulfone as the cross linking agent.

3.2.2. Characterization of NF-LAPS

In this section, the experiments to assess the PVA/PAA hydrogel NFs and the success of the surface functionalization are explained. In addition, the procedures to evaluate the performance of NF-LAPS towards changes in pH are described.

3.2.2.1. Characterization of PAA/PVA hydrogel NFs

As-pun and annealed hydrogel NFs were characterized before the sensing experiments to verify the nature and surface morphology. For the purpose of imaging, scanning electron microscopy (SEM VEGA-3, Tescan) was performed with an acceleration voltage of 20 kV. The average diameter of the NFs was determined by image processing available in the SEM software. Fourier transform infrared spectroscopy (FT-IR) study on the PVA/PAA hydrogel was carried out (Nexus 670 FT-IR) to examine the thermal crosslinking of the gel after annealing as well as the success of the surface functionalization step. Swelling studies were performed by first drying hydrogel NF mats at 60◦C for 1 h in vacuum. Dry samples were weighed, then immersed in aqueous solutions with various pH values and weighted at different time intervals. Swelling ratios were calculated in the following equation:

$$SR_w = \frac{W_w - W_d}{W_d} \qquad \text{Eq.3.1}$$

where SR_w is the swelling ratio in terms of weight, W_w is the weight of the wet samples at a given time and W_d is the initial weight of the dehydrated samples.

3.2.2.2. Evaluation of NF-LAPS in pH sensing

As seen in Figure 3.1, pH sensing measurements were conducted in a three-electrode system with the sensing chip acting as the WE. A pseudo Ag/AgCl electrode was used as the RE; Pt wire was chosen as the CE. Red LED light from the digital light processor, DLP® LightCrafter™ Evaluation Module (EVM) illuminated the backside of the sensing chip, modulated with a frequency of 12 kHz. A potentiostat (Gamry Reference 3000™) was used to measure the generated photocurrent. Direct current (DC) potential was applied to the system with a 2 mV increase step and scan rate of 40 mV/s. The aqueous solutions had pH values ranging from 4 to 9.

3.2.3. Cell cultures and sample preparations

E. coli ATCC 25922 (American type culture collection) from a −80 °C stock was cultured in Luria–Bertani (LB) broth overnight at 37 °C. The cultured *E. coli* was washed and suspended in 1xPBS for detection usage. Consequently, *E. coli* cells were stained by propidium iodide (PI) for fluorescence microscopy (red) characterization. *E. coli* cells were incubated with PI at 37 °C for 30 min before use. Colonies of *Pseudomonas fluorescens* (*P. fluorescens*) CHA0 (wild type) from −80 °C bacterial stock were streaked onto an LB agar plate. Then, the agar plate was incubated in incubator at 30 °C for 24 h. Next, a colony of *P. fluorescens* was transferred and inoculated into LB broth medium from the agar plate. Afterwards, the solution was kept in shaker incubator (New Brunswick Scientific Co., NJ) at 30 °C and 150 rpm for about 24 h. According to the required concentration for the experiment, we diluted the bacterial solution with LB broth medium. Furthermore, this bacterial strain expresses green fluorescent protein (GFP) constitutively, which gives us the opportunity to use fluorescent microscopy for their visualization.

3.2.4. Detection of *E. coli* in Phosphate Buffer Saline (PBS) solution

The method used here is similar to that explained for pH measurements in Section 3.2.2.1; however, *E. coli* cells were added to the buffers to achieve 400 µl samples with known concentrations in the range of 10^3–10^7 CFU/ml. 20 µl of 0.15 g/l (80 µM) glucose in MilliQ (MQ) water was added for the fermentation process.

NF-LAPS measurements started immediately after the addition of glucose (40 µl) and continued for 60 min. Control samples included a blank sample with glucose and a sample containing 10^7 CFU/ml of *P. fluorescens* bacterial cells. The rate of acidification for the *E. coli* samples was also calculated. Fluorescence microscopy was conducted on the NFs for bacteria samples of *E. coli* and P. fluorescens to examine the selectivity of the binding between d-mannose and E. coli. The NF mats were immersed in solutions containing the bacteria and imaged after washing with PBS using a fluorescence microscope (Nikon EclipseTi). *P. fluorescens* exhibits fluorescence without further processing; however, *E. coli* cells were stained as mentioned in Section 3.2.3.

3.2.5. Detection of *E. coli* in Real Water Samples (RWS)

To be able to detect the bacteria in real water samples (RWS), a portable device was fabricated based on NF-LAPS. A 3D printed sensor chamber is used to hold the NF-LAPS chips. A red LED with a wavelength of 635 nm and a frequency of 12 kHz illuminates the backside of the sensor. The WE is connected to a compact EMStat3 PalmSens potentiostat. DC voltage is applied through the potentiostat with 2 mV steps and a speed of 40 mV/s. The potentiostat communicates the I-V curve readouts to a generic tablet. EMStat3 uses the PStouch application for measurements and analysis.

RWS from the city of Edmonton were collected according to accepted protocols. Samples were stored immediately at 4 °C and used shortly after collection. The samples were filtered twice to remove large particles before sensing. 1 ml of filtered samples were filtered again to obtain 400 µl samples and tested for 1 h, with and without adding glucose. Experiments were also carried out after washing the surface to assure selective binding. Moreover, to ensure accurate detection outcome, 100 ml water samples were filtered through a 0.25 µl mesh filters. 400 µl samples achieved from filtering (from 1 ml samples) were tested in the NF-LAPS prototype. This step was conducted as a pre-enrichment approach.

3.3. Results

Here, the results obtained from the experiments explained in the previous section are reported (3.2). Characterization results are presented first, followed by results obtained from the NF-LAPS sensor unit in the lab as well as results from the portable NF-LAPS prototype unit.

3.3.1. Characterization of NF-LAPS

3.3.1.1. Characterization of PAA/PVA hydrogel NFs

SEM images of as-spun and annealed PVA/PAA mats clearly confirmed the formation of the NFs (figure 3.3). The as-spun sample displayed a uniform morphology in the form of cylindrical NFs with an average diameter of 340 ± 50 nm (figure 3.3(a)). Imaging the annealed NF mat showed that thermal processing has not compromised the integrity of the NFs and the morphology is preserved during heating. The average diameter of the annealed NFs is 350 ± 50 nm (figure 3.3(b)).

The results of FT-IR on the prepared NF samples after thermal processing confirmed the crosslinking of the polymers and the formation of PVA/PAA hydrogel. Figure 3.4(a) shows the FT-IR spectrum of the annealed NF sample as well as the surface functionalized NFs. In the annealed NFs, by adding PAA, the dissymmetry stretching vibration of C−O in PVA has moved from 1094 cm^{-1} to a higher wavenumber of 1098 cm^{-1}. The peak at 1413 cm^{-1} is associated with C−O as well, while the peak at 1269 cm^{-1} is linked to the stretching vibration of C−O, which has become broader in the hydrogel.

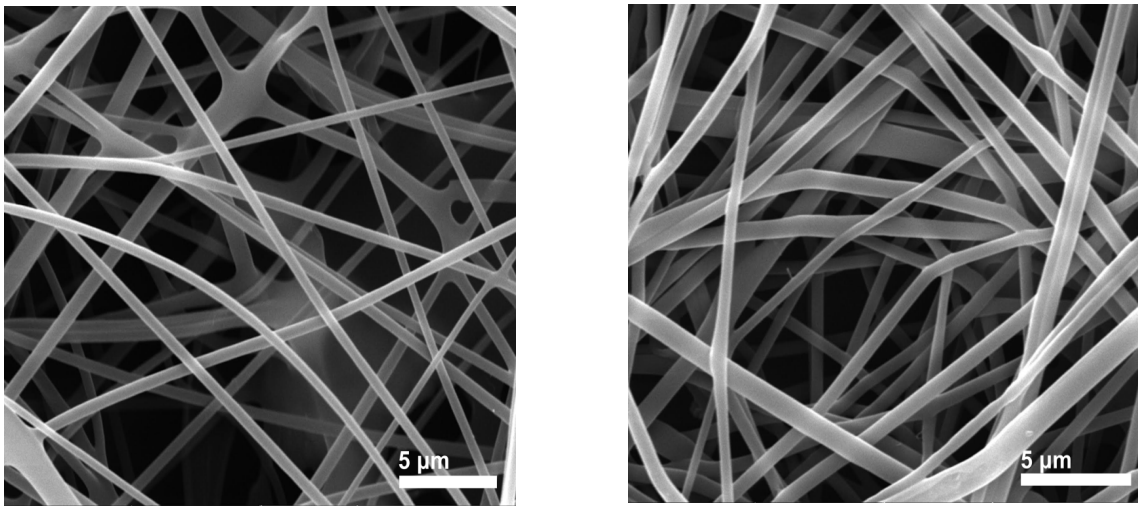

(a) (b)

Figure 3.3. SEM images of (a) as-spun PVA/PAA hydrogel NFs prior to annealing showing an average diameter of 340 ± 50 nm. (b) annealed PVA/PAA hydrogel NFs with an average diameter of 350 ± 50 nm; the formation of cylindrical NFs with uniform morphology is evident. The integrity of the NFs has been preserved during annealing (The scale bar is 5 µm).

The peak at 1245 cm^{-1} represents the vibration of $-CH_2$ connected to the carboxyl group. C–H stretching vibrations become evident in wavenumbers of 1449 cm^{-1} and 2921 cm^{-1}. The dissymmetry stretching vibration of C–O in the carboxyl group attributed to PAA has shifted to 1718 cm^{-1} in the PAA/PVA hydrogel. The absorbance peak at 3377 cm^{-1} is linked to the O–H stretching vibration of the hydrogel that has shifted from the 3288 cm^{-1} wavenumber for pure PVA. The findings are in agreement with the works of Manavi-Tehrani et al. [64] and Wang and colleagues [65].

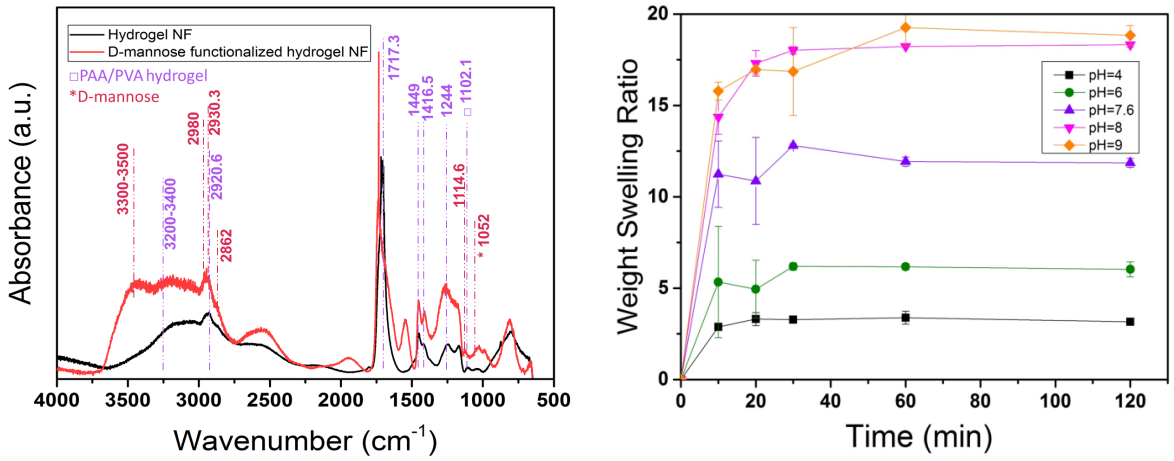

(a) (b)

Figure 3.4. (a) FT-IR absorbance spectra of the PVA/PAA hydrogel NFs annealed at 145 °C for 30 min and d-mannose functionalized NFs. The spectra confirm the crosslinking in the hydrogel by thermal processing and the successful incorporation of the sugar by surface functionalization. (b) Swelling behavior of the NFs in terms of weight in different pH conditions. The hydrogel NFs swell with time before reaching a final volume; moreover, the acidic hydrogel NFs used here swell more as pH increases.

The spectrum associated with the surface functionalized NFs shows the successful integration of d-mannose on the NFs (Figure 3.4(a)). The peaks in the wavelength region of 1050–1085 cm^{-1} and 1085–1150 cm^{-1} pertain to the various stretching vibrations of the aliphatic chain and the C–H stretching in d-mannose, respectively. The peaks arising in the region between 2800 and 3000 cm^{-1} indicate the $–CH_3$ and $–CH_2$ stretching vibrations.

Finally, the broad band at the 3300–3500 cm^{-1} range indicates the O–H stretching vibration. The spectral information is in accordance with what was reported by Witoonsaridsilp et al. [66]. Figure 3.4(b) shows the swelling behavior of the PVA/PAA hydrogel NF mats in different pH conditions as a function of time. It is clear that the swelling rate of the hydrogel increases as pH increases. This is advantageous for the LAPS system since the capacity of the sensing layer is changing with pH. Maximum swelling is observed at SR_w=18.83 for the sample in pH=9. In addition, all hydrogel NF samples show saturation in swelling under 1 h. The stability of the swelling over longer periods of time ensures the reliability of the sensing layer.

3.3.1.2. Evaluation of NF-LAPS in pH sensing

Figure 3.5(a) depicts the photocurrent (I_p) measured for the hydrogel NF-LAPS as a function of applied voltage for solutions with different pH values. The photocurrents are in the order of μA. There is an apparent shift in the LAPS response to higher applied voltages as pH increases.

Furthermore, the onset of the depletion state in the energy bands of the Si substrate, accompanied by the generation of the photocurrent, shifts towards higher potentials as pH increases.

This shift is proportional to the change in the width of the depletion layer in the semiconductor layer, as mentioned in Eq.2.16 (section 2.1.3 in chapter 2).A super- Nernstian response from the

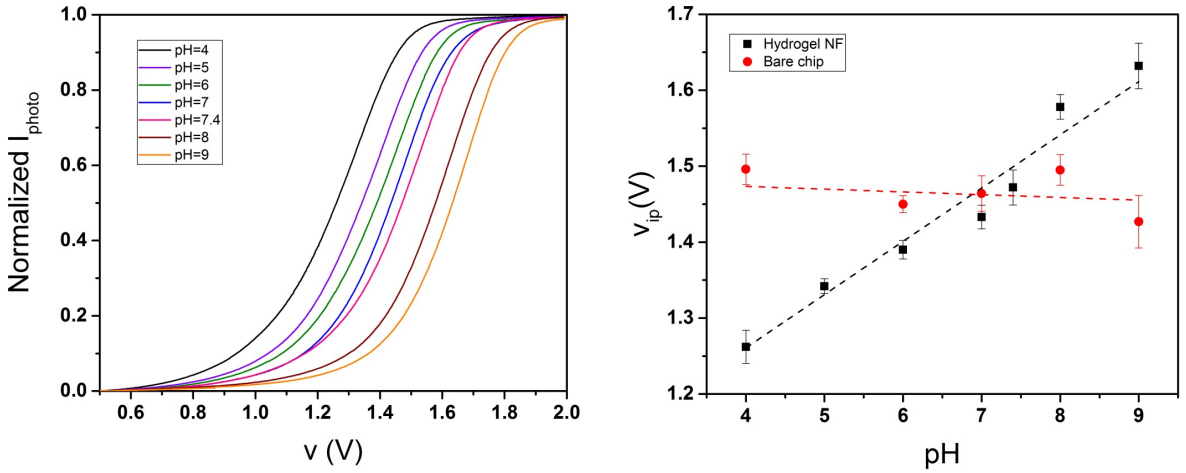

(a) (b)

Figure 3.5. (a) NF-LAPS generated photocurrent as a function of applied voltage for different pH values. Photocurrent curves shift to higher potentials as pH increases. (b) The inflection point potential of the NF-LAPS response, v_{ip}, from the photocurrent curves is illustrated at various pH values of the electrolyte. A super-Nernstian response is obtained in the system through a 74 mV/pH shift in v_{ip} (R^2=0.96). The response of the sensor chip without any NF layer is also demonstrated as a control experiment. There is virtually no change in v_{ip} when no sensitive layer is present with a slope of -0.003 mV/pH (R^2=0.93).

hydrogel NF-LAPS is seen in figure 3.5(b) where the inflection point, v_{ip}, of the photocurrent curves is shown as a function of solution pH. The slope of the linear fitting indicates an approximate 74 mV upward shift in the response of the system with a unit of change in the value of pH. The R^2 value of 0.96 indicates the linearity of the shift as pH increases, as predicted by the Nernst equation (Eq. 2.19). Compared to the conventional Si_3N_4, the response is much higher than the reported values of 55-58 mV/pH [67,68]. This shows that the hydrogel NF layer is more sensitive to pH changes in the electrolyte. The super-Nernstian response seen here is probably due to the fact that Nernst equation considers the activity of the sensing layer to be uniform throughout the bulk and neglects the activity of the surface. In this case the lower activity of the surface of the NFs causes the super-Nernstian response as mentioned earlier. The complex interactions near the surface of the NFs between the PVA/PAA hydrogel and the ions present can be a reason for such a response. Moreover, the physical swelling of the NFs contributes to the

overall signal from the NF-LAPS system. Figure 3.5(b) also demonstrates v_{ip} as a function of pH when no NF layer is present. The slope of -0.003 mV/pH clearly shows that the presence of an ion sensitive layer is required in order to get a valid LAPS response for different pH values.

3.3.2. Detection of *E. coli* in Phosphate Buffered Saline (PBS) solution

Figure 3.6(a) illustrates the change in pH over time for the various samples tested. The pH is determined through v_{ip} of the photocurrents for all the experiments. In the case of the *E. coli* samples, pH begins to decrease after the addition of glucose to the electrolyte as a result of the fermentation process. For the testing period of 60 min, pH shifts towards more acidic values and decreases further with higher concentrations of *E. coli*. The blank sample with only PBS and glucose shows little change in pH over the course of the experiment. The overall change with time in the blank sample can be attributed to the drift in the current of the system. Moreover, the selectivity of the NF-LAPS towards *E. coli* is confirmed when the solution with *P. fluorescens* is introduced into the system. *P. fluorescens* was chosen as it could represent interference in the detection of *E. coli* in drinking water. Most other sugar fermenting bacteria such as Salmonella

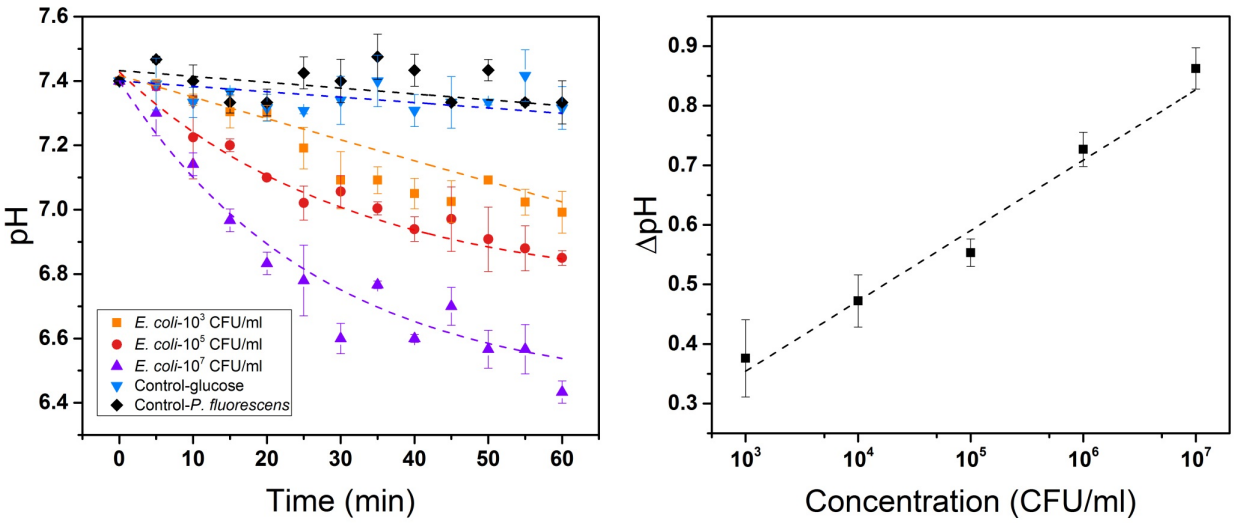

(a) (b)

Figure 3.6. (a) pH change as a function of time in the NF-LAPS system is shown at different concentrations of *E. coli*. *E. coli* ferment the glucose added to the electrolyte, generating acidic products yielding in a decrease in pH value. The pH decreases further with time at higher concentrations of the bacteria. Experiments with P. fluorescens as a negative control indicated minimal alteration in the pH value, suggesting that no fermentation occurs in the case of P. fluorescens. In addition, a control experiment where only glucose was used in the system exhibited little pH changes in comparison to the *E. coli*-containing samples. The overall change in the signal with time is merely due to the drift of the current. (b) Shows the response of the NF-LAPS after 60 min for different concentrations of E. coli in terms of change in pH (the concentration axis is in logarithmic scale). A linear sensor response is apparent with a slope of 0.118 pH per CFU/ml and an R^2= 0.997. The response indicates a theoretical limit of detection (LOD) of 20 CFU/ml for *E. coli* based on the slope of the line and signal to noise ratio (SNR).

are found in food, which is not the target of this study in water. As Figure 3.6(a) indicates, no evidence of fermentation is present, as the pH value remains virtually the same with respect to time. Once again, the small change in the value could most probably be caused by the sensor drift. Figure 3.6(b) shows the total pH change for all the different concentrations of *E. coli* in the NF-LAPS after 60 min (the concentration axis is in logarithmic scale). The response of the sensor is linear with aslope of 0.118 pH per CFU/ml and an R^2= 0.997. The response indicates a theoretical limit of detection (LOD) of 20 CFU/ml for *E. coli*, taking into account the noise level

of the system and a signal to noise ratio (SNR) of 3. The error bars appear as a result of multiple experiments with fresh sensing chips. Sensor chips are used once since E. coli is bound to the surface of the NFs after each experiment as biological residue. These biological residues prevent the use of the chips for repeated experiments without sterilization. As a result sensor chips are used only once.

In addition, we took fluorescence microscopic images to further investigate the selectivity of the functionalized NFs. The images comparing the binding of the E. coli and P. fluorescens tested, after washing with PBS, can be found in Figure 3.7(a) and (b), respectively. Figure 3.7(a) clearly shows the binding of *E. coli* cells, seen as the smaller glowing features, onto the surface of the NFs. The *P. fluorescens* cells however, were washed away with PBS and none were left bound to the surface (Figure 3.7(b)).

The images in the insets also show different magnifications of the two samples. The microscopic images con-firm the selectivity of the NF layer, with d-mannose on the surface, towards *E. coli*. The lack of binding to P. fluorescens is desirable, since *P. fluorescens* can interfere with the signal in real water samples.

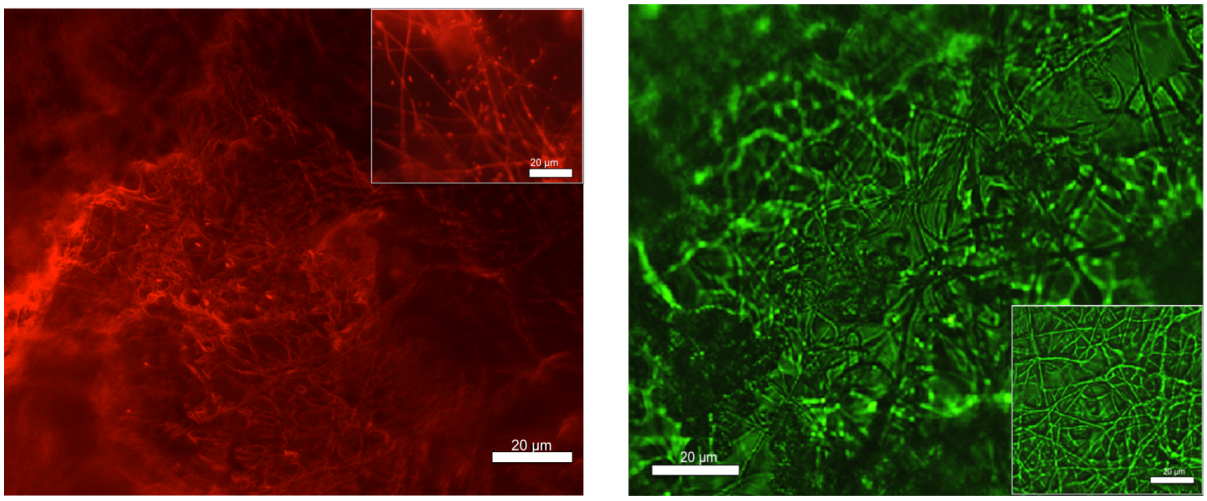

(a) (b)

Figure 3.7. Fluorescence microscopic images illustrate the selectivity of the NFs towards *E. coli*. (a) The d-mannose on the surface of the NFs has specific binding towards E. coli; after washing the NF mat, the *E. coli* are still bound to the NFs as seen by the smaller glowing features. *E. coli* has been stained by propidium iodide (PI) for red fluorescence.(b) *P. fluorescens* are not bound to the surface since there are no *P. fluorescens* cells present after washing. *P. fluorescens* strains imaged here have innate green fluorescence. The scale bars indicate 20 µm.

The rate of acidification for the *E. coli* samples based on the rate of fermentation in the NF-LAPS system was explored. Figure 3.8 demonstrates the acidification rate with respect to sample concentration in terms of H^+/s.cell (the concentration is in logarithmic scale). In theory, the rate of acidification should be the same per unit cell, for the same strain of cells; however, here we see different values as concentration changes. The disagreement with theory can probably be associated with the fact that the amount of sugar available to the *E. coli* cells remains constant even though the number of cells changes. In other words, in practice, lower concentrations of *E. coli* have more nutrients to ferment, leading to higher acidification rates at lower concentrations.

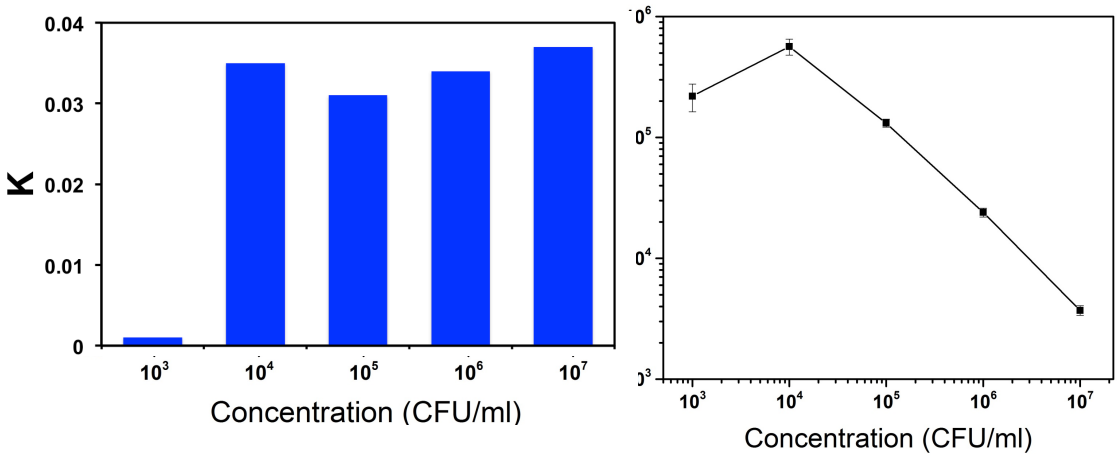

(a) (b)

Figure 3.8. (a) The rates of reaction k, for different concentrations of *E. coli.* These k values are used to determine the rate of acidification . (b) The rate of acidification for the *E. coli* cells is depicted for different concentrations, based on the NF-LAPS pH change in 60 min (the concentration is shown in logarithmic scale). Although in theory the rate should be identical per cell for all the concentrations, the value varies here; this is probably due to the fact that the amount of nutrients remains the same even though the number of cells increases. In other words, higher concentrations of *E. coli* have fewer nutrients available per cell; therefore, a decrease in the rate of acidification is seen for the same duration of experiments. This is more evident for concentrations higher than 10^4 CFU/ml.

This has also been explained in the work of Werner and colleagues [61]. The effect is more prominent for concentrations of 10^4 CFU/ml and the acidification rate might have slightly decreased for the lowest concentration due to saturation in the amount of nutrients.

3.3.3. NF-LAPS prototype

An image of the portable NF-LAPS is depicted in figure 3.9. The device consists of a 3D printed sensor chamber, a red LED with frequency driving unit, an EMStat3 PalmSens potentiostat and

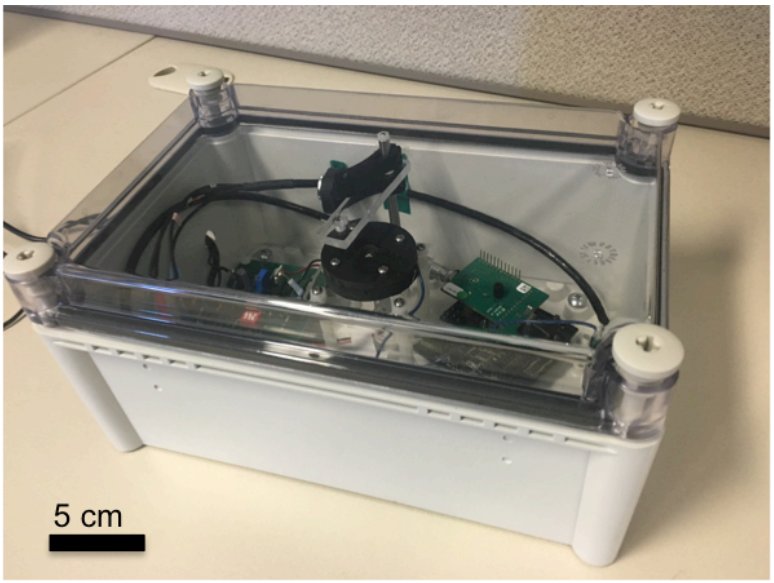

Figure 3.9. An image of the portable NF-LAPS prototype device that includes a sensor chamber, a red LED and a potentiostat. The unit communicates data to a generic handheld tablet, with the analysis android application, PStouch.

RE and CE. The sensor communicates the data to a generic handheld tablet through the android application PStouch. The entire prototype is approximately 30 cm long and 20 cm wide.

The device can be carried to any desired destination and has the potential to become even smaller. The sensor chips used in the prototype have demonstrated a lifetime of 6 months and are still in good condition. It is worth mentioning that sensor chips that have detected *E. coli* need immediate replacement since the binding to the surface is not reversible. The LED has so far been used for almost 400 h.

The portable NF-LAPS prototype has the capability to be used in the field without the need for highly trained personnel or sophisticated laboratory equipment. In the next section, the results obtained from experiments with the prototype will be presented.

3.3.4. Detection of *E. coli* in Real Water Samples (RWS)

RWS were tested in the portable NF-LAPS device without any signal hampering due to the more complex nature of the samples. Figure 3.10(a) illustrates the response of the prototype over time for RWS. Without adding any glucose, the samples show no pH change with time. However, when glucose is added, pH decreases with time, proving the presence of sugar fermenting entities in the media. To investigate the existence of *E. coli*, the sensor chamber is triple-washed so that there is no interference from possible sugar fermentation caused by other sources. The results in figure 3.10(a) from washed experiments show that there is still pH change, indicating that there is in-fact *E. coli* present in the RWS. The pH change is less compared to when there is no washing. This could be due to other interfering entities being washed away; moreover, not all *E. coli* cells might have bound to the surface before the washing step. It is worth noting that the collected RWS were not from drinking water sources. Plating samples in agar plate also showed the presence of colony forming units in RWS (figure 3.10(b)). Distinguishing the nature of the different colonies is not the focus of this work and can be pursued in the future.

The results presented here demonstrate the capability of the NF-LAPS prototype in handling real samples with no manipulation in the laboratory. This shows that with further testing in harsher conditions, the prototype can be used on-site for water monitoring.

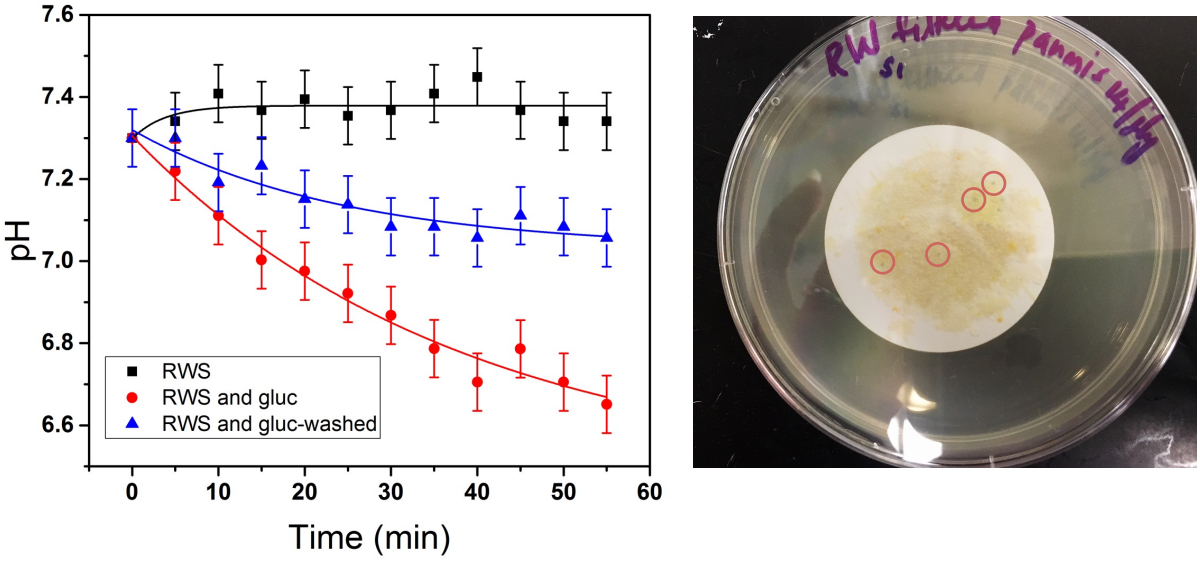

(a) (b)

Figure 3.10. (a) RWS tested with NF-LAPS. The results show that there are in fact *E. coli* cells present in RWS. The control experiment confirms the validity of the results. Washing the surface shows that binding is still occurring on the surface; however, other sugar fermenting entities do not remain in the system. pH change is not as significant after washing. This could also be due to some *E. coli* cells not binding prior to washing. (b) Colony forming units are evident after RWS were cultured on agar plate, some indicated by circles around the colonies.

In addition, to pre-enrich the water samples, 100 ml samples of RWS were filtered with 0.25 µl filter pads in order for *E .coli* not to pass. 400 µl of filtered samples were tested in the prototype. The surface of the sensor is washed to ensure selectivity. Figure 3.11 illustrates the fermentation of sugars by *E. coli* with time, by showing the drop in pH to more acidic values. The *E. coli* cells have remained on the sensor surface after washing by binding to the d-mannose on the surface of the NFs. Based on the obtained calibration curve, approximately 10^5 CFU/ml of *E. coli* is detected in RWS by the NF-LAPS prototype device.

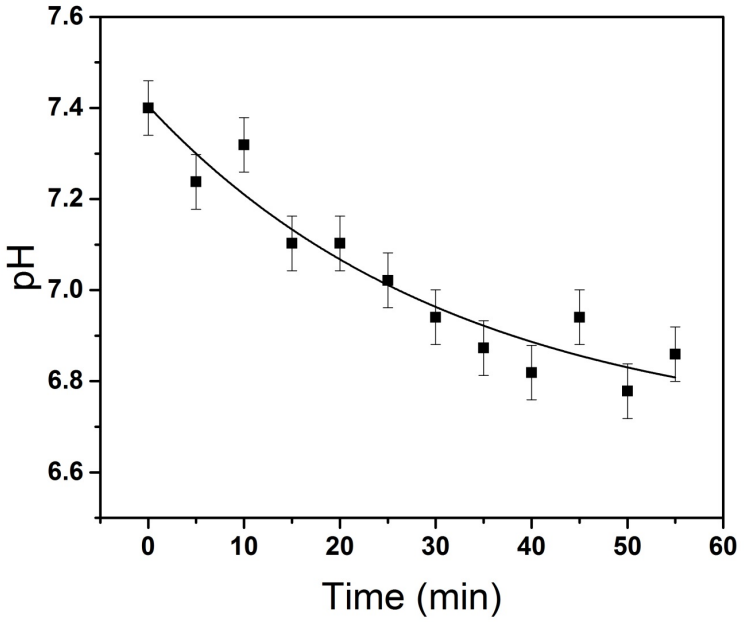

Figure 3.11. The response of the portable NF-LAPS to the pre-enriched RWS. Over time the pH decreases after glucose is added, indicating the presence of *E. coli* in water. Since the surface has been washed, *E. coli* is the only possible candidate to have fermented the glucose by binding to the d-mannose on the surface of the NFs. Approximately10^5 CFU/ml *E. coli* is detected, based on the calibration curve obtained for the NF-LAPS prototype.

It should be noted that more studies would be required in the future to compare different strains of *E. coli* to perhaps distinguish between pathogenic and non-pathogenic strains of the bacteria. This would help ensure the reliability of the prototype in field detection.

Chapter 4: The detection of *Escherichia coli (E. coli)* in orange juice with NF-LAPS[2]

In this chapter, the versatility of the NF-LAPS system is explored, particularly the prototype, by evaluating its performance towards the detection of *E. coli* in orange juice. Orange juice has a more complex composition with different molecules present in the medium. Moreover, orange juice is acidic by nature; therefore, the stability of the device is tested for use in acidic environments.

Various reports of outbreaks linked to *Escherichia coli (E. coli)* from different food products have recently surfaced following either minimally processed products or improper practices [69–71]. *E. coli* poses serious danger as one of the leading causes for foodborne diseases in developed countries [72]. Specific strains of *E. coli* can cause infections including diarrhea, bloody diarrhea, hemorrhagic colitis or even kidney failure due to the production of Shiga toxin [10]. Amongst all fruit juice, orange juice is the most widely consumed beverage and demands high priority in the case of pathogen contamination prevention. Interestingly, acidic fruit juices were not considered as hosts for bacterial life until recent years [73]. However, the occurrence of outbreaks has validated the possibility of pathogen growth in such beverages. Accordingly, the United States Food and Drug Administration (FDA) has imposed a number of treatments, inactivation processes and chemical sanitizations to ensure the safety of fruit juices available for consumption [74].

During the various stages of production processing and disinfection treatments, it is imperative that the quality of the beverage be monitored for possible infection with pathogens such as *E.*

[2] Parts of this chapter have been submitted to Sensors and Actuators B: Chemical for publication.

coli. Traditional detection techniques for *E. coli* consist of plating and colony counting methods, polymerase chain reaction (PCR) and enzyme-linked immunosorbent assay (ELISA). The merits of these methods cannot be denied as they are reliable, accurate and repeatable. On the other hand, these techniques require time consuming measurements, intensive training of highly qualified personnel and separate laboratory facilities.

For shorter detection times and approaches that can be deployed where food products are manufactured, packaged or distributed, methods are required that do not demand long processing times and are available on-site. Although SPR sensors have come close to producing bench-top devices for sensing purposes, electrochemical sensors offer a number of advantages. Firstly, the sensing mechanism is simpler in electrochemical sensors and their simplicity does not compromise the element of sensitivity. Secondly, electrochemical platforms have the capacity to be miniaturized and instrumentation is uncomplicated. Furthermore, electrochemical sensors have capability to be integrated with optical methods to form photoelectrochemical sensors for further sensitivity [75].

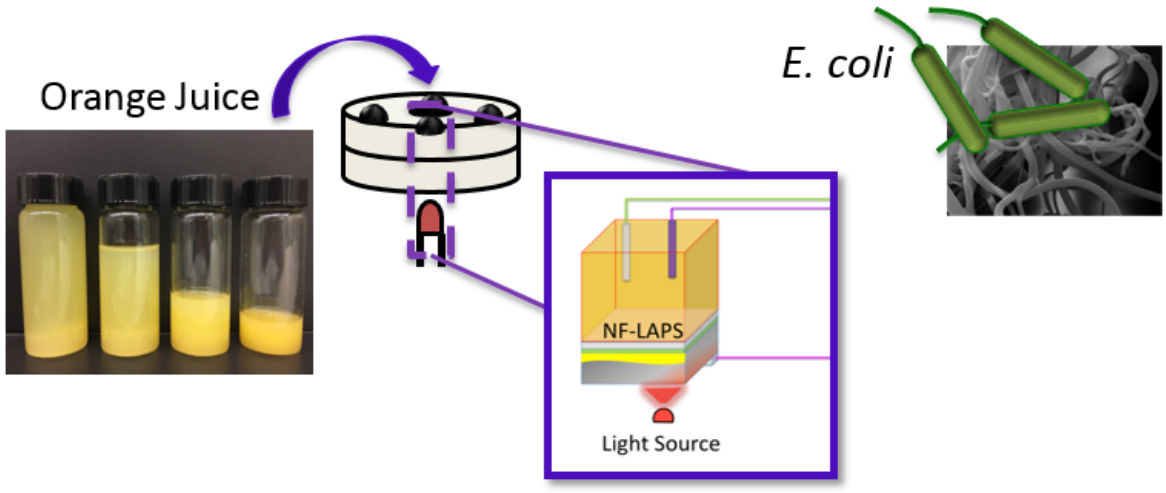

Figure 4.1. An illustration of the NF-LAPS sensor used for the detection of *E. coli* in orange juice. The bacterial cells bind to the surface of the NFs functionalized with d-mannose.

That is the case for the NF-LAPS system used for this work. Figure 4.1(a) shows a schematic representation of the NF-LAPS sensor chamber and its use for the detection of *E. coli* in orange juice.

4.1. Objectives

Here the application of a portable NF-LAPS system to selectively detect *E. coli* in orange juice in less than 1 h is demonstrated. We base our sensing mechanism on the metabolic activity of *E. coli* towards sugar molecules and the production of acidic products such as lactates and acetates. By functionalizing the surface of the NFs with d-mannose, we eliminate the need for antibody-antigen interactions as they are complex and reduce sensor reliability over time. In addition, to ensure the selectivity of the NF-LAPS towards *E. coli*, we used *Salmonella typhimurium (S. typhi)*. *S. typhi* is a sugar fermenting bacteria that can also be found in foods and fruit juices [76,77]. Selectivity against non-fermenting bacteria has already been established for this NF-LAPS in chapter 3. The sensitivity of the system is in no manner hindered by the presence of the opaque analyte with a variety of molecules in type and concentration. The illumination of light from the backside of the LAPS instead of the front ensures that the opaque samples do not interfere with the overall photocurrent. The simplicity of our photoelectrochemical sensor has the advantage of offering a compact and portable device for on-site sensing applications.

4.2. Experimental

All chemical reagents were purchased from Sigma Aldrich and used without further purification. Commercially pasteurized orange juice was purchased without additional preservatives and stored at 4 °C before use. A calibration curve for different pH values was obtained using phosphate buffer saline (PBS) solutions with HCl and NaOH for pH adjustments.

The sensor chips were fabricated according to methods explained earlier in chapter 3 including electrospun PAA/PVA pH sensitive hydrogel NFs. Si substrates of a p-type nature and a thickness of 525 ± 25 μm were used as the sensor chip substrates. The natural SiO_2 layer on the Si substrates was kept intact to ensure the insulation on the surface. After electrospinning, all sensor chips were annealed at 145 °C for 30 min before surface functionalization. The surface of the NF sensitive layer was functionalized with d-mannose according to previously established procedures (section 3.2.1). The experiments conducted for this work are explained further in this section.

4.2.1. Stability of NF-LAPS

Before *E. coli* detection measurements in orange juice, the stability of the NF-LAPS is tested for acidic environments by adding different concentrations of HCl to tap water. The concentrations tested are 1.5 mM, 3 mM and 4.5 mM To reach equilibrium with the swelling of the NF layer, 20 min experiments are performed for each concentration. The acidity is then reduced by diluting the solution in two consecutive steps. Repeatability is evaluated by alternately making tap water acidic with a 3 M HCl concentration and consequent dilution back to the original pH of 7.

4.2.2. Cell cultures and sample preparations

E. coli strain ATCC 25922 and *S. typhi* strain ATCC 19585 from a −80 °C stock were cultured in LB broth overnight at 37 °C. The cultured cells were washed and suspended in 1xPBS for detection usage. Bacterial cells were used from storage for sensing purposes after cooling to room temperature.

4.2.3. Detection of *E. coli* in orange juice

Orange juice is initially tested in the NF-LAPS with dilution factors of 1 (no dilution), 2, 4 and 6 to examine the response and stabilization time with respect to dilution. The bulk pH values are measured in all solutions for comparison. Orange juice is then spiked with *E. coli* to achieve concentrations in the range of 10^2 – 10^6 CFU/ml. For all the *E. coli* sensing measurements, glucose is added to the solution with a concentration of 80 μM to verify the fermentation of sugars and subsequent pH change. Glucose is added after 20 min to ensure the equilibrium of the solution in the NF-LAPS. Experiments each last 1 h after adding the sugar. A series of control experiments are performed to verify the response of the sensor. Orange juice without any *E. coli* is tested for the same duration. Glucose alone is added to orange juice in a separate set of experiments, each running for 1 h. *E. coli* is added to orange juice as well and tested for 1 h (after signal stabilization) without added glucose to compare with conditions where glucose is added manually. All experiments are performed at room temperature and repeated at least three times. Each test uses 400 μl of solution. New chips are used every run to ensure reproducibility.

To examine the selectivity of the sensor towards *E. coli*, *S. typhi* is used as a sugar fermenting bacteria. Orange juice is spiked with 10^6 CFU/ml *S. typhi* and tested with and without washing the surface of the sensor chip. The same is done for *E. coli* for comparison.

4.3. Results

4.3.1. Stability of NF-LAPS

Figure 4.2 depicts the photocurrent curves obtained with the NF-LAPS device for 10^6 CFU/ml *E. coli* in orange juice for the first 25 min after glucose is added. At lower applied potentials (0.6-0.8 V) where the sensor is in a state of accumulation, there is no photocurrent. As the potential increases, a photocurrent is produced which indicates a state of depletion for the sensor. After initial stabilization, I-V curves shift to the left towards lower applied potentials. This means that the pH of the medium is lowering as a result of the metabolic activity of *E. coli.* The inflection point of the curves is used to determine the pH value, based on previously obtained calibration curves.

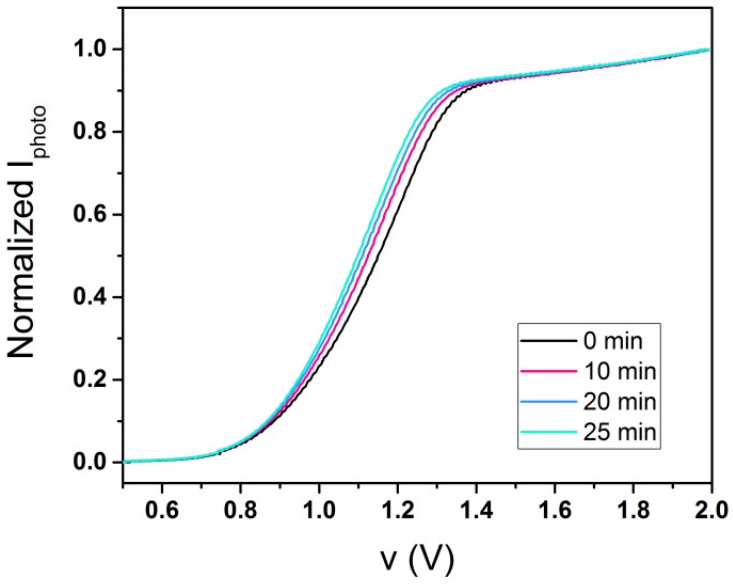

Figure 4.2. Photocurrent curves with respect to applied voltage for the NF-LAPS. Orange juice spiked with 10^6 CFU/ml *E. coli* after signal stabilization, when glucose is added. The photocurrent signal shifts towards lower applied voltage values, indicating a more acidic environment as a result of sugar fermentation by the bacterial cells.

Response of the portable NF-LAPS system to stepwise increase in the acidity of the medium is illustrated in figure 4.3(a). When tap water (pH 7) was added to the sensor, an initial jump was observed. This initial jump during the first few minutes in the calculated pH is due to the fact that the hydrogel NFs begin swelling from a dry state. After 5 min, the pH values vary minimally and eventually reach pH 7, 15 min later. As tap water is acidified in three steps with 1.5 mM HCl, the measured pH decreases in the NF-LAPS as well. The deswelling of the NFs from higher pH values dictates the obtained signal with time. Following the last acidification step, the solution is diluted in two 20 min steps with the same volume as the added acid. The pH would not go back to 7, as changes in pH are not linear with respect to volume. The adaptation of the NFs to sudden pH changes might seem lengthy. In the case of extracellular acidification however, changes in acidity are gradual. Figure 4.3(b) represents the repeatability of the NF-LAPS response towards acidification. Each cycle consists of acidification with 3 mM HCl solution and subsequent dilution back to the original pH value of 7. The repeatability of the NF-LAPS is evident which is one of the important features of biosensors. The error bars indicate multiple experiments.

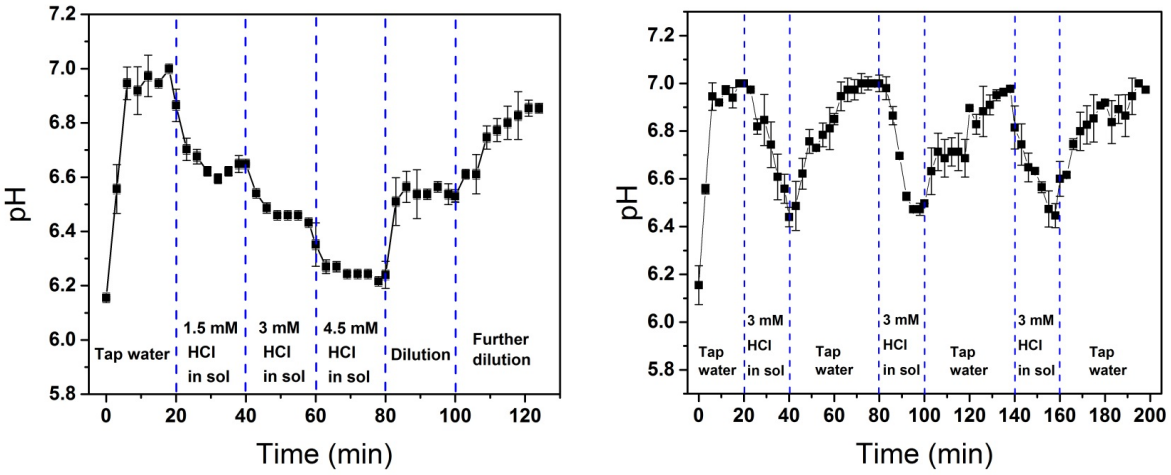

(a) (b)

Figure 4.3. Response of the portable NF-LAPS system to (a) stepwise increase in the acidity of the medium. The initial shift in the calculated pH value is a direct effect of the swelling of the NF layer from a dry state into a wet state. Therefore, accurate values are taken after the initial stabilization. By increasing the acidity of the medium, measured pH values begin to decrease accordingly. Consequent dilution causes the increase in pH. Stabilization occurs after 20 min in each stage. The response time is a result of the swelling and deswelling of the pH sensitive NF layer; (b) cyclic acidification and dilution. Notice that each cycle is 60 min long. The 20 min stabilization time is designated to the acidification and the 40 min is appointed to the dilution required to increase the pH back to its initial value. All pH values are calculated based on the pH calibration curve of the NF-LAPS obtained previously with a sensitivity of 74 mV/pH [60].

4.3.2. Detection of *E. coli* in orange juice

We firstly examined the effect of dilution in orange juice with dilution factors of 1 (no dilution), 2, 4 and 6. Figure 4.4(a) and 4.4(b) show that the signal in NF-LAPS is most stable where there is no dilution. A dilution factor of 2 is also suitable, however a drop in the voltage after 10 min indicates that swelling of the NFs might have been countered by a separation in the phases of the solution, as shown in figure 4.4(d). It is worth mentioning that the calculated pH for diluted samples during the initial stages (shown in figure 4.4(b)) does not represent the actual pH of the

orange juice with time; it merely points to effects of dilution that delays equilibrium in the system. For instance, without dilution, the calculated pH is very close to the true pH value of orange juice (3.9). In addition, the variation in measured pH is small over time. When orange juice is diluted 6 times with tap water (with pH 7) it is expected that the pH is higher than 3.9. However, the initial measured values (first 5 min) are far from the real pH values, a possibly because the water is trying to separate from the cloudy portion of the orange juice. Despite the longer equilibrium times for diluted samples, the final pH at 20 min is accurate for all samples. Figure 4.4(c) also confirms the increase in pH for diluted solutions. Orange juice with no dilution has a pH of 3.9 and a pH of 4.5 with a dilution factor of 6. Figure 4.4(d) verifies the assumption that there is a separation of phases in diluted samples. All of these findings demonstrate that there is no need to dilute orange juice for the sensing measurements. In addition, according to Anvarian et al., clarification and loss of the cloudy component of orange juice affects the viability of microorganisms in the beverage and may in fact increase it [78]. Therefore, it is vital that we do not tamper with the physiological interactions of *E. coli* and orange juice.

We then investigated the ability of NF-LAPS to detect *E. coli* by spiking orange juice, without dilution, with 10^6 CFU/ml of the bacteria. As seen in figure 4.5, the pH value of the environment decreases when *E. coli* is added. Due to the variety of sugars already present in orange juice, fermentation occurs even when no glucose is added to the *E. coli* spiked orange juice.

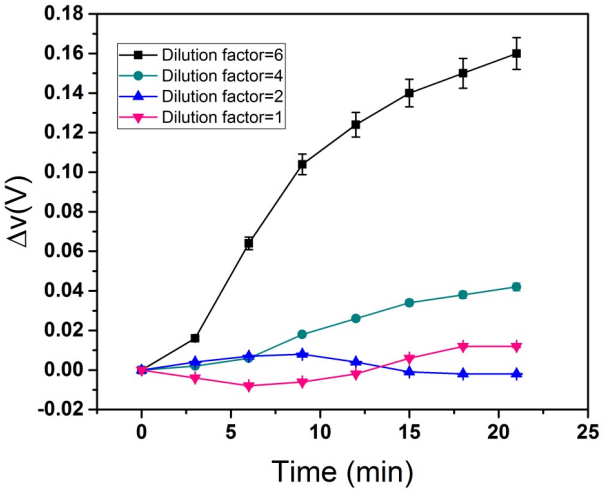

(a)

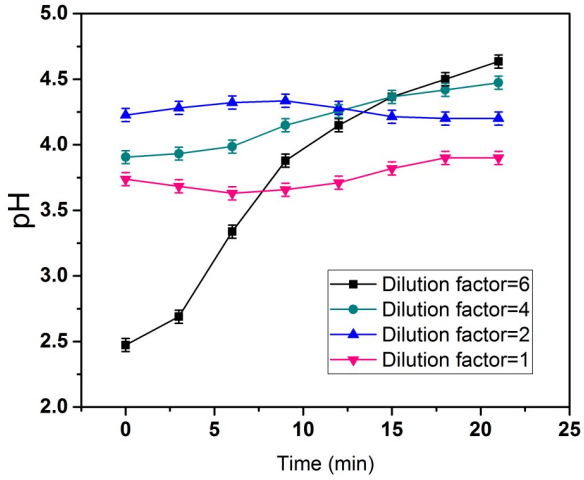

(b)

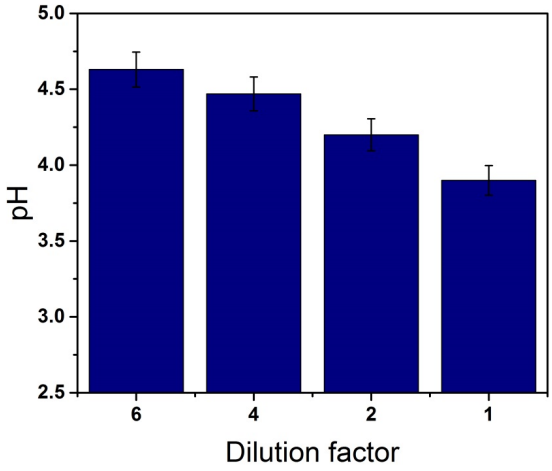

(c)

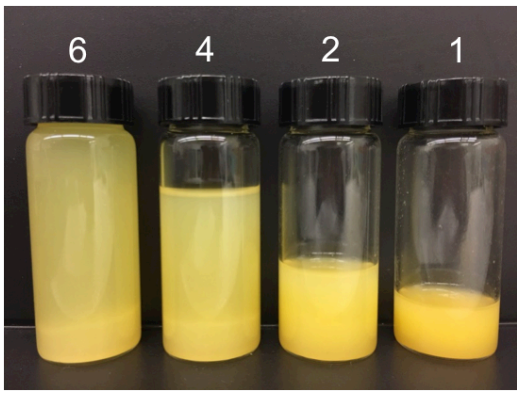

(d)

Figure 4.4. The effect of orange juice dilution on the NF-LAPS signal. (a) Shift in the inflection point of the I-V curves with time for different dilution factors in orange juice. The signal is most stable where there is no dilution. This means that although the stabilization time is equal for all dilution factors, the overall signal is more consistent when the orange juice is directly used without further dilution. The difference is probably due to the separation of the added water from the orange juice, with time. (b) The calculated pH values with time for the various dilution factors. The graph shows the change in the pH values as a result of dilution. Performing measurements on orange juice samples without any dilution has not hindered the sensitivity of the NF-LAPS towards pH. (c) The final pH of the solutions after stabilization of the NF-LAPS. The measurements match bulk pH readings. (d) Image of the orange juice with different dilutions, depicting the separation between the phases. Solutions without dilution proved to be the most reliable samples.

However, for real life applications, pH might have already been lowered if the beverage is contaminated beforehand with *E. coli*. For this reason, it is paramount to add glucose to the mixture to see if further fermentation takes place. It is evident that adding glucose has led to further extracellular acidification (figure 4.5). Bear in mind that when there is no *E. coli* in the solution, pH does not show significant change with time as evident in figure 4.5.

To determine the sensitivity of the NF-LAPS device, we tested a range of different *E. coli* concentrations from 10^6 CFU/ml down to 10^2 CFU/ml. It is worth reiterating that the NF-LAPS is stable when glucose is added. Figure 4.6(a) displays the pH change with time for *E. coli* in orange juice after adding glucose. The higher the concentration of the bacterial cells, the lower the final pH of the media.

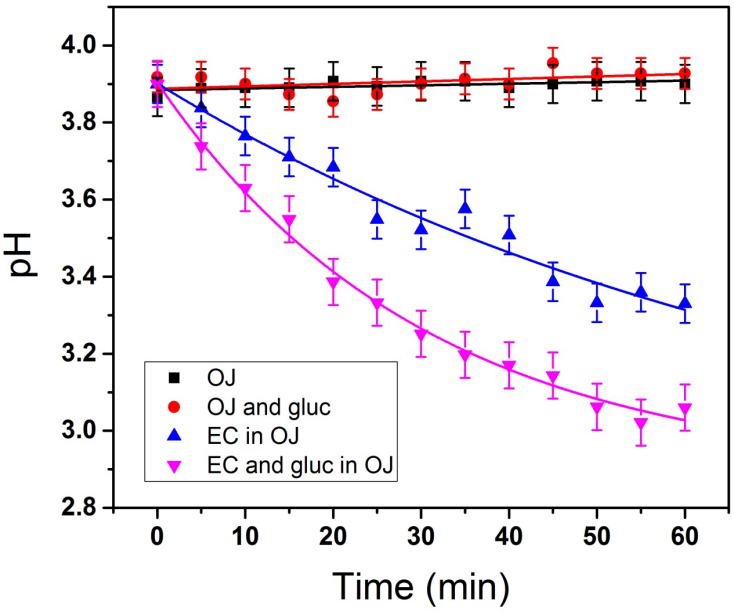

Figure 4.5. Drop in the pH of the media, as a result of the fermentation of sugars in orange juice spiked with *E. coli*. There is no noticeable change in pH with time in the absence of *E. coli*, with or without any sugar added. When *E. coli* is introduced, the media becomes more acidic due to the presence of a variety of sugars in orange juice; however, pH decreases even further when glucose is added to the medium. This is crucial for the sensor to function for real samples tested, since the initial pH may already be lowered by the presence of bacteria.

The sensitivity line is achieved for the device based on the overall change in the orange juice pH as a result of the metabolic activity of *E. coli*. The slope of the sensitivity line depicted in figure 4.6(b) is 0.149 per CFU/ml of *E. coli* in orange juice and R^2=0.989. The slight deviation from the fitted line is associated with the lower concentrations of 10^2 CFU/ml and 10^3 CFU/ml, probably because the amount of sugar available for the bacteria has been saturated. Hence the change in pH is somewhat close despite the fewer number of *E. coli* cells present. The measured limit of detection (LOD) of the NF-LAPS is shown to be 10^2 CFU/ml; considering the signal to noise ratio of the device, the theoretical LOD of the system is calculated to be 20 CFU/ml.

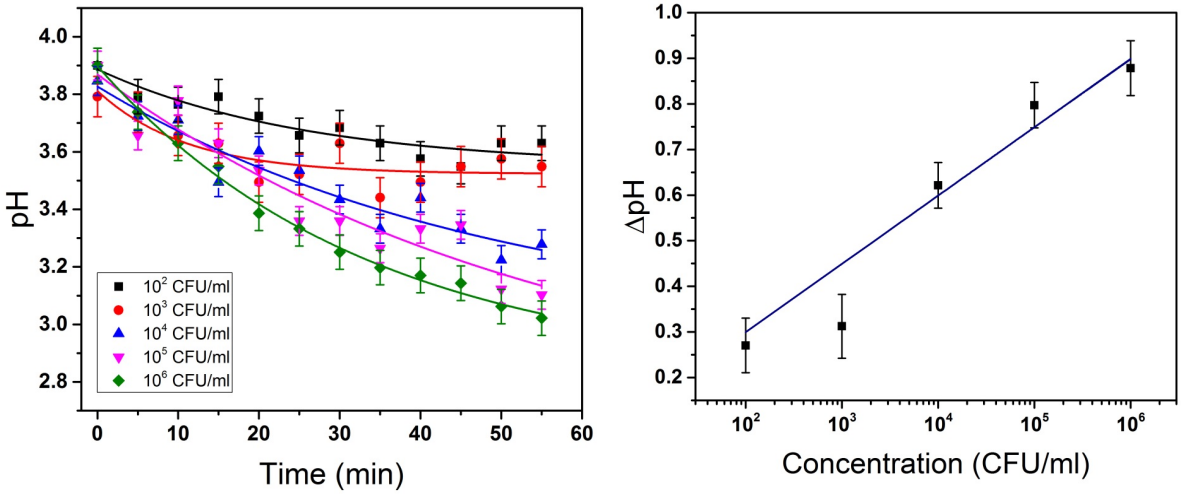

(a) (b)

Figure 4.6. (a) Change in pH with time for various concentrations of *E. coli* in orange juice after adding sugar. Higher concentrations of the bacteria produce more acidic products, thus reducing the pH further. (b) Sensitivity of the NF-LAPS towards different concentrations of *E. coli* in orange juice. The fitted sensitivity line has a slope of 0.149 per CFU/ml of *E. coli* in orange juice and R^2=0.989. Lower *E. coli* concentrations of 10^2 and 10^3 CFU/ml do not show significant difference in the final pH probably due to the fact that sugar may be excess in the media and saturated the fermentation process.

Figure 4.7(a) illustrates the selective detection of *E. coli* in orange juice when compared to the sugar fermenting *S. typhi*. When the surface of the sensor is unwashed, *S. typhi* causes pH change in orange juice but acidification occurs more rapidly for *E. coli* at the same concentration as *S. typhi* (10^6 CFU/ml) for the same duration. More importantly, when the surface of the NF-LAPS sensor chip is triple washed before adding glucose, only in the case of *E. coli* does the pH value drop with time. This shows that the *E. coli* has preferred affinity towards the d-mannose on the

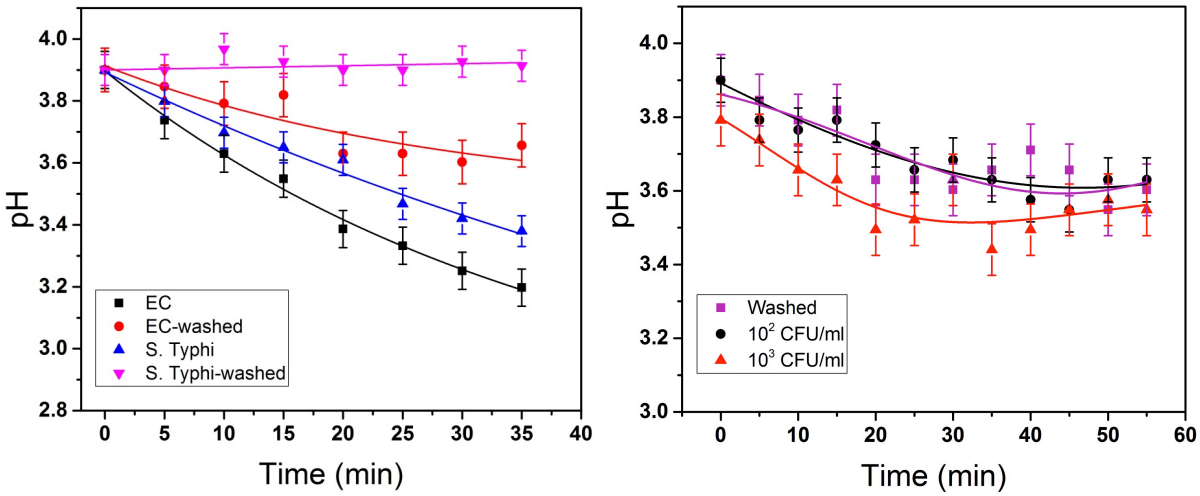

(a) (b)

Figure 4.7. The selectivity of the portable NF-LAPS is tested against *S. typhi*. (a) demonstrates the pH of the orange juice with time after the introduction of 10^6 CFU/ml of either *E. coli* or *S. typhi*. When the surface is not washed prior to testing, pH changes for both types of bacteria. However, pH becomes more acidic for *E. coli* in the same time period. The acidification in the presence of *S. typhi* is due to the sugar fermenting nature of the bacteria. In order to ensure that only *E. coli* cells bind to the surface of the functionalized NFs, the surface of the sensor is washed before glucose is introduced. Due to the higher affinity of *E. coli* to the d-mannose on the surface of the NFs, there is no change in pH seen for *S. typhi* after the surface is washed. On the other hand, the pH value decreases with time for *E. coli* even after the surface is washed. (b) The response of the NF-LAPS for *E. coli* after washing is compared to the known concentrations tested. The comparison and the sensitivity line of the NF-LAPS show that approximately 10^2 CFU/ml of *E. coli* remains on the surface after washing.

surface of the NFs as opposed to *S. typhi*. The difference in specifity of various bacterial genera towards mannose is also established by Firon et al. According to that report, the term mannose-specific bacteria is too general and the combining lectin sites in *E. coli* differ significantly from those of *S. typhi.* In fact all the *S. typhi* strains tested showed a different mannose binding behavior compared to *E. coli* [79].

To further investigate the effect of washing, pH measurements are further continued for *E. coli*. According to the sensitivity line obtained, approximately 10^2 CFU/ml of *E. coli* is estimated to have remained on the surface after washing. This is also verified in fig. 6(b) when results are compared to acidification curves for known concentrations of *E. coli*, shown in figure 4.6(a). The selectivity aspect of the NF-LAPS is an undeniable requirement when testing real samples, especially when a portable device is used. This eliminates the need for additional testing at sophisticated laboratory facilities. Therefore, the portable NF-LAPS device would be a great candidate for monitoring the safety of orange juice for consumers at different stages of production and distribution.

Overall, the NF-LAPS offers many advantages compared to other sensing techniques, as mentioned earlier in chapter 1. It offers high sensitivity, especially due to the incorporation of the NFs. It is more versatile than methods such as SPR or QCMs since it is easier to use, uses inexpensive sensor chips and can be used for a variety of target media. Pathogen detection with the NF-LAPS is desirable especially since the portable NF-LAPS can be used for on-site monitoring. The mass production of electrospun NFs is still a challenge for large scale applications in any system; however, for the NF-LAPS system a small volume of NFs are required and can be accommodated in daily production.

Chapter 5: Alternate application of the NF-LAPS: Study of cancer cell metabolism [3]

The NF-LAPS system is quite versatile for the detection of pH changes, especially due to the metabolic activity of different living cells. The LAPS platform can be of great assistance in biomedical applications, especially point of care applications due to its merits, as discussed before. The sensitivity that NF-LAPS offers alongside its capability to be used outside the laboratory environment through portable devices gives it a great advantage over other techniques. Therefore, we propose the use of this versatile method in biomedical applications. To this end, we have studied cancer cell metabolism with the NF-LAPS.

The metabolic properties of cancer cells differ significantly from that observed with normal cells [80,81]. Emerging evidence shows that tumor cells utilize glucose and glutamine metabolic processes to meet the increased energy demands needed for proliferation, invasion, angiogenesis and metastasis. The production of energy in cancer cells relies abnormally on anerobic glycolysis, a phenomenon known as the Warburg effect [82]. The Warburg effect is defined by an increased level of glucose utilization via glycolysis. In addition, such highly proliferating cells depend on other atypical metabolic properties like increased fatty acid synthesis and elevated rates of glutamine breakdown [82]. Previous studies have shown that many characteristics of cancer cells, such as dysregulated Warburg-like glucose metabolism, fatty acid synthesis, and glutaminolysis, are linked to therapeutic resistance in cancer treatment [83–85]. Furthermore, a number of recent reports have shown that targeting cellular metabolism may improve the

[3] Parts of this chapter have been published in our work in ACS Sensors, doi: 10.1021/acssensors.6b00632.

response to cancer therapeutics [86]; thus, combining chemotherapeutics with metabolic enzyme inhibitors may represent a promising strategy to overcome drug resistance in cancer therapy.

5.1. Objectives

In this study, we report on measuring cancer cell acidification and monitor their response to therapeutics over a period of 2 h using NF-LAPS in an effort to contribute to the current understanding of cancer metabolism (Figure 5.1).

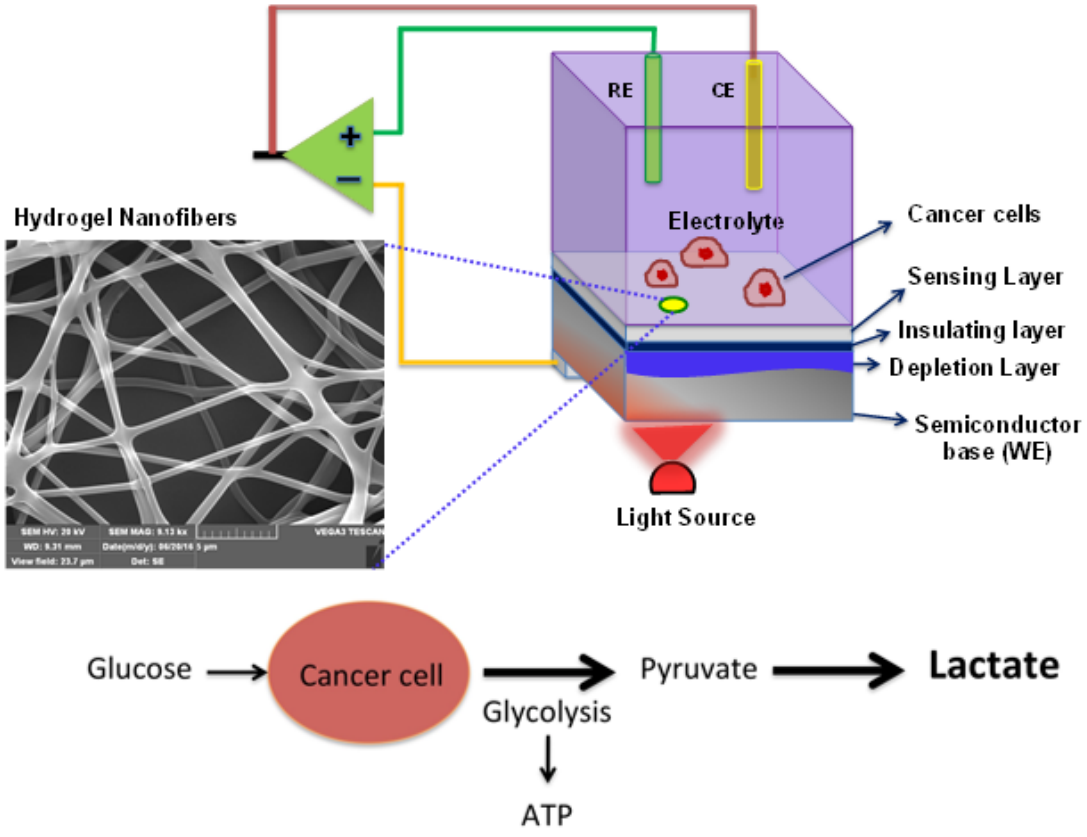

Figure 5.1. The NF-LAPS setup used for the detection of cancer cell metabolism. The pH sensitive hydrogel was fabricated on top of p-type Si substrate to work as a pH sensitive layer (Scanning electron microscopy shows the NF layer).

We also explored the implications of the metabolic enzyme inhibitors in extracellular acidification, tumor proliferation and potential shifts of tumor metabolism in combination with cancer chemotherapy.

5.2. Experimental

Fabrication of the sensor chips with pH sensitive PVA/PAA hydrogel NFs was carried out using a homemade electrospinning setup as described previously in section 3.2.1. However, there was no additional functionalization on the surface. The formation of NFs was confirmed by SEM imagine (figure 5.1). The cell culture steps and cell metabolism experiments are further explained in this section.

5.2.1. Cell cultures and sample preparations

The human breast cancer cells line MDA-MB-231 (ATCC, Manassas, VA) was used in this study. The cells were cultured in Dulbecco's modified eagle medium (DMEM) containing 10% fetal bovine serum (FBS), 100 IU/ml penicillin and 100 IU/ml streptomycin. The human mammary epithelial cell line MCF10A was also used as a representative of normal breast cells. MCF10A was cultured in a minimal essential growth medium (MEGM, Lonza, Cedarlane) supplemented with the same additives as above. Resistant type cancer cell line (MDA-MB-435-MDR) was used as a resistive breast cancer cell in order to investigate the chemoresistance and response to antibiotics in the presence of metabolic enzyme inhibitors. All cells were cultivated at 37 °C in a 5% CO_2–95% O_2 incubator, and the growth media were replaced every 48 h.

5.2.2. Cell experiments

As indicated earlier, we base our study on measurements of the extracellular pH fluctuation (acidification) initiated by cancer cells in the surrounding media. Due to the high sensitivity of

the hydrogel NFs, very small changes (down to ~0.02 pH) can be easily detected. In the first set of the experiments, we calibrated the physiochemical properties of the NF-LAPS with DMEM medium at pH 7.3 using a linear sweep voltammetry (LSV) method. In 400 μL culture medium and at a concentration of 1×10^5 cell/ml, harvested cancer cell lines MDA-MB231 or the noncancerous cell line MCF10A, were transferred to the sensor chamber and kept under standard culture conditions for growth. The NF-LAPS readings were recorded directly after addition of the culture and continued for approximately 90 minutes. Control samples included a blank medium free of cell lines and a culture medium containing noncancerous cell lines were used as a reference for comparisons. The rate of acidification was simply calculated from the photocurrent measurements. The acidification of cells was also recorded in the absence of glucose and in the presence of different glucose levels (2 mM to 10 mM). In addition, to measure sensitivity of the sensor, we recorded the acidification in the presence of different concentrations of cancer cells ($10^3 – 10^6$ cells/ml).

5.2.3. Metabolic inhibitor experiments

For monitoring drug resistance, we used the multidrug resistant cell line (MDA-MB-435-MDR) and monitored the acidification as above, for approximately 90 min in the presence of doxorubicin (solely at 1 μM) or doxorubicin with metabolic enzyme inhibitors, 2-deoxyglucose (2-DG), or Oxamate at 1 μM. Statistically, experiments were performed using multiple chips and run under same conditions to ensure the reproducibility of the experiments. All measurements were carried out under STP settings. All measurements were averaged and each experiment was performed at least three times. Data are presented as mean standard deviation (± SD) throughout the chapter. Multiple chips were used to exhibit the reproducibility of the results. Unlike bacteria

tests, sensor chips can be reused for cell acidification studies, since there is no irreversible binding to the surface of the NFs.

5.3. Results

The SEM images confirmed the formation of PAA/PVA hydrogel NFs with an average diameter of 330 ±50 nm (figure 5.1). The results of the experiments are presented in this section.

5.3.1. Cell experiments

We initially tested the performance of the sensor using the culture medium (DMEM at pH 7.3). This was also used as a standard reference for our next experiments (Figure 5.2(a)). From the statistics, the fluctuation in the potential of the NF-LAPS was found to be stable. For subsequent stability testing, we monitored the extracellular acidification (the pH sensitivity of the NF-LAPS) by scanning the photocurrent versus voltage characteristic curves under a series of pH conditions. The fluctuation in the pH can be easily generated from the photocurrent change with respect to applied voltage and the pH sensitivity of the calibrated curve. First, results obtained with low glucose level (DMEM low glucose) media spiked with breast cancer cell lines (MDA MB231), or normal breast cell line (MCF10A) at a concentration of 10^5 cells/ml, showed no significant changes in the pH over 80 min of monitoring (Figure 5.2(b) and 5.2(c)). However, when a glucose supplement (10 mM) was added to the media, a decrease in the pH in the cancer cells spiked medium compared to the normal cells contains medium as well as to the reference control (medium free of cells) was observed.

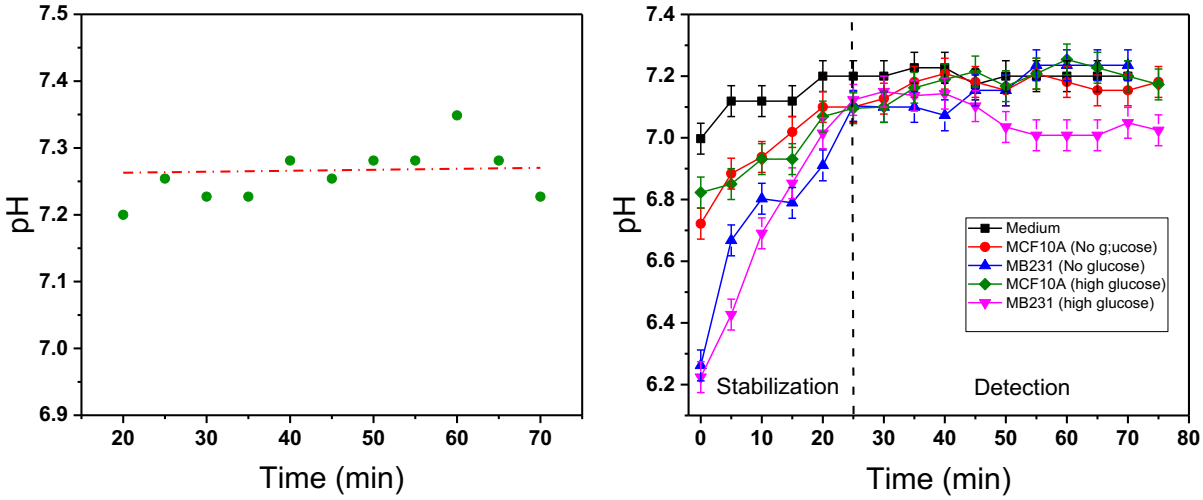

(a) (b)

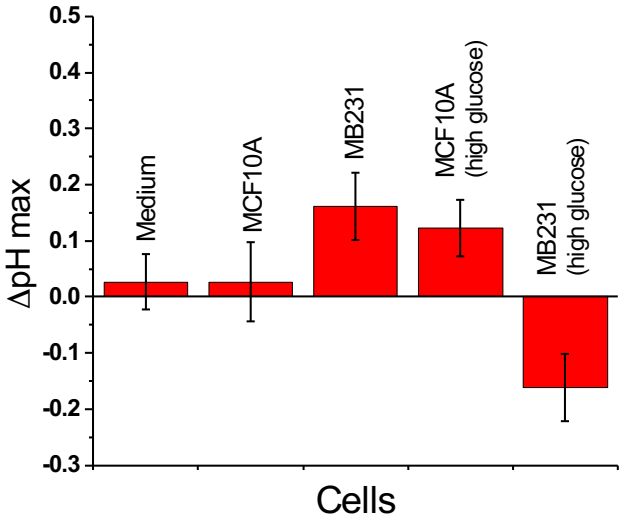

(c)

Figure 5.2. Metabolic monitoring of cancer cells by detecting the extracellular acidification on microenvironment. (a) standard pH fluctuation monitored in a culture medium (DMEM pH 7.3) to show stability of the NF-LAPS sensor performance, (b) the detection of extracellular acidification (pH change) of breast cancer cells (MDA MB231) in microenvironment (400 μl sample) at low and high level of glucose moieties. As indicated the level of acidification was compared to normal cell lines (MCF10A) in same environment with low and high levels of glucose; (c) shows the ΔpH max where statistics of different pH changes were recorded and averaged values (mean ±SD) were presented from three replicates carried at same environment and different time periods.

Furthermore, experiments where different concentrations of glucose were added showed different degree of shifts towards acidic pH. Higher acidity (lower pH) was observed when a higher concentration of glucose was injected (~0.4 pH change, which is equivalent to about 29 mV, Figure 5.3(a)). The noise level of NF-LAPS was less than 5 nA, and the sensitivity of detection was approximately 74mV/pH. The sensitivity for different concentrations of the cancer cells (with glucose added) shows a slop of 0.092 cell/ml and pH resolution reaches 0.02 pH. This was very consistence with previous results of sensor performance tests. We strongly believe that pH begins to decrease after the addition of glucose as a result of the accelerated glucose fermentation process by cancer cells. In contrast, there was no evidence of fermentation in the media spiked with normal cell lines, as the pH value remained virtually the same with respect to the tested time period. These results are also in agreement with previous reports and confirm further that the energy production in cancer cells is abnormally reliant on aerobic glycolysis [87,88].

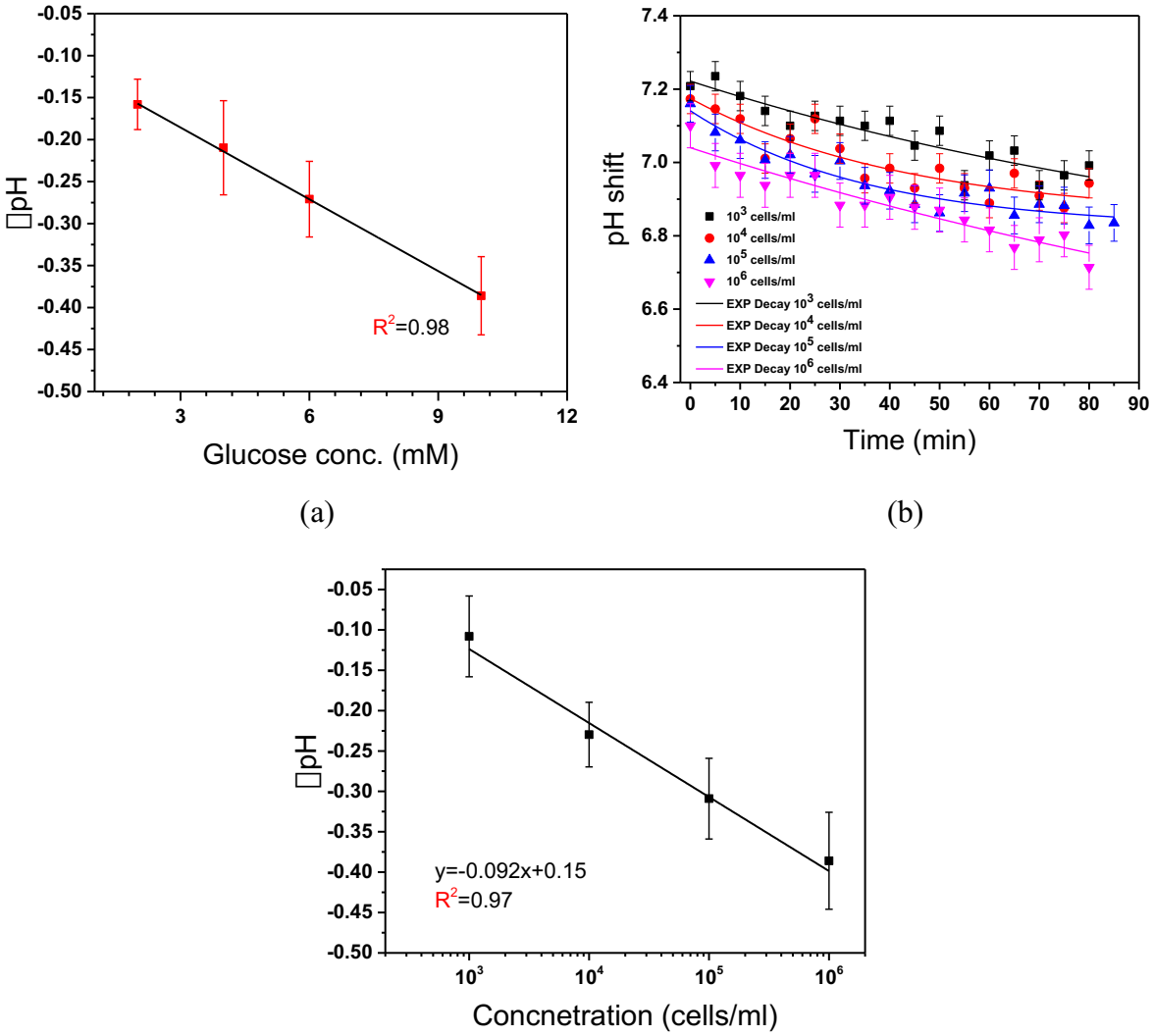

Figure 5.3. NF-LAPS sensitivity and concentration dependence measurements. (a) pH shift as a function of time at different glucose levels and fixed concentration of cancer cells (10^6 cells/ml). Figure b represents the correlation between pH and the different concentrations of cancer cell after stabilization in the sensor chamber. The results suggest that the extracellular pH decreases with time at higher number of cancer cells; i. e., the values of pH scales inversely with number of cancer cells in the sample. The fitted curves indicate the exponential decay in pH change. c, pH shift in the NF-LAPS after exposure to serial concentrations of cancer cells shows the sensitivity of the sensor. The corresponding fit is a linear function and error bars represent standard deviations (n=3). All data represents an average of 3 replicates and error bars correspond to standard deviations.

To identify sensitivity of the NF-LAPS in detecting extracellular acidification, a series of experiments where glucose rich media having various concentrations of cancer cells (MDA MB231) were tested for pH change over 90 min period. Figure 5.3(b) shows the pH change over time for different concentrations of cancer cells after stabilization in the sensor chamber. The fitted lines represent exponential decay of the pH change with time. While in Figure 5.3(c), we observe the sensitivity line for the NF-LAPS with respect to concentration of the cancer cells in the presence of glucose. It is clear that the pH scales inversely with the number of cancer cells in the sample. The detection limit, the minimum number of cells which can show detectable change in the pH, was found to be 10^3 cell/ml for an SNR of 3. The rate of acidification of cancer cells, based on the serial concentrations of cancer cells used, was found to vary with the NF-LAPS sensor. Although acidification rate per cell should be the same for all the concentrations, the observed values vary, most probably due to the increase in the number of cells while the amount of nutrients remains the same. Therefore, at lower concentrations, the cancer cells may have more glucose to ferment leading to higher rates of acidification. On the contrary, at higher concentration of cancer cells, cells may get less glucose to ferment causing lower level of acidification.

5.3.2. Metabolic inhibitor experiments

Next, we determined the extracellular acidification of the multidrug resistance cancer cell line (MDA-MB-435-MDR), alone and in presence of doxorubicin in glucose rich media. Monitoring the extracellular acidification over a period of ~ 90 min showed a dramatic drop in the pH due to glucose fermentation by cancer cells (Figure 5.4(a) and 5.4(b)). This is in contrast with what is observed with the non-resistant cancer cells (MDA MB231) when they were treated with the same anticancer drug (Figure 4(b)). The results suggest that resistant cancer cells are not provoked by the introduction of doxorubicin. Instead, their metabolic processes remained active by generating lactic acid metabolite. Further, to estimate the effect of metabolic enzyme inhibitors on cancer cells, culture media with or without doxorubicin was treated with metabolic enzyme inhibitors (2-deoxyglucose (2-DG), or Oxamate) at 1 μM. The results are illustrated in Figure 5.4(a) and 5.4(b), which show the effect of metabolic enzyme inhibitors on cancer cells acidification over a 90 min period. While in the presence of enzyme inhibitors alone, the pH has dropped to acidic, a notable increase in the pH (lower acidification) was observed when doxorubicin was co-administered with the enzyme inhibitors. It appears that both enzyme inhibitors have generated a synergistic mechanism by which the anticancer activity of doxorubicin was improved. The 2-DG is a glucose analog metabolic inhibitor that acts with other chemo and radiotherapy to enhance the anticancer activity. The analog is phosphorylated by hexokinase enzyme to generate a stable 2-DG-phosphate. This stable product accumulates in the cells, inhibits further metabolic process, decrease glycolysis and cause ATP depletion [86,89]. The Oxamate, on the other hand, is a pyruvate analog that blocks glycolysis by blocking the conversion of pyruvate to lactate [86,90]. Results illustrate that the combination of doxorubicin with 2-DG or Oxamate generate a glycolysis inhibitory effect on doxorubicin resistant cells,

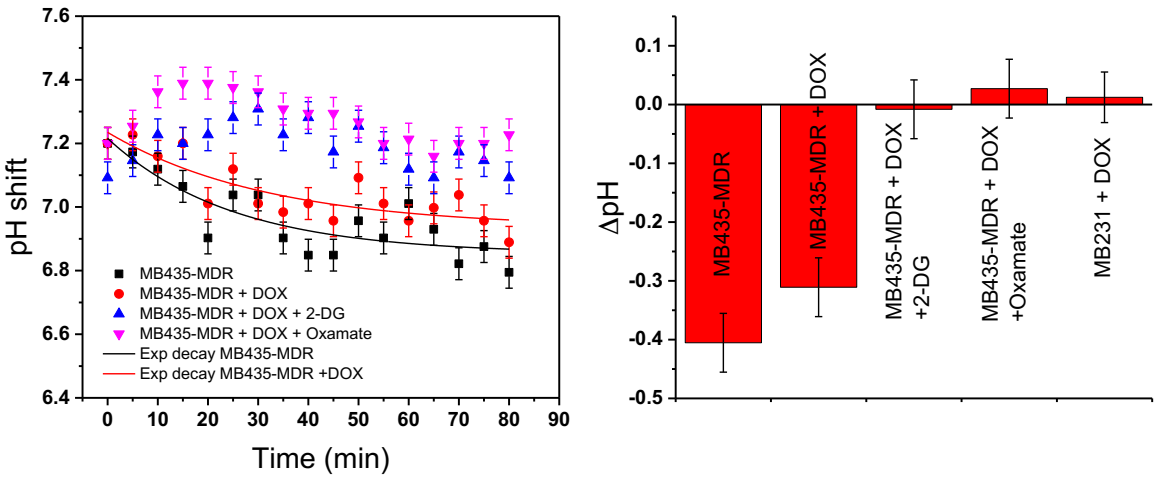

(a) (b)

Figure 5.4. Experiments display response of the NF-LAPS system to the resistant cancer cell line (MDA MB435-MDR) in the presence of Doxorubicin (DOX) alone or in combination with metabolic enzyme inhibitors, 2-DG or Oxamate. (a) the detection of extracellular acidification due to the resistant cancer cells (MDA MB435-MDR), alone, in the presence of DOX, or in the presence of DOX with metabolic enzyme inhibitors, as specified. As results indicated, a significant drop in pH was observed when cancer cells incubated alone or with DOX; however, lower acidification rate (no change in pH) was observed when DOX was co-administered with the enzyme inhibitors, 2-DG or the Oxamate. Results suggest a synergistic effect of the combined therapy on cancer metabolism. An exponential decay trend is observed for the changes in pH in the absence of inhibitors, seen as the fitted curves; (b) represents statistical data derived from three replicate studies conducted at the same environment. Averaged values are presented with error bars indicating standard deviations.

which may have led to a synergistic anticancer effect on cancer. Although a number of key studies remain to be explored, we anticipate these finding will contribute well to the current understanding of cancer metabolism and its related mechanism of drug resistance. The device will be very useful for a variety of applications including drug discovery and testing pharmaceutical ingredients.

Chapter 6: Conclusions and Future Directions[4]

The biocompatible PAA/PVA hydrogel NF network is successfully fabricated by means of electrospinning and subsequent thermal crosslinking and functionalized for biosensing applications. The swelling study of the NFs demonstrates the increase in swelling ratio with pH, as expected. The hydrogel NF-LAPS system shows quality performance in the detection of changes in pH with an overall super-Nernstian response. The biosensor shows a linear response with regards to the concentration of the bacteria. The NF-LAPS is successful in the detection of *E. coli* with a theoretical LOD of 20 CFU/ml based on the sensitivity line and SNR. The selectivity of the system towards *E. coli* is confirmed compared to the control sample containing *P. fluorescens.* The mannose specific lectins of *E. coli* render the d-mannose functionalized NFs a highly suitable platform for biosensing. Furthermore, the acidification rate of the *E. coli* (calculated as H^+/s.cell) is different for the various concentrations tested.

Testing the prototype device in detecting *E. coli* in RWS has also been successful. This means that the device shows great promise in the field of water monitoring, particularly where biosensors are needed, especially since it has been made into a portable device and can be used for on-site detection of *E. coli* in water.

In addition, we have investigated the detection of *E. coli* in orange juice using the portable NF-LAPS device, where we have a more complex media. The sensing measurements have determined the presence of *E. coli* in less than 1 h. We have also demonstrated the sensitivity of the device towards *E. coli* down to 10^2 CFU/ml and calculated a theoretical LOD of 20 CFU/ml. Furthermore, we have established that there is no need for dilution of orange juice prior to

[4] Parts of this chapter have been published in Sensors and Actuators B: Chemical. Some parts have been submitted to ACS sensors.

testing, which is an advantage for the sensor device. Repeatability of the experiments has indicated the reliability of the sensor for applications outside the laboratory. We have shown the selectivity of the NF-LAPS by ruling out interference from the sugar fermenting *S. typhi*. Even without washing the surface of the sensor, we can differentiate the acidification of *E. coli* and *S. typhi;* however, for accurate results we would recommend washing prior to testing. Lastly, we believe the portable NF-LAPS has great potential to be used as a monitoring device to ensure the safety of orange juice as well as other fruit juices at various stages of production, distribution and consumption.

Tom demonstrate the versatility of the NF-LAPS system, we have successfully monitored the metabolic activities of cancer cells in a non-invasive fashion. Results show the ability of the NF-LAPS to monitor the extracellular acidity of cancer cells in real time. It was used to investigate chemoresistance of cancer cells and shows the effects of metabolic enzyme inhibitors on the anticancer activity when they are combined with chemotherapeutics. Reducing drug resistance would have a significant boon for cancer patients. Designing simple tools to detect drug resistance and measuring drug efficacy would have significant impact on the current use of drugs, efficacy monitoring and in future for new drug discovery. More studies will be needed to explore the possibilities of using the NF-LAPS to further study cancer cell behavior.

The next step in this endeavor would be to examine the portable NF-LAPS prototype device in a variety of environmental conditions and using various real samples. This would help to get the device closer for use in remote areas where there is need for on-site monitoring of water without long wait times and sophisticated laboratory equipment. Moreover, efforts will be made to fully automate the process for data acquisition and analysis using the potentiostat system incorporated in the prototype.

In addition, there is a need for further study regarding the different strains of *E. coli* to differentiate between pathogenic and non-pathogenic strains for applications in onsite detection. More field tests will help to validate the success of the NF-LAPS prototype.

References

[1] United States Geologicla Survey, The World's Water, (2016). http://water.usgs.gov/edu/earthwherewater.html (accessed September 27, 2016).

[2] U. Nations, Integrated Monitoring Guide for SDG 6 Targets and global indicators Cross-cutting and fragmented at the core of sustainnable development, 2016. http://www.unwater.org/fileadmin/user_upload/unwater_new/docs/SDG 6 targets and global indicators_2016-07-19.pdf.

[3] World Health Organization, Guidelines for drinking-water quality, 2011. doi:10.1016/S1462-0758(00)00006-6.

[4] United Nations, The United Nations World Water Development Report 2015, 2015. https://www.unesco-ihe.org/sites/default/files/wwdr_2015.pdf.

[5] V. Alavian, H. Maher Qaddumi, D. Eric, S.M. Diez, A. Danilenko, G. Puz, B.C. Bates, Z.W. Kundzewicz, S. Wu, J.P. (Eds) Palutikof, A. Matavel, S. Bila, L.D. Brekke, J.E. Kiang, J.R. Olsen, R.S. Pulwarty, D.A. Raff, D.P. Turnipseed, R.S. Webb, K.D. White, K.C. Urama, N. Ozor, Climate change and water resources management : A federal perspective, DC World Bank. 2 (2009) 1–29.

[6] Environmental Protection Agency, Types of drinking water contaminants, (2016). https://www.epa.gov/ccl/types-drinking-water-contaminants (accessed September 29, 2016).

[7] N. Bolong, A.F. Ismail, M.R. Salim, T. Matsuura, A review of the effects of emerging contaminants in wastewater and options for their removal, Desalination. 238 (2009) 229–

246. doi:10.1016/j.desal.2008.03.020.

[8] E. Torres, G. Gonzalez-M, B. Klotz, D. Rodrigo, Effects of high hydrostatic pressure and temperature increase on Escherichia coli spp. and pectin methyl esterase inactivation in orange juice, Food Sci. Technol. Int. (2015) 1–8. doi:10.1177/1082013215582107.

[9] A. Bashir, N. Boisen, F. Scheutz, E.E. Paxinos, R. Sebra, C. Chin, D. Iliopoulos, A. Klammer, P. Peluso, L. Lee, A.O. Kislyuk, J. Bullard, A. Kasarskis, S. Wang, J. Eid, D. Rank, J.C. Redman, S.R. Steyert, J. Frimodt-møller, C. Struve, A.M. Petersen, K.A. Krogfelt, J.P. Nataro, E.E. Schadt, M.K. Waldor, Origins of the E. coli strain causing an outbreak of hemolytic-uremic syndrome in Germany, N. Engl. J. Med. 365 (2012) 709–717.

[10] K. Jiang, H. Etayash, S. Azmi, S. Naicker, M. Hassanpourfard, P.M. Shaibani, G. Thakur, K. Kaur, T. Thundat, Rapid label-free detection of E. coli using antimicrobial peptide assisted impedance spectroscopy, Anal. Methods. (2015). doi:10.1039/C5AY01917F.

[11] M.J. Figueras, J.J. Borrego, New perspectives in monitoring drinking water microbial quality., Int. J. Environ. Res. Public Health. 7 (2010) 4179–202. doi:10.3390/ijerph7124179.

[12] CBC news, Inside Walkerton: Canada's worst-ever E. coli contamination, (2010). http://www.cbc.ca/news/canada/inside-walkerton-canada-s-worst-ever-e-coli-contamination-1.887200 (accessed September 30, 2016).

[13] A. Mascarenhas, Drinking water quality surveillance: Samples from Pune villages found "contaminated," Pune, 2016. http://indianexpress.com/article/india/india-news-india/pune-

water-quality-control-2777382/.

[14] K. Yang, J. LeJeune, D. Alsdorf, B. Lu, C.K. Shum, S. Liang, Global distribution of outbreaks of water-associated infectious diseases., PLoS Negl. Trop. Dis. 6 (2012) e1483. doi:10.1371/journal.pntd.0001483.

[15] S.D. Brugger, C. Baumberger, M. Jost, W. Jenni, U. Brugger, K. Mühlemann, Automated counting of bacterial colony forming units on agar plates, Public Libr. Sci. One. 7 (2012) 1–6. doi:10.1371/journal.pone.0033695.

[16] J. Marotz, C. Lübbert, W. Eisenbeiß, Effective object recognition for automated counting of colonies in Petri dishes (automated colony counting), Comput. Methods Programs Biomed. 66 (2001) 183–198. doi:10.1016/S0169-2607(00)00128-0.

[17] P. Leonard, S. Hearty, J. Brennan, L. Dunne, J. Quinn, T. Chakraborty, R. Kennedy, Advances in Biosensors for Detection of Pathogens in Food and Water, Microb Technol 32 CrossRef CAS. 2003 SRC (2003) 3–13.

[18] D. Rodriguez-Lazaro, Real-time PCR in food science: current technology and applications, Norfolk, UK: Caister Academic Press, 2013.

[19] A. Paton, J. Paton, Detection and Characterization of Shiga Toxigenic Escherichia coli by Using Multiplex Enterohemorrhagic E . coli hlyA , rfb O111 , and Detection and Characterization of Shiga Toxigenic Escherichia coli by Using Multiplex PCR Assays for stx 1 , stx 2 , eae, J. Clin. Microbiol. 36 (1998) 598–602.

[20] O. Faye, O. Faye, D. Diallo, M. Diallo, M. Weidmann, A.A. Sall, Quantitative real-time PCR detection of Zika virus and evaluation with field-caught mosquitoes., Virol. J. 10

(2013) 311. doi:10.1186/1743-422X-10-311.

[21] Sino Biological Inc., What is ELISA? Enzyme-linked immunosorbent assay, (2016). http://www.elisa-antibody.com/ELISA-Introduction (accessed September 30, 2016).

[22] S. Shan, D. Liu, Q. Guo, S. Wu, R. Chen, K. Luo, L. Hu, Y. Xiong, Sensitive detection of Escherichia coli O157 : H7 based on cascade signal amplification in ELISA, 99 (2016) 7025–7032.

[23] M. Cavaiuolo, S. Paramithiotis, E.H. Drosinos, A. Ferrante, Development and optimization of an ELISA based method to detect Listeria monocytogenes and Escherichia coli O157 in fresh vegetables, Anal. Methods. 5 (2013) 4622–4627. doi:10.1039/c3ay40893k.

[24] H. Hamidinejat, M.R. Seifi Abad Shapouri, M.M. Namavari, P. Shayan, M. Kefayat, Development of an indirect ELISA using different fragments of recombinant Ncgra7 for detection of neospora caninum infection in cattle and water buffalo, Iran. J. Parasitol. 10 (2015) 69–77.

[25] The blog of pacific biolabs, The importance of immunigenicity testing in biotherapeutic development, (2016). http://blog.pacificbiolabs.com/pacificbiolabs/2013/5/6/immunogenicity-testing-overview (accessed September 30, 2016).

[26] D.R. Shankaran, K.V. Gobi, N. Miura, Recent advancements in surface plasmon resonance immunosensors for detection of small molecules of biomedical, food and environmental interest, Sensors Actuators, B Chem. 121 (2007) 158–177.

doi:10.1016/j.snb.2006.09.014.

[27] D.L. Enrico, M.G. Manera, G. Montagna, F. Cimaglia, M. Chiesa, P. Poltronieri, A. Santino, R. Rella, SPR based immunosensor for detection of Legionella pneumophila in water samples, Opt. Commun. 294 (2013) 420–426. doi:10.1016/j.optcom.2012.12.064.

[28] B. Drafts, Acoustic wave technology sensors, IEEE Trans. Microw. Theory Tech. 49 (2001) 795–802. doi:10.1109/22.915466.

[29] K.M.M. Kabir, S.J. Ippolito, G.I. Matthews, S.B. Abd Hamid, Y.M. Sabri, S.K. Bhargava, Determining the optimum exposure and recovery periods for efficient operation of a QCM based elemental mercury vapor sensor, J. Sensors. 2015 (2015). doi:10.1155/2015/727432.

[30] Y. Wan, D. Zhang, B. Hou, Determination of sulphate-reducing bacteria based on vancomycin-functionalised magnetic nanoparticles using a modification-free quartz crystal microbalance, Biosens. Bioelectron. 25 (2010) 1847–1850. doi:10.1016/j.bios.2009.12.028.

[31] S. Patel, H. Park, P. Bonato, L. Chan, M. Rodgers, A review of wearable sensors and systems with application in rehabilitation, J. Neuroeng. Rehabil. 9 (2012) 21. doi:10.1186/1743-0003-9-21.

[32] A. Boisen, T. Thundat, Design & fabrication of cantilever array biosensors, Mater. Today. 12 (2009) 32–38. doi:10.1016/S1369-7021(09)70249-4.

[33] D. Grieshaber, R. Mackenzie, J. Vörös, E. Reimhult, Electrochemical Biosensors -Sensor Principles and Architectures, Sensors. 8 (2008) 1400–1458. doi:10.3390/s8031400.

[34] S.H. Lee, H. Kim, H.H. Girault, H.J. Lee, Portable amperometric perchlorate selective sensors with microhole array-water/organic gel interfaces, Bull. Korean Chem. Soc. 34 (2013) 2577–2582. doi:10.5012/bkcs.2013.34.9.2577.

[35] H. Tang, W. Zhang, P. Geng, Q. Wang, L. Jin, Z. Wu, M. Lou, A new amperometric method for rapid detection of Escherichia coli density using a self-assembled monolayer-based bienzyme biosensor, Anal. Chim. Acta. 562 (2006) 190–196. doi:10.1016/j.aca.2006.01.061.

[36] S.-I. Tu, J. Uknalis, P. Irwin, L.S.L. Yu, The use of Light Addressable Potentiometric Sensor (LAPS) to detect magnetically captured Escherichia coli O157:H7 in ground beef, in: Proc. SPIE 4206, Photonic Detect. Interv. Technol. Safe Food, 1, Boston, 2001: pp. R6923-1-R6923-6. doi:10.1117/12.418716.

[37] X. Zong, C. Wu, X. Wu, Y. Lu, P. Wang, A non-labeled DNA biosensor based on light addressable potentiometric sensor modified with TiO2 thin film., J. Zhejiang Univ. Sci. B. 10 (2009) 860–6. doi:10.1631/jzus.B0920090.

[38] H. Yu, H. Cai, W. Zhang, L. Xiao, Q. Liu, P. Wang, A novel design of multifunctional integrated cell-based biosensors for simultaneously detecting cell acidification and extracellular potential., Biosens. Bioelectron. 24 (2009) 1462–8. doi:10.1016/j.bios.2008.08.045.

[39] A. Richter, G. Paschew, S. Klatt, J. Lienig, K.-F. Arndt, H.-J.P. Adler, Review on Hydrogel-based pH Sensors and Microsensors, Sensors. 8 (2008) 561–581. doi:10.3390/s8010561.

[40] X. Jin, Y.-L. Hsieh, pH-responsive swelling behavior of poly(vinyl alcohol)/poly(acrylic acid) bi-component fibrous hydrogel membranes, Polymer (Guildf). 46 (2005) 5149–5160. doi:10.1016/j.polymer.2005.04.066.

[41] J.A. Kaplan, P. Barthélémy, M.W. Grinstaff, Self-assembled nanofiber hydrogels for mechanoresponsive therapeutic anti-TNFα antibody delivery, Chem. Commun. (2016) 1–4. doi:10.1039/C6CC02221A.

[42] S. Hosseinzadeh, S.M. Rezayat, E. Vashegani-Farahani, M. Mahmoudifard, S. Zamanlui, M. Soleimani, Nanofibrous hydrogel with stable electrical conductivity for biological applications, Polym. (United Kingdom). 97 (2016) 205–216. doi:10.1016/j.polymer.2016.05.013.

[43] S.W. Han, W.G. Koh, Hydrogel-Framed Nanofiber Matrix Integrated with a Microfluidic Device for Fluorescence Detection of Matrix Metalloproteinases-9, Anal. Chem. 88 (2016) 6247–6253. doi:10.1021/acs.analchem.5b04867.

[44] P.K. Vemula, J.E. Kohler, A. Blass, M. Williams, C. Xu, L. Chen, S.R. Jadhav, G. John, D.I. Soybel, J.M. Karp, Self-assembled hydrogel fibers for sensing the multi-compartment intracellular milieu, Sci. Rep. 4 (2014) 4466. http://dx.doi.org/10.1038/srep04466.

[45] G.W.C. Kaye, T. Howell, Tables of physical & chemical constants, Natl. Phys. Lab. (2016). http://www.kayelaby.npl.co.uk/ (accessed October 5, 2016).

[46] J.S. Foresi, T.D. Moustakas, Metal contacts to gallium nitride, Appl. Phys. Lett. 62 (1993) 2859–2861. doi:10.1063/1.109207.

[47] W. Kang, M.S. Hybertsen, Quasiparticle and optical properties of rutile and anatase TiO2,

Phys. Rev. B - Condens. Matter Mater. Phys. 82 (2010). doi:10.1103/PhysRevB.82.085203.

[48] Z. Zhang, J.T. Yates, Band Bending in Semiconductor Chemical and Physical Consequences at Surfaces and Interfaces.pdf, Chem. Rev. 112 (2012) 5520–5551. doi:10.1021/cr3000626.

[49] Y. Tsividis, Operation and modeling of the MOS transistor, 2nd ed., McGraw-Hill, New York, 1999.

[50] R.H. Wilson, Electron transfer processes at the semiconductor-electrolyte interface, 1980. doi:10.1080/10408438008243628.

[51] A.J. Bard, L.R. Faulkner, Fundamentals and applications, 2nd ed., Wiley and sons, 2001. doi:10.1038/nprot.2009.120.Multi-stage.

[52] a. J. Nozik, R. Memming, Physical Chemistry of Semiconductor - Liquid Interfaces, J. Phys. Chem. 100 (1996) 13061–13078. doi:10.1021/jp953720e.

[53] K. Rajeshwar, Fundamentals of Semiconductors Electrochemistry and Photoelectrochemistry, Encycl. Electrochem. (2007) 1–51. doi:10.1002/9783527610426.bard060001.

[54] R. Memming, G. Schwandt, Potential and Charge Distribution at Semiconductor???electrolyte Interfaces, Angew. Chemie Int. Ed. English. 6 (1967) 851–861. doi:10.1002/anie.196708511.

[55] J.C. Owicki, L.J. Bousse, D.G. Hafeman, G.L. Kirk, J.D. Olson, H.G. Wada, J.W. Parce, The light-addressable potentiometric sensor: principles and biological applications., Annu.

Rev. Biophys. Biomol. Struct. 23 (1994) 87–113. doi:10.1146/annurev.bb.23.060194.000511.

[56] A.J. Bard, Z. Cynthia, Electroanalytical chemistry: a series of advances, 24th ed., CRC press, 2016. https://books.google.ca/books?id=3GTRBQAAQBAJ&dq=super+nernstian+response+%2B+surface+activity&source=gbs_navlinks_s.

[57] L. Bousse, J.C. Owicki, J. Wallace Parce, Biosensors with microvolume reaction chambers, in: S. Yamauchi (Ed.), Chem. Sens. Technol., 4th ed., Elsevier, Tokyo, 1992.

[58] M. Sartore, M. Adami, C. Nicolini, Computer simulation and optimization of a light addressable potentiometric sensor, Biosens. Bioelectron. 7 (1992) 57–64. doi:10.1016/0956-5663(92)90031-H.

[59] World Business Council for Sustainalbe Development, Water Facts and trends - update, (2009) 1–14. http://www.wbcsd.org/Pages/EDocument/EDocumentDetails.aspx?ID=137.

[60] P.M. Shaibani, K. Jiang, G. Haghighat, M. Hassanpourfard, H. Etayash, S. Naicker, T. Thundat, The detection of Escherichia coli (E. coli) with the pH sensitive hydrogel nanofiber-light addressable potentiometric sensor (NF-LAPS), Sensors Actuators, B Chem. 226 (2016) 176–183. doi:10.1016/j.snb.2015.11.135.

[61] C.F. Werner, C. Krumbe, K. Schumacher, S. Groebel, H. Spelthahn, M. Stellberg, T. Wagner, T. Yoshinobu, T. Selmer, M. Keusgen, M.E.M. Baumann, M.J. Schöning, Determination of the extracellular acidification of Escherichia coli by a light-addressable potentiometric sensor, Phys. Status Solidi Appl. Mater. Sci. 208 (2011) 1340–1344.

doi:10.1002/pssa.201001141.

[62] B. Byrne, E. Stack, N. Gilmartin, R. O'Kennedy, Antibody-Based Sensors: Principles, Problems and Potential for Detection of Pathogens and Associated Toxins, Sensors. 9 (2009) 4407–4445. doi:10.3390/s90604407.

[63] A. Sohrabi, P.M. Shaibani, T. Thundat, The effect of applied electric field on the diameter and size distribution of electrospun Nylon6 nanofibers., Scanning. 35 (2013) 183–8. doi:10.1002/sca.21044.

[64] I. Manavi-Tehrani, M. Rabiee, M. Parviz, M.R. Tahriri, Z. Fahimi, Preparation, Characterization and Controlled Release Investigation of Biocompatible pH-Sensitive PVA/PAA Hydrogels, Macromol. Symp. 296 (2010) 457–465. doi:10.1002/masy.201051062.

[65] X.M. Wang, X.D. Li, G.Q. Zheng, J.M. Jiang, J.Y. Chen, X.D. Zhang, In Situ Synthesis of PVA-PAA-HA Interpenetrating Composite Hydrogel, Key Eng. Mater. 309–311 (2006) 1165–1168. doi:10.4028/www.scientific.net/KEM.309-311.1165.

[66] W. Witoonsaridsilp, O. Paeratakul, B. Panyarachun, N. Sarisuta, Development of Mannosylated Liposomes Using Synthesized N-Octadecyl-d-Mannopyranosylamine to Enhance Gastrointestinal Permeability for Protein Delivery, AAPS PharmSciTech. 13 (2012) 699–706. doi:10.1208/s12249-012-9788-1.

[67] Y.-H. Lin, A. Das, C.-S. Lai, A simple and convenient set-up of light addressable potentiometric sensors (LAPS) for chemical imaging using a commercially available projector as a light source, Int. J. Electrochem. Sci. 8 (2013) 7062–7074.

[68] A.B.M. Ismail, T. Yoshinobu, H. Iwasaki, H. Sugihara, T. Yukimasa, I. Hirata, H. Iwata, Investigation on light-addressable potentiometric sensor as a possible cell-semiconductor hybrid, Biosens. Bioelectron. 18 (2003) 1509–1514. doi:10.1016/s0956-5663(03)00129-5.

[69] P. Waller, Seattle Memo's Mexican Restaurant Link in E. coli Cluster, (2016). http://www.foodpoisonjournal.com/foodborne-illness-outbreaks/seattle-memos-mexican-restaurant-link-in-e-coli-cluster/#.V9rWa7zzd1o (accessed September 15, 2016).

[70] L.A. King, E. Loukiadis, P. Mariani-Kurkdjian, S. Haeghebaert, F.X. Weill, C. Baliere, S. Ganet, M. Gouali, V. Vaillant, N. Pihier, H. Callon, R. Novo, O. Gaillot, D. Thevenot-Sergentet, E. Bingen, P. Chaud, H. de Valk, Foodborne transmission of sorbitol-fermenting Escherichia coli O157:[H7] Via ground beef: An outbreak in northern France, 2011, Clin. Microbiol. Infect. 20 (2014) O1136–O1144. doi:10.1111/1469-0691.12736.

[71] D. Zhao, J.U. Barrientos, Q. Wang, S.M. Markland, J.J. Churey, O.I. Padilla-Zakour, R.W. Worobo, K.E. Kniel, C.I. Moraru, Efficient Reduction of Pathogenic and Spoilage Microorganisms from Apple Cider by Combining Microfiltration with UV Treatment., J. Food Prot. 78 (2015) 716–22. doi:10.4315/0362-028X.JFP-14-452.

[72] A. Singh, S. Poshtiban, S. Evoy, Recent Advances in Bacteriophage Based Biosensors for Food-Borne Pathogen Detection, Sensors. 13 (2013) 1763–1786. doi:10.3390/s130201763.

[73] J.-Y. Lee, S.-S. Kim, D.-H. Kang, Effect of pH for inactivation of Escherichia coli O157:H7, Salmonella Typhimurium and Listeria monocytogenes in orange juice by ohmic heating, LWT - Food Sci. Technol. 62 (2012) 83–88. doi:10.1016/j.lwt.2015.01.020.

[74] S. Yoo, K. Ghafoor, J.U. Kim, S. Kim, B. Jung, D.-U. Lee, J. Park, Inactivation of <I>Escherichia</I> <I>coli</I> O157:H7 on Orange Fruit Surfaces and in Juice Using Photocatalysis and High Hydrostatic Pressure, J. Food Prot. 78 (2015) 1098–1105. doi:10.4315/0362-028X.JFP-14-522.

[75] A. Chen, S. Chatterjee, Nanomaterials based electrochemical sensors for biomedical applications, Chem. Soc. Rev. 42 (2013) 5425–38. doi:10.1039/c3cs35518g.

[76] E. Wong, F. Vaillant-Barka, E. Chaves-Olarte, Synergistic effect of sonication and high osmotic pressure enhances membrane damage and viability loss of Salmonella in orange juice, Food Res. Int. 45 (2012) 1072–1079. doi:10.1016/j.foodres.2010.07.037.

[77] S. Jain, S. a Bidol, J.L. Austin, E. Berl, F. Elson, M. Lemaile-Williams, M. Deasy, M.E. Moll, V. Rea, J.D. Vojdani, P. a Yu, R.M. Hoekstra, C.R. Braden, M.F. Lynch, Multistate outbreak of Salmonella Typhimurium and Saintpaul infections associated with unpasteurized orange juice--United States, 2005., Clin. Infect. Dis. 48 (2009) 1065–1071. doi:10.1086/597397.

[78] A.H.P. Anvarian, M.P. Smith, T.W. Overton, The effects of orange juice clarification on the physiology of Escherichia coli; growth-based and flow cytometric analysis, Int. J. Food Microbiol. Anvarian Int. J. Food Microbiol. 219 (2015) 38–43. doi:10.1016/j.ijfoodmicro.2015.11.016.

[79] N. Firon, I. Ofek, N. Sharon, Carbohydrate-Binding Sites of the Mannose-Specific Fimbrial Lectins of Enterobacteria, Infect. Immun. 43 (1984) 1088–1090.

[80] M. Vander Heiden, L. Cantley, C. Thompson, Understanding the Warburg effect: The

metabolic Requiremetns of cell proliferation, Science. 324 (2009) 1029–1033. doi:10.1126/science.1160809.Understanding.

[81] G. Kroemer, J. Pouyssegur, Tumor Cell Metabolism: Cancer's Achilles' Heel, Cancer Cell. 13 (2008) 472–482. doi:10.1016/j.ccr.2008.05.005.

[82] P.P. Hsu, D.M. Sabatini, Cancer cell metabolism: Warburg and beyond, Cell. 134 (2008) 703–707. doi:10.1016/j.cell.2008.08.021.

[83] P. R. Pandey, W. Liu, F. Xing, K. Fukuda, K. Watabe, Anti-Cancer Drugs Targeting Fatty Acid Synthase (FAS), Recent Pat. Anticancer. Drug Discov. 7 (2012) 185–197. doi:10.2174/157489212799972891.

[84] D.R. Wise, C.B. Thompson, Glutamine addiction: a new therapeutic target in cancer, Trends Biochem. Sci. 35 (2010) 427–433. doi:10.1016/j.tibs.2010.05.003.

[85] K. Birsoy, D.M. Sabatini, R. Possemato, Untuning the tumor metabolic machine: Targeting cancer metabolism: a bedside lesson, Nat. Med. 18 (2012) 1022–1023. doi:10.1038/nm.2870.

[86] Y. Zhao, E.B. Butler, M. Tan, Targeting cellular metabolism to improve cancer therapeutics., Cell Death Dis. 4 (2013) e532. doi:10.1038/cddis.2013.60.

[87] D. a Tennant, R. V Durán, E. Gottlieb, Targeting metabolic transformation for cancer therapy., Nat. Rev. Cancer. 10 (2010) 267–277. doi:10.1038/nrc2817.

[88] M.G. Vander Heiden, Targeting cancer metabolism: a therapeutic window opens., Nat. Rev. Drug Discov. 10 (2011) 671–684. doi:10.1038/nrd3504.

[89] H. Pelicano, D.S. Martin, R.-H. Xu, P. Huang, Glycolysis inhibition for anticancer treatment., Oncogene. 25 (2006) 4633–46. doi:10.1038/sj.onc.1209597.

[90] M. Zhou, Y. Zhao, Y. Ding, H. Liu, Z. Liu, O. Fodstad, A.I. Riker, S. Kamarajugadda, J. Lu, L.B. Owen, S.P. Ledoux, M. Tan, Warburg effect in chemosensitivity: targeting lactate dehydrogenase-A re-sensitizes taxol-resistant cancer cells to taxol., Mol. Cancer. 9 (2010) 33. doi:10.1186/1476-4598-9-33.